FINAL REPORT

Sponsors: Office of Naval Research (ONR)
U.S. Army Research Office (ARO)
Prime Contract No: NOOO14-82-K-0350
MIT Report No: MIT-EL 88-001
Contract Period: 4/1/82-5/31/86
Date: February 1, 1988

SINTERABLE CERAMIC POWDERS FROM LASER-HEATED GASES

Dr. John S. Haggerty
Energy Laboratory &
Materials Processing Center
Massachusetts Institute of Technology
Cambridge, MA 02139
(617) 253-2129

The views and conclusions contained in this document are those of the authors and should not be interpreted as necessarily representing the official policies either expressed or implied of the Office of Naval Research or of the U.S. Government

SECURITY CLASSIFICATION OF THIS PAGE

REPORT DOCUMENTATION PAGE

1a. REPORT SECURITY CLASSIFICATION Unclassified	1b. RESTRICTIVE MARKINGS
2a. SECURITY CLASSIFICATION AUTHORITY ---	3. DISTRIBUTION/AVAILABILITY OF REPORT Unlimited
2b. DECLASSIFICATION/DOWNGRADING SCHEDULE ---	
4. PERFORMING ORGANIZATION REPORT NUMBER(S) MIT-EL 88-001	5. MONITORING ORGANIZATION REPORT NUMBER(S) ---
6a. NAME OF PERFORMING ORGANIZATION Massachusetts Institute of Technology 6b. OFFICE SYMBOL (If applicable)	7a. NAME OF MONITORING ORGANIZATION Department of Navy Office of Naval Research
6c. ADDRESS (City, State, and ZIP Code) Cambridge, MA 02139	7b. ADDRESS (City, State, and ZIP Code) 800 N. Quincy St. Arlington, VA 22217-5000
8a. NAME OF FUNDING/SPONSORING ORGANIZATION ONR jointly with ARO 8b. OFFICE SYMBOL (If applicable)	9. PROCUREMENT INSTRUMENT IDENTIFICATION NUMBER N00014-82-K-0350
8c. ADDRESS (City, State, and ZIP Code) ONR as in No. 7b ARO - Research Triangle Park, NC 27709	10. SOURCE OF FUNDING NUMBERS PROGRAM ELEMENT NO. / PROJECT NO. / TASK NO. / WORK UNIT ACCESSION NO.

11. TITLE (Include Security Classification)

Sinterable Ceramic Powders from Laser Heated Gases

12. PERSONAL AUTHOR(S)

Haggerty, John S.

13a. TYPE OF REPORT	13b. TIME COVERED	14. DATE OF REPORT (Year, Month, Day)	15. PAGE COUNT
Final Report	FROM 4/1/82 TO 5/31/86	1988 February	154

16. SUPPLEMENTARY NOTATION

17. COSATI CODES			18. SUBJECT TERMS (Continue on reverse if necessary and identify by block number)	
FIELD	GROUP	SUB-GROUP	Ceramic processing	Ceramic powder(s)
			Ceramic powder synthesis	Si powder
			Laser induced gas-phase reactions	Si_3N_4 powder

19. ABSTRACT (Continue on reverse if necessary and identify by block number)

Extremely high quality ceramic powders have been synthesized from SiH_4, NH_3 and CH_4 reactant gasses that are heated by absorbing energy emitted from a CO_2 laser. Resulting Si, Si_3N_4 and SiC powders have been characterized in terms of parameters which are important for densification processes. The powders are virtually ideal. The fully dispersible powders have mean diameters ranging from 0.1-0.3 μm with a standard deviation that is typically 25-45%. As-synthesized powders are extremely high purity because the synthesis equipment is hermetic and cold-walled.

The synthesis process has been modeled on a macro scale with respect to heat-transfer, fluid-flow and stability criteria. These results have permitted the process to be scaled safely to production rates up to 8-40 tons/year/nozzle. The particle formation and growth processes have also been analyzed experimentally and analytically in terms of a collision-coalescence model. Application of these models permitted particle sizes to be increased to useful dimensions while retaining complete dispersibility. Compound particles

20. DISTRIBUTION/AVAILABILITY OF ABSTRACT ☒ UNCLASSIFIED/UNLIMITED ☐ SAME AS RPT. ☐ DTIC USERS	21. ABSTRACT SECURITY CLASSIFICATION ---
22a. NAME OF RESPONSIBLE INDIVIDUAL Robert Pohanka	22b. TELEPHONE (Include Area Code) (202) 696-4402 22c. OFFICE SYMBOL 1131

DD FORM 1473, 84 MAR 83 APR edition may be used until exhausted. All other editions are obsolete

SECURITY CLASSIFICATION OF THIS PAGE

☆U.S. Government Printing Office: 1985-507-047

18. Subject terms (continued)

SiC powder
Particle nucleation kinetics
Particle growth kinetics
Nitriding kinetics
SiC sintering kinetics
Particle surface chemistry
Anhydrous dispersants

Ceramic properties
SiC strength, hardness & toughness
RBSN strength, hardness & toughness
RBSN oxidation kinetics

Oxide melt density
Oxide melt surface tension
Pendant-drop analysis

19. Abstract (continued)

form by a 2-step reaction sequence between molten silicon particles and a reactive atmosphere only after the Si particles have grown to desired dimensions. The process is extremely efficient; $\geq$95% of the SiH_4 is reacted in a single pass through the laser beam and approximately 2 kwhr of energy are required per kilo of powder. Manufacturing costs are projected to be $1.50-5.00/kg plus the cost of the reactants.

Resulting powders have been dispersed and shaped into flaw-free, maximum density green parts; colloidal pressing and centrifugal sedimentation techniques have been used successfully. Reaction bonded silicon nitride (RBSN) forms from the Si powders in unusually rapid, low temperature (e.g. 1150°C, 1 hr and 1250°C, 10 min) exposures. The SiC powders sinter to virtually full density in 1 hr at 2050°C.

The properties of both RBSN and sintered SiC (SSC) parts made from the laser-synthesized powders are excellent. RBSN strengths (up to 690 MPa) are 3-5 times values normally observed at the same densities and are in the range normally associated with fully dense alpha-Si_3N_4. The strengths of the SSC parts are also much higher than are normally observed (up to 714 MPa). The oxidation resistance of the RBSN is approximately 10 times better than conventional RBSN and 5-10 times better than commercial hot pressed Si_3N_4 (HPSN) for 1000 and 1400°C air exposures. The superior properties and consolidation kinetics result directly from the high quality of the green parts and the purity levels maintained in the powders through the firing stage.

As a separate topic, the surface tensions and densities of Al_2O_3 melts with MgO, TiO_2 and ZrO_2 additions were measured in air, He and He-H_2 atmospheres using the pendant-drop technique. Melts on the bottom ends of sintered rods were formed by CO_2 laser heating. A curve fitting technique was developed that improved the experimental accuracy of analyzing the short pendant drops that are characteristic of these materials.

TABLE OF CONTENTS

		Page
	DOD form 1473	iii
	Acknowledgements	vi
I.	**Summary**	1
II.	**Overview**	
	1. Laser Synthesized Ceramic Powders: Synthesis, Characteristics, Fabrication, and Part Properties	7
III.	**Powder Synthesis Process**	
	1. Models for Synthesis of Ceramic Powders by Vapor Phase Reactions	15
	2. Powder Temperature, Size, and Number Density in Laser-Driven Reactions	25
	3. Crystal Structure of Silicon Powders Produced from Laser-Heated Silane	37
IV.	**Post Synthesis Processing**	
	1. Wetting and Dispersion of Silicon Powder Without Deflocculants	41
	2. Dispersion of SiC Powders in Non-aqueous Solvents	45
	3. Drying of Silicon Powder Compacts	79
	4. Processing and Properties of Reaction Bonded Silicon Nitride and Sintered Silicon Carbide made from Laser Synthesized Powders	85
V.	**Properties of Reaction Bonded Silicon Nitride and Silicon Carbide made from Laser Synthesized Powders**	
	1. Processing and Properties of Reaction Bonded Silicon Nitride made from Laser Synthesized Silicon Powders	95
	2. High Strength, Oxidation Resistant Reaction-Bonded Silicon Nitride from Laser-Synthesized Silicon Powder	107
	3. High Strength Reaction Bonded Silicon Nitride	115
	4. Properties of Reaction Bonded Silicon Nitride made from High Purity Silicon Powder	127
VI.	**Melt Properties**	
	1. Surface Tensions of Alumina-Containing Liquids	139
VII.	**Appendix**	
	1. Listing of Publications and Theses Resulting from Research Sponsored by this Program	145

ACKNOWLEDGEMENTS

The final accomplishments of research programs sponsored first by DARPA, then by ONR and ARO, are summarized in this report. These series of research programs permitted us to study the basic processing issues needed to define the mechanisms by which high quality non-oxide ceramic powders could be made at commercially interesting rates. Using the powders we produced, very significant property improvements were achieved. The research was exciting and we believe valuable for the ceramics community.

The research programs involved many individuals and were truly interdisciplinary in nature, drawing on backgrounds ranging from surface chemistry to aeronautical engineering. It was only through the integration of these efforts that we were able to accomplish our overall objectives. We have attempted to acknowledge the individual contributions directly through the authorship of the papers that were included in this report and secondarily through the references they cite.

The participants in the research program included undergraduates, graduate students, post-doctoral research associates, research staff and faculty. The educational experiences provided by this research are only partially shown by the included list of theses; the interactions encouraged by the complex nature of the program as a whole provided an experience that is rare in university research.

We gratefully acknowledge all contributions to this research program. In particular, we are grateful for the educational opportunities provided to MIT by this sponsorship.

SUMMARY

SINTERABLE CERAMIC POWDERS FROM LASER HEATED GASES

by

Dr. John S. Haggerty
Energy Laboratory
Materials Processing Center
Massachusetts Institute of Technology
Cambridge, Massachusetts 02139

The focus of this research program changed continuously as our understandings permitted us to transition from simply demonstrating the feasibility of the laser-heated, powder-synthesis process to the evaluation of properties of parts made from powders synthesized under optimized, high mass flow rate conditions. The program's scope included powder synthesis, post-synthesis processing and property measurement tasks for Si, Si_3N_4 and SiC powders made from laser heated gas-phase reactants; Si powders were used for making reaction bonded silicon nitride (RBSN). More broadly, this research program sought to demonstrate the validity of the processing-microstructure-property paradigm first proposed by MIT; we believed it would only be through the use of highly perfect powders and careful post-synthesis processing steps that it would be possible to achieve the uniform, defect-free microstructures and the resulting property improvements needed for many demanding applications. The powder characteristics that were sought were small, uniform diameters, spherical shapes, high purity and, most importantly, an absence of agglomerates.

In the laser-heated powder synthesis process, reactant gassed are heated to reaction temperatures by absorbing IR photons emitted from a CO_2 laser. The absorbed energy is thermalized rapidly through intermolecular collisions. This heating technique permits both the achievement of process conditions needed to produce the desired powder characteristics and excellent access for process diagnostics. In this process, heating rates are rapid and uniform (10^5-10^8 °C/s), the maximum temperature is precisely controllable, and cooling rates are rapid (10^5 °C/s). Design features for a hermetic, cold-wall reaction cell are straightforward. Manufacturing cost analyses shows that Si,

Si_3N_4 and SiC powders can be made by the laser-heated synthesis process from exothermic reactions for $1.50-5.00/kg plus the cost of the reactants; the process has commercial viability.

The powder synthesis process was modeled extensively on both the macro- and micro-scales. Critical for these analyses was the novel experimental apparatus we developed which permitted the particles' size, number density and emissivity of the particulate plume in the reaction zone to be measured with nominally 10^{-5} second temporal and $<10^{-1}$mm spatial resolutions. These results provided direct measurements of particle formation and growth rates as a function of time, temperature and composition; they also defined the precise locations where phase transformation or compound formation reactions occurred.

Heat transfer and fluid flow analyses showed that while the process appeared stable and uniform, there were several phenomena that could preclude the achievement of uniform time-temperature-composition histories needed to produce uniform powders. Most of these adverse effects became accentuated as the process was increased in scale. Radial mixing of the reactant and annular gas streams can dilute and cool the outer region of the reaction zones and locally produce smaller than average diameter particles. The turbidity of large diameter, high number density particle plumes can prevent needed rapid cooling rates of interior particles by precluding direct radiation to cold surfaces. Cyclic instabilities can result from unusual flash-back dynamics with IR absorbing gases that react exothermically to produce particulate products which absorb varying levels of the IR laser energy. These issues were examined analytically and experimentally. In each case, means were found to operate the synthesis process safely without adversely affecting the powder quality with the high particle number densities and gas velocities needed for low cost production.

Silicon, SiC and Si_3N_4 powder formation and growth mechanisms under high mass flow rate conditions needed for commercial production were successfully modeled experimentally and analytically. Early in this program, we attempted to describe the process by classical nucleation and growth models. While the results agreed reasonably well with theory for small particle diameters (<50nm) produced in dilute, low pressure conditions, we were unable to achieve needed particle diameters (>100nm) with predicted reaction-cell conditions. The newly developed models predict average size, size distribution and morphologies for varied process conditions. Important variables include the

choice of reactants, temperature distribution, gas velocity distribution and mixing. Good Si powders are formed by collisions and coalescence of molten particles rather than nucleation and growth. Growth continues until freezing or the start of carburization or nitridation reactions. Quenching the Si particles prevents agglomeration after growth terminates. Suitable diameter, dispersible Si_3N_4 and SiC particles form by a 2-step mechanism involving reactions of the Si particles only after they have grown to desired, final dimensions. Because it is essential that the reaction steps be spatially separated, premixed reactants are subject to many constraints. Good SiC powders were made with premixed SiH_4/CH_4 and $SiCl_2H_2/C_2H_4$ streams; good Si_3N_4 were made only by injecting NH_3 into a stream of molten Si particles because we did not find a suitable N_2 source to separate the reaction steps with premixed reactant streams. Beyond the synthesis research tasks, the program concentrated on Si and SiC as the lead materials.

Pure anhydrous solvent and solvent-dispersant systems were identified that could be used to fully disperse Si and SiC powders. Stabilization resulted from both coulombic and steric mechanisms. While stable at low volume concentrations of solids, few provided adequate stability at high particle concentrations. Stability was found to be highly sensitive to contamination of the liquids by water and to exposures of the particles to air. Pure, laser-synthesized SiC powder was shown to have a basic surface and was stabilized by acidic solvents while either commercial or laser-synthesized SiC powder that had been exposed to air had acidic surfaces and were dispersed by basic solvents. Optimum systems will probably be based on block-copolymer dispersants matched to the high-purity powder surfaces and compatible with drying requirements. Initial results with these types of polymer dispersants provided stability up to 47 volume percent solids.

Crack-free, dried green bodies having packing densities at least equalling that of a random close packed structure (63%) were made with unclassified Si and SiC powders by colloidal pressing; slightly lower density levels were achieved by centrifugal sedimentation. Early, small diameter powders of all three materials could not be packed to densities greater than approximately 45% unless agglomerates were removed by centrifugal classification. This pretreatment usually raised green densities to the 50-60% range but the yield of good powder was unacceptably low. Density levels in green parts generally increased with improved dispersion stability; however, the

density level and uniformity were most strongly affected by the degree of agglomeration in the powders.

Cracks were frequently observed in colloidally pressed parts unless they were subjected to a CIP'ing step. The crack frequency in the parts was reduced by improved die geometry and technique; the residual number appeared attributable to the highly compliant stainless steel sponges used to apply the load to the samples via the ported pistons. CIP'ing to 275 MPa eliminated virtually all of the cracks; however, RBSN strengths revealed an optimum in terms of the fraction of the solvent (25-35% of the total solvent) removed from the as-pressed parts.

With good heat transfer to the sample, drying kinetics were rate controlled either by the boundary-layer or pore-diffusion mass transport processes depending on external gas velocity and sample dimensions. Without heat-sinking to a thermal mass, heat transfer through the boundary layer generally will be rate controlling for the liquid removal phase of the drying processes. Adsorbed residuals were not removed until samples were exposed to temperatures substantially in excess of the solvents' boiling points for prolonged periods. It is absolutely essential that all volatile residuals be removed from these samples before they are subjected to firing temperatures because the unusually small channel diameters can cause explosive pressure levels to develop.

Nitriding and densification kinetics proceeded rapidly at low temperatures because of the achieved combination of small particle size, high purity and good packing. These results were most dramatic with RBSN. Normal nitriding schedules involve times up to a few hundred hours at temperatures in excess of the Si melting point (1410°C). With normal handling, the laser synthesized Si nitrided to completion in 1 hour at 1400°C; with exceptionally clean handling, it nitrides even faster, e.g. 1 hour at 1150°C or <10 minutes at 1250°C. The rate controlling nitriding mechanisms that are responsible for the unusual reverse reaction gradients (higher extent of reaction in interior regions) in these samples makes fabrication of large parts feasible. SiC also sintered to essentially full density at relatively low temperatures and short times (1 hour at 2050°C) but the kinetics have not been studied as extensively as for RBSN.

Properties of the parts made from the laser-synthesized Si and SiC powders were unusually good. RBSN samples exhibited average strengths that were 3-5 times higher than strengths previously observed by others at both

density levels (63 and 75%) that were studied; these strengths are well into the range normally associated with fully dense alpha Si_3N_4. The maximum strength observed for RBSN was 690 MPa. The oxidation resistance of the RBSN samples in air at 1000 and 1400°C was 10 times better than is typical of RBSN and 5-10 better than hot pressed Si_3N_4 (HPSN). Strengths of the RBSN did not decrease after these oxidizing exposures. Hardness and fracture toughness values were somewhat above average for RBSN. Sintered SiC (SSC) samples exhibited an average strength of 690 MPa, a value that is 2 times normally observed values for this material. The maximum strength level observed for SSC was 714 MPa. Hardness values observed for these samples were normal. The unusually good property levels observed for the samples made from the laser-synthesized powders result directly from the microstructural quality made possible only with defect free powders. Though exceptional, the strengths in these samples were controlled by defects that were much larger than constituent powders (typically 10-15 μm), so further improvements are possible.

This research program accomplished its important objectives. Broadly, the overall goal was to demonstrate that superior microstructures and properties could be achieved by using both powders having ideal characteristics and very specific post-synthesis processing procedures. This was accomplished. In achieving this objective, several narrower technical issues were resolved. These included finding means to make the powders, disperse the powders, shape the powders into high-density flaw-free parts, dry the parts and densify the parts. While superior properties and both reduced densification times and temperatures were demonstrated, these results do not represent fully optimized process conditions or maximum property values. Further improvements can be anticipated and much remains to be done to make these results feasible in commercial scale processes.

Separate from the main thrust of this research program, we also used the unique features of laser heating to characterize the surface tensions and densities of molten alumina containing melts. Surface tension to density ratios were measured for Al_2O_3 plus Cr_2O_3, MgO, TiO_2 and ZrO_2 in air, He and H_2 + He atmospheres with laser melted pendant-drops. Viscosity measurements from vibrating drops were inconclusive because of problems associated with exciting a single mode of vibration. Densities of the melts were calculated.

This report is made up of a series of technical publications selected to summarize the program's principal results with a minimum of duplication. Two

publications on properties of RBSN that were completed after this program's termination have been included to illustrate the impact research initiated in this program had on continued work. The report also lists the citations for 9 theses and 29 technical publications that resulted in whole or in part from this research program.

To be published in the Proceedings of the
172nd Meeting of the Electrochemical Society,
Session IV, High Temperature Materials
Synthesis, Honolulu, Hawaii, Oct. 18-23, 1987
P87-05

LASER SYNTHESIZED CERAMIC POWDERS: SYNTHESIS, CHARACTERISTICS, FABRICATION, AND PART PROPERTIES

John H. Flint and John S. Haggerty

Massachusetts Institute of Technology
77 Massachusetts Avenue
Cambridge, Massachusetts 02139

ABSTRACT

Si, Si_3N_4, SiC, TiB_2, TiO_2 and B powders have been made from laser heated gaseous reactants. The unusual and precisely controllable reaction conditions made possible with this heating technique permit uniform, small, high-purity, non-agglomerated powders to be made at high rates. The synthesis process has been modeled empirically and analytically to give direct measures of particle diameters, number densities and temperatures as well as velocities, mixing and stability limits. With careful post-synthesis processing, these powders can be made into defect-free parts with rapid, low-temperature consolidation schedules. Resulting reaction bonded silicon nitride (RBSN) and sintered silicon carbide (SSC) parts exhibit much improved properties.

INTRODUCTION

The properties of structural ceramics approach their theoretical values only if pressure and/or sintering aids are employed during consolidation. This results in increased cost, restricted maximum size and complexity of finished parts, and degraded high-temperature mechanical properties. This research program addressed these issues based on a strategy of producing flaw-free green parts made directly from high-purity, small diameter powders.

POWDER SYNTHESIS

The laser synthesis process was developed (1,2) to produce small, high purity, non-agglomerated ceramic powders. The powders are synthesized by rapidly heating a reactant gas stream with a CW CO_2 laser (Figure 1). The reactant gas flows into the laser beam where it is heated until the gas reacts and the particles nucleate and grow. A concentric flow of argon injected around the reactant stream improves the reaction zone stability and carries the powder through the chimney to a filter where the particles are trapped.

Silane (SiH_4) is used to make Si powders (1), SiH_4 mixed with methane (CH_4) or ethylene (C_2H_4) is used to make SiC (3), and SiH_4 mixed with ammonia is used to make Si_3N_4 (1,4). Under most operating

conditions, all of the SiH_4 is converted to powder. TiB_2 is made from mixtures of $TiCl_4$ with B_2H_6, and boron powder is made from B_2H_6 or $BCl_3 + H_2$ (5). TiO_2 is made from titanium alkoxides (6).

The powder characteristics are controlled by the chemical-reaction, particle-formation and particle-growth rates. The cell pressure, the choice of reactants, their flow rates, the laser power and intensity, and cell geometry determine the rates primarily through their influence on the temperature distribution within the reaction zone. These interactions have been investigated experimentally using a light scattering technique (7), and by correlating synthesis conditions with powder properties. Heating rates, velocities, mixing, reaction zone instabilities and resulting particle size distributions have also been modeled mathematically (8,9).

The resulting powders are small (< 500 nm), are equiaxed, have very high purity (< 200 ppm oxygen), and for the compounds have controlled compositions. Powders with few agglomerates are produced under proper conditions. The combination of small size and freedom from agglomeration allows the powders to be formed into dense, virtually flaw-free green bodies with extremely small pores. Table 1 summarizes the characteristics of typical powders.

Table 1. Summary of Powder Characteristics

Powder Characteristic	Si	Si_3N_4	SiC	TiB_2	B	TiO_2
Mean Diameters (nm)	19-305	7.5-170	20-200	30-50	30-40	12-35
Standard Deviation of Diameters (% of mean)	~50	~25	~25	~50	~25	~75
Impurities O_2 (wt.%)	0.02-0.7	~ 0.3	0.3-1.3			
Total Others (ppm)	≤200	≤100	≤100	NA	NA	NA
Major Elements	Ca, Cu, Fe	Al, Ca	Al, Cu			
Composition	—	0-60% excess Si	0-10% excess Si or C	0-60% excess B	—	NA
Crystallinity	crystalline-amorphous	amorphous-crystalline	crystalline-(Si and SiC) amorphous	crystalline	crystalline-amorphous	crystalline
Grain Size:Mean Diameter	1:5-1:3	~1:2	1:2-1:1	~1:3	~1:1	1:3-1:1

A fluid flow and heat transfer model (8) has provided many insights into the laser synthesis process. Figure 2 shows that as the reactant gases flow into the laser beam their velocity profile becomes nearly uniform, and that pronounced temperature gradients can be present. Radiation from the hot particles is the dominant cooling mechanism at temperatures above 1200°C.

High quality Si powders are formed by the collision and coalescence of liquid Si droplets (9). The process begins when SiH_4 gas heated by the laser decomposes into Si dimers and trimers (10). The number density of particles decreases rapidly as collisions result in particle growth by coalescence. Once the particles solidify growth stops. A variation in exposure times to T >1410°C produces a distribution of particle sizes. Flow streams that are never heated to 1410°C produce agglomerates of small particles. If the cooling rate from 1410°C is slow, aggregates of large particles can be produced. Therefore, the particle size and morphology distributions are directly attributable to the temperature and velocity distributions in the reaction zone (11). Uniform powder is produced only when all flow streams experience similar time-temperature-concentration histories. Figure 3 compares the measured mass distribution of Si powder F28S to distributions calculated from collision/coalescence theory (12). The excellent agreement confirms the accuracy of this model (9).

High quality SiC is formed from premixed streams of SiH_4 and CH_4 via a two step reaction mechanism (3). Two distinct bands appear in the reaction zone. Si particles form and grow in the lower band and carburization occurs in the upper band. The onset of the carburization reaction terminates the particle growth process.

Only very small agglomerated particles are produced (~40 nm) when premixed streams of SiH_4 and C_2H_4 are used (1-3). This results because C_2H_4 starts to carburize the Si particles at temperatures below the melting point of Si, preventing their coalescence and growth into larger spherical particles.

The detailed particle formation and growth mechanisms for TiO_2, TiB_2 and B powders have not been modeled in the same detail as the Si containing powders since this research focused on initiating endothermic reactions with condensed phase reactants. It is probable that melting did not occur for the employed synthesis conditions.

POWDER PROCESSING

Test parts (13-15) were made to determine whether using laser synthesized powders resulted in superior consolidation kinetics and properties. Our objective was to form high purity, defect-free unfired bodies having constituent particles arranged with random close packed rather than ordered structures. Parts were made from dispersions by colloidal (filter) pressing. Dispersing media were selected based on maximizing dispersion stability and drying kinetics while minimizing contaminating residuals and destructive effluents.

RBSN samples used for mechanical testing were made (13-15) from dried Si pellets nitrided without exposure to air in a top loading, cold-wall, tungsten furnace installed inside an Ar atmosphere glove box. Complete nitridation was achieved by heating at 1°C/min up to

1420°C, followed by a 1 hour hold. Studies of the nitriding kinetics and rate controlling mechanisms show (16) that laser synthesized Si parts can be completely nitrided at lower temperatures in shorter times (1150°C, 1h; 1250°C, 10 minutes).

SiC pellets (15) were made from a L30SC type powder to which approximately 0.5% by weight B was introduced during synthesis using B_2H_6. Dried samples were fired at temperatures ranging from 1800°C to 2100°C in a graphite tube furnace in an Ar atmosphere. The heating cycle consisted of a 50°C/h ramp to the firing temperature, a 1 h soak and a furnace quench (50-100°C/h).

PROPERTY MEASUREMENTS

A ball-on-ring biaxial strength test (17,18) was used to determine the room temperature strengths of the nitrided and sintered samples. Hardness and fracture toughness were measured using a Vickers indenter. Oxidation resistance of the RBSN was measured with elevated temperature air exposures.

Figure 4 summarizes the results of strength measurements with two types of RBSN samples (15). An average of 544 ± 80 MPa (Max = 676 MPa) was observed for a group of 75% dense RBSN samples made from powder F55S and an average of 250 MPa (Max = 460 MPa) for 65% dense samples made from an earlier powder (13). Figure 4 also includes three different lines representing least-square fits of exponential functions to RBSN, SSN and HPSN strength data reported in the literature (13,19,20) for laboratory and commercial samples with various surface finishes.

Laser-originating RBSN specimens exhibit average strengths that are 2.5 to 5.0 times the average reported values at both corresponding density levels. Both groups of RBSN samples exhibited strengths normally associated with sintered or hot pressed α-Si_3N_4. Fracture sources were usually either 5-15 μm diameter voids or preexisting lenticular cracks less than 50 μm deep perpendicular to the stress axis. Application of the Griffith equation (21) to the observed strengths yields flaw sizes of 4 to 16 μm.

The results of the strength measurements with the 2050°C SiC samples are also unusual. Although the samples are far from optimal, the observed average strength, 645 ± 60 MPa, (Max = 761 MPa) is approximately twice the strength levels normally observed for sintered SiC (22) and is more typical of hot pressed or HIPed SiC. The only other group that has reported SSC strength levels in this range (23) also employed SiH_4 based synthesis chemistries and similar anhydrous, anaerobic post-synthesis handling procedures.

Vickers hardness values were determined on polished surfaces using 300 and 500 gram loads. Observed values for RBSN ranged from 3.5 to 11.0 GPa. The hardness of 77% dense RBSN (~10 GPa) is higher than

that of 85% dense, highly optimized commercial RBSN (~8.3 GPa) (19). Using the indentation technique (24), our dense specimens exhibited an average K_{IC} value of 2.8 MPa $m^{1/2}$. These are higher than is characteristic of the optimized commercial RBSN (~2.0 MPa $m^{1/2}$) (19) and approach those of sintered α-Si_3N_4. We are continuing to investigate the factors that are responsible for these superior hardness and K_{IC} values.

For SiC, the observed hardness values of 23.8 GPa are also more typical of hot pressed than sintered SiC. The hardness and strength values are presumably coupled. Fracture toughness values could not be measured on the SiC using the indentation technique because stable cracks did not form.

The oxidation resistance of laser-originating RBSN at 1250°C in flowing air is strongly dependent on the porosity level and pore size. As predicted by Thümmler's (25) results at the same temperature, low density specimens undergo significant internal oxidation before saturation is attained. For densities >85% and Hg porosimetry pore radii < 60 nm, Thümmler showed that internal oxidation would be reduced to less than 1% due to pore closure by the oxide product. For laser-originating RBSN (13-15), the extent of oxidation at 1250°C in air was less than 1% for specimens having densities as low as 74%. This superior performance at lower densities very likely results from our samples having smaller pore diameters and more uniform microstructures.

CONCLUSIONS

This research program achieved its principal technical objective; superior consolidation kinetics and properties can result if powders having very specific characteristics are employed in combination with careful post-synthesis handling procedures. Powders must be small, equiaxed, uniform in size, pure and free of agglomerates. Of these criteria, freedom from agglomerates is the most important because agglomerates lower the achievable green density to unacceptably low levels and introduce large, localized defects.

Even without many iterations of the processing variable-microstructure-property approach used in this research, we have achieved property levels that were considered unreachable with RBSN and unusual with sintered SiC. These improvements resulted directly from our ability to make parts in which residual porosity was distributed uniformly in minimum size pores and without large, multiparticle diameter defects.

ACKNOWLEDGMENTS

Numerous staff and students have contributed to this work. Hopefully, all are properly referenced. This research was principally sponsored by DOD (DARPA, ONR, and ARO) and an industrial

consortium including Aisin Seiki Co., Alcoa, NGK Spark Plug Co., Nippon Steel, Sumimoto Electric Industries, Ltd., The Japan Steel Works, Ltd., and Toa Nenryo Kogyo K.K.. Specific topics were supported by DOE, NASA-Lewis and The 3M Corporation. All contributions are gratefully acknowledged.

REFERENCES

1. Cannon, W. R., Danforth, S. C., Flint, J. H., Haggerty, J. S., Marra, R. A., "Sinterable Ceramic Powders from Laser Driven Reactions, Part I; Process Description and Modeling," J. Am. Ceram. Soc., 65 [7], 324-30 (1982).
2. Cannon, W. R., Danforth, S. C., Haggerty, J. S., Marra, R.A., "Sinterable Ceramic Powders from Laser Driven Reactions, Part II; Powder Characteristics and Process Variables," J. Am. Ceram. Soc., 65 [7], 330-5 (1982).
3. Sawano, K., Haggerty, J. S. and Bowen, H. K., "Formation of SiC Powder from Laser Heated Vapor Phase Reactions," Yogyo-Kyokai-Shi (J. of Ceram. Soc. Japan), 95 [1], 64-9 (1987).
4. Aoki, M., Flint, J. H. and Haggerty, J. S., "Laser Synthesis of Silicon Nitride Powders for Ceramic Processing," to be published in Proceedings of the First International Conference on Ceramic Powder Processing Science, Orlando FL, Nov. 1987.
5. Casey, J. D., and Haggerty, J. S., "Laser-Induced Vapor-Phase Syntheses of Boron and Titanium Diboride Powders," Journal of Materials Science, 22, 737-744 (1986).
6. Casey, J. D., and Haggerty, J. S., "Laser-Induced Vapor-Phase Synthesis of Titanium Dioxide Powder," accepted for publication in Journal of Materials Science.
7. Flint, J. H., Marra, R. A. and Haggerty, J. S., "Powder Temperature, Size, and Number Density in Laser Driven Reactions," Aerosol Sci. and Tech., 5, 249-261 (1986).
8. Akmandor, I. S., "Theoretical and Computational Models of Reacting Silane Gas Flows: Laser Driven Pyrolysis of Subsonic and Supersonic Jets," Ph.D. Thesis, MIT, 1985.
9. Flint, J. H. and Haggerty, J.S., "A Model for the Growth of Silicon Particles from Laser-Heated Gases," submitted to Aerosol Science and Technology.
10. Coltrin, M. E., Kee, R. J. and Miller, J. A., "A Mathematical Model of the Coupled Fluid Mechanics and Chemical Kinetics in a Chemical Vapor Deposition Reactor," J. El. Chem. Soc., 131, 425-434 (1984).
11. Ulrich, G. D. and Subramanian, N. S., "Particle Growth in Flames, III. Coalescence as a Rate-Controlling Process," Combustion Sciences and Technology, 17, 210-26 (1977).
12. Lee, K. W., Chen, H. and Gieseke, J. A., "Log-Normally Preserving Size Distribution for Brownian Coagultion in the Free-Molecule Regime," Aerosol Sci. and Tech., 3, 53-62 (1984).
13. Haggerty, J. S., Garvey, G., Lihrmann, J-M, and Ritter, J. E.,

"Processing and Properties of Reaction Bonded Silicon Nitride made from Laser Synthesized Silicon Powders," Defect Properties and Processing of High-Technology Nonmetallic Materials, Materials Research Society Symposia Proceedings, Vol. 60, Pittsburgh, PA, 1986, pp. 51-62.

14. Haggerty, J. S., Flint, J. H., Garvey, G., Lihrmann, J-M. and Ritter, J. E., "High Strength, Oxidation Resistant Reaction Bonded Silicon Nitride from Laser-Synthesized Silicon Powder," Proceedings 2nd International Symposium Ceramic Materials and Components for Engines, Lübeck-Travenmünde Federal Republic of Germany, April 1986.
15. Haggerty, J.S., Flint, J.H., Aoki, M., Garvey, G. J., Okuyama, M., Ritter, J. E., and Sheldon, B.W, "Processing and Properties of Reaction Bonded Silicon Nitride and Sintered Silicon Carbide Made from Laser Synthesized Powders," submitted to The American Ceramic Society.
16. Sheldon, B.W. and Haggerty, J.S., "The Nitridation of High Purity, Laser-Synthesized Silicon Powder to Form Reaction Bonded Silicon Nitride", to be published in the Proceedings of the 12th Annual Conference on Composites and Advanced Ceramics, Cocoa Beach, FL, 1988.
17. Wachtman Jr., J. B., Capps, W. and Mandel, J., "Biaxial Flexure Tests of Ceramic Substrates," J. of Mat. 7[2], 188 (1972).
18. Shelty, D. K., Rosenfield, A. R., McGuire, P., Bansal, G. K. and Duckworth, W. H., "Biaxial Flexure Tests for Ceramics," Am. Ceram. Soc. Bull., 59[12], 1193 (1980).
19. Danforth, S. C. and Haggerty, J. S., "Mechanical Properties of Sintered and Nitrided Laser Synthesized Silicon Powder," J. Am. Ceram. Soc., 66 [4], 273-5 (1983).
20. Rice, R. W., "Comment on 'Additional observations on the strength / nitrided density relationship for a reaction sintered silicon nitride,'" J. Mat. Sci., 12[7], L627 (1977).
21. Smith, F. W., Emergy, A. F. and Kobayashi, A. S., "Stress Intensity Factors for Penny-Shaped Cracks Part II: Semi-Infinite Solid," J. Appl. Mech., 34, Series E, 953-959 (1976).
22. Dudda, S., "Densification and Properties of α-Silicon Carbide," J. Am. Ceram. Soc., 68, C-269 (1985).
23. Saiki, G. and Kondo, J., "Synthesis and Sintering of B-Doped SiC Powders by Plasma Arc Method", Paper 16-BP-86 presented at the Annual Meeting of the American Ceramic Society, March 1986.
24. Anstis, G. R., Chantikui, P., Lawn, B. R. and Marshall, D. B., "A Critical Evaluation of Indentation Techniques for Measuring Fracture Toughness: I, Direct Crack Measurements," J. Am. Ceram. Soc., 64[9], 533 (1981).
25. Porz, F. and Thümmler, F., "Oxidation Mechanism of Porous Silicon Nitride," J. Mat. Sci., 19, 1203-95 (1984).

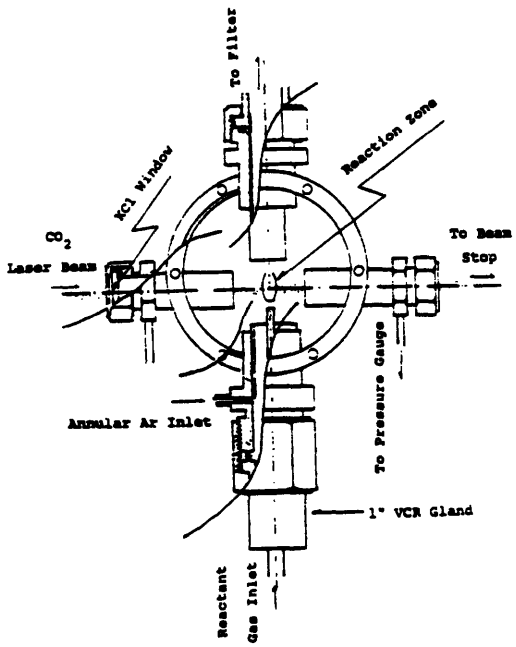

Figure 1. Schematic of CO_2 laser reactor.

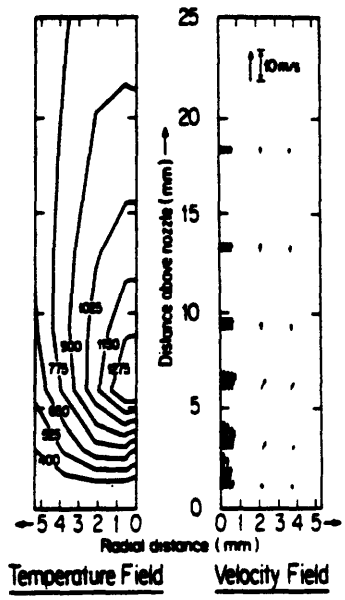

Figure 2. Calculated temperature and flow distributions for laser heated silane reaction zone.

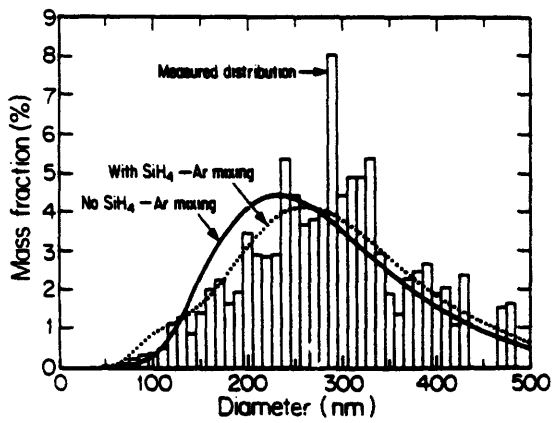

Figure 3. Histogram of mass distribution of silicon powder F28S, compared to calculated distributions (solid curve, no mixing assumed; dashed curve, some mixing with annular argon)

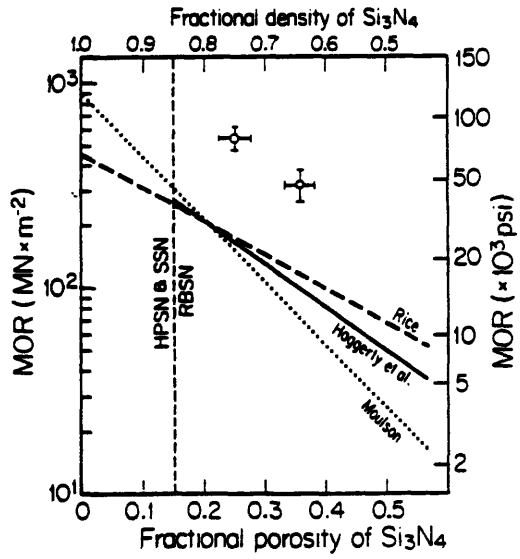

Figure 4. Strength of silicon nitride versus porosity. The strengths of two sets of laser synthesized RBSN are compared to three data surveys.

To be published in the Proceedings of the First International Conference on Ceramic Powder Processing Science, Orlando, Florida, November 1-4, 1987, to be published by the American Ceramic Society P87-08

MODELS FOR SYNTHESIS OF CERAMIC POWDERS BY VAPOR PHASE REACTIONS

John H. Flint and John S. Haggerty
Massachusetts Institute of Technology
Cambridge, MA

INTRODUCTION

Significant improvements in the quality of laser synthesized Si, SiC, and Si_3N_4 powders have been realized based on developed process models that relate particle formation and growth mechanisms to properties. These models are able to accurately predict the particle size, size distribution, and morphology of laser synthesized powders for a variety of process conditions. They also explain many of the features noticed during the development of the laser synthesis process.

LASER HEATED SYNTHESIS REACTIONS

The ceramic powders are synthesized by rapidly heating a reactant gas stream with a CW CO_2 laser beam[1-3] in a cold wall reactor shown schematically in Figure 1. The reactant gas flows from the nozzle into the laser beam, where it is heated at $\approx 10^6$ K/second until the gas reacts and the particles form and grow. A concentric flow of argon injected around the reactant stream stabilizes the reaction zone and helps the powder flow smoothly through the chimney into a filter where the particles are trapped. Because of rapid heating, there is little mixing between the reactant gas and the argon so the reactant concentration is uniform throughout most of the reaction zone.

Silane (SiH_4) is used to make Si powders and SiH_4 mixed with methane (CH_4) or ethylene (C_2H_4) is used to make SiC. Ammonia (NH_3) mixed with SiH_4 is used to make Si_3N_4.

The synthesis process variables that control the powder characteristics are the reaction cell pressure, the choice of reactants, their flow rates and flow ratios, the laser power and intensity, and the nozzle and chimney locations.[1,2] These variables determine the chemical-reaction, particle-formation, and particle-growth rates primarily through their influence on the temperature distribution within the reaction zone. The effects these variables have on the particle formation, growth and chemical composition have been investigated experimentally using the light scattering-transmission technique,[4] and by correlating synthesis conditions with powder properties. The heating rates, velocities, mixing, reaction zone instabilities and resulting particle size distributions have also been modeled mathematically.[5,6]

Table 1 summarizes the physical characteristics and green packing densities of the Si and SiC powders used to make the superior reaction bonded silicon nitride (RBSN) and sintered silicon carbide (SSC).

Table 1. Powder Properties

Powder Designation	F28S	F45S/F55S	L6SC	L30SC-B	N31SN
Material	Si	Si	SiC	B-doped SiC	Si_3N_4
Max Temp. (°C)	1455	1605	1830	1920	1600
Pressure (atm)	1.3	1.3/1.6	1.3	2.0	1.3
D (mass), nm	262	305	90	95	142
σ_g (number)	2.6	1.8	1.7	1.7	2.2
σ_g (mass)	1.5	1.5	1.4	1.4	1.8
Packing Density (%)	59	63	63	63	52

The mean size (D) and size distributions (σ_g) were determined from TEM photomicrographs like Figures 2, 3 and 4. Geometric standard deviations (σ_g) were calculated because the particle size distributions are asymmetric (almost log-normal). A common feature of laser synthesized powders is that the mass distributions are narrower than the number distributions (σ_g (mass) < σ_g (number)).

SILICON POWDER FORMATION MODEL

Figure 2 is a TEM photomicrograph of silicon powder F45S. Virtually all (96% by mass) of the particles are isolated spheres, ranging from 100 to 500 nm in diameter.

High quality silicon powders are formed by the collision and coalescence of liquid silicon droplets. A detailed description of this model is presented elsewhere.[6] The process begins when silane gas heated by the laser decomposes

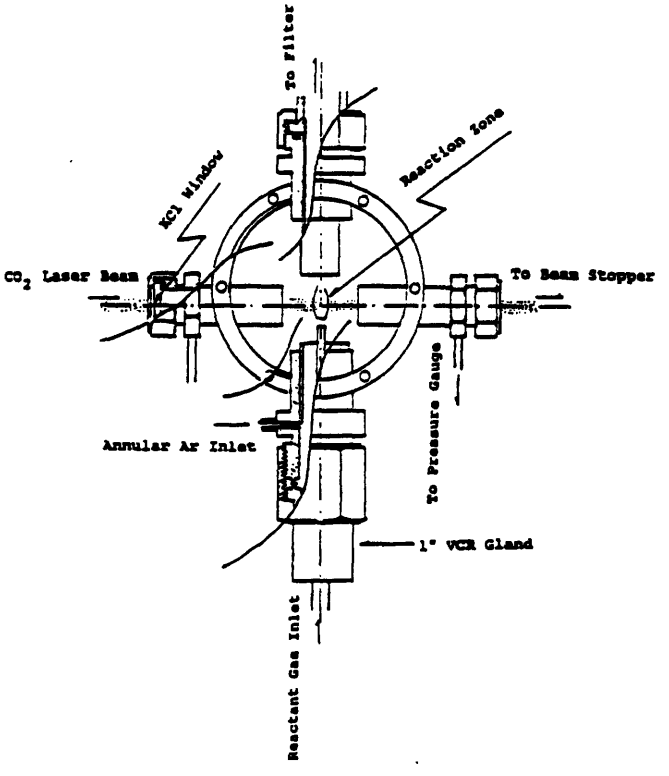

Figure 1. Schematic of CO_2 laser reactor.

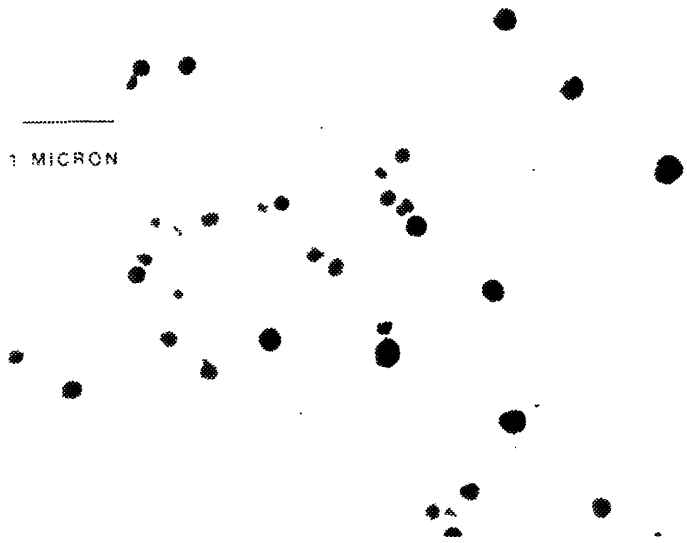

Figure 2. TEM photomicrograph of silicon powder F45S.

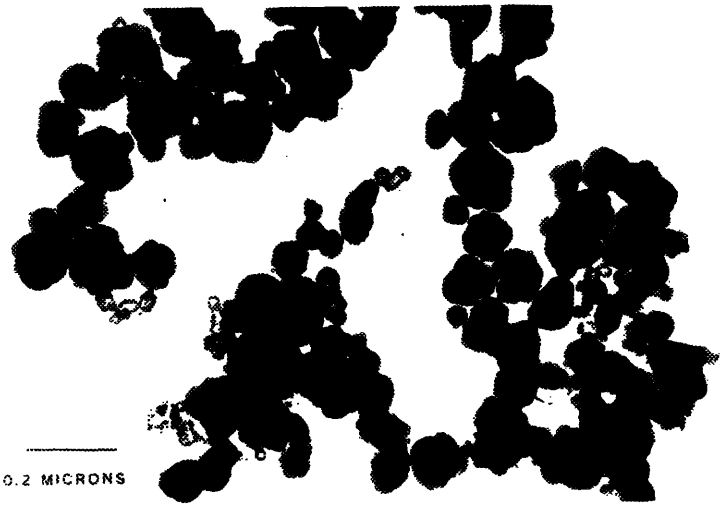

Figure 3. TEM photomicrograph of silicon carbide powder L06SC.

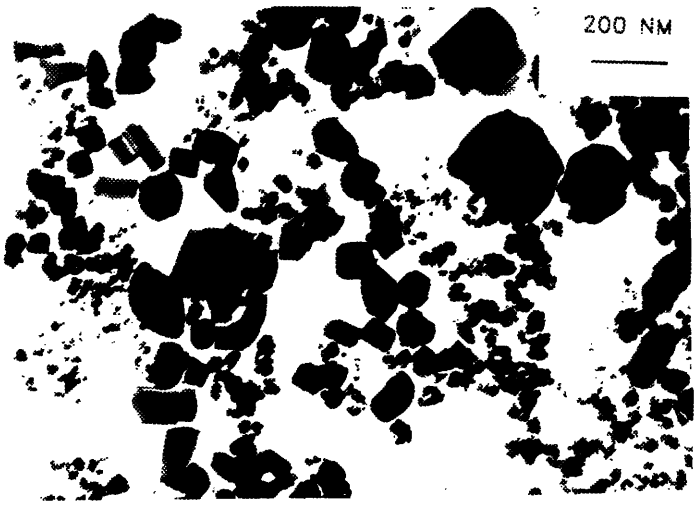

Figure 4. TEM photomicrograph of powder N31SN.

into silicon dimers and trimers.[7] The temperature and time interval of decomposition depend on the heating rate. At 10^6 K/sec, it takes 360 μsec for the silane to decompose (1% to 99%) at an average temperature of 1044°C. At a typical stream velocity of 0.5 m/s, the pyrolysis reactions go to completion in ~0.2 mm. The number density of these "initial" particles decreases rapidly as collisions result in particle growth; the particle growth rate depends on the Si concentration,[8,9] which is proportional to the system pressure since there is little mixing with the argon. Interparticle collision rates will start as high as 10^7/sec and decrease as particles grow by inelastic collisions. Our previous results[1,2] show that solid particles grow to a diameter of 10-20 nm before non-dispersible aggregates are formed. Typical number densities and collision rates are 10^{12}-10^{13}/cm^3 and 3 x 10^4/sec at these dimensions. Agglomerates form once sintering rates can no longer form dense, spherical particles in the time interval between collisions. If temperatures exceed the silicon melting point (1410°C), the agglomerates can once again coalesce into spherical silicon particles by a viscous flow process[9] and particle growth will continue.

Particle growth continues until the temperature decreases below 1410°C along a specific flow stream. Once the particles solidify, coalescence becomes impossible, and once they cool substantially below 1410°C, colliding particles no longer stick to one another. A variation in exposure times to T >1410°C produces a distribution of particle sizes in the powder. Flow streams that are never heated to 1410°C produce agglomerates of small particles. If the cooling rate from 1410°C is not high enough to reduce the particle temperature several hundred degrees in the period between interparticle collisions, aggregates of large particles can be produced. Therefore, the particle size and morphology distributions are directly attributable to the temperature and velocity distributions in the reaction zone. Uniform powder is produced only when all flow streams experience similar time-temperature-concentration histories.

Using the aerosol growth law developed by Lee,[8] we have calculated the particle size and size distribution expected from the collision and coalescence of molten particles in the temperature and velocity fields produced by laser heated decomposition of silane. Silicon powder F28S was modeled. Lee's solution assumes that along any flow stream the particle size distribution remains log-normal as the particles grow. He found that σ_g for that flow stream would rapidly converge to 1.355, consistent with the formation of a self-preserving distribution. For analysis, the reaction zone was divided into five concentric flow streams having approximately equal mass fluxes. The Si concentration of the outer streams can be diluted to account for SiH_4 mixing with the annular Ar and for thermophoresis.

The elapsed time each flow stream spent hotter than 1410°C was determined from a photograph of the F28S reaction zone that revealed the position of the boundary of the liquid to solid phase transition. An average stream velocity calculated from the reaction zone area measured from the photograph was used to calculate the elapsed times for T > 1410°C (5.8 ms to 23.2 ms), which are significantly longer than the times required for SiH_4 decomposition or for σ_g to converge to 1.355. Calculated temperature distributions from a fluid-flow model[5] were not sufficiently accurate to be used in the particle size calculation.

The individual mass distributions (dashed curves) calculated for each flow stream are shown in Figure 5 together with their sum (solid curve) which predicts the final particle size distribution. The outer region produced 110 nm particles, whereas those produced along the centerline averaged 350 nm.

For this calculation, the Si concentration in only the outer region was reduced by 70% to simulate intermixing with argon. The four interior regions, contributing 92% of the mass flux, were not diluted with argon. Diluting the outer region broadens the particle size distribution by contributing a large number of small particles. Two predicted distributions are compared to the measured particle size distribution of Si powder type F28S in Figure 6. The distribution represented by the solid curve was calculated assuming no intermixing of silane and argon. The dashed curve is the distribution shown in Figure 5. The excellent agreement in the average size and the shape of the distribution for the spherical particles confirms the accuracy of the silicon particle formation model.

The silicon powder synthesis model illustrates why it is difficult to achieve the time-temperature conditions that result in high-quality powder. Efficient conductive and radiant cooling of the outer flow streams tends to produce small particles and agglomerates. The prolonged, high temperatures along the centerline combined with the slow cooling rates tend to yield large particles that can be agglomerated. The least significant consequence of differences in cooling rates and mixing is a broadening of the particle size distribution. If all flow streams remained molten for the same length of time, σ_g would equal 1.355. Application of the model to run F28S conditions demonstrates that the variation in growth times and mixing with argon increases σ_g(mass) to 1.48 in agreement with experimental observation (see Table 1). A distribution of agglomerated powder sizes is a more serious consequence of incorrect t-T histories which precludes packing into dense green bodies.

SILICON CARBIDE POWDER FORMATION MODEL

High quality silicon carbide is formed from premixed streams of SiH_4 and CH_4 via a two step reaction mechanism.[3] Figure 3 is a TEM photomicrograph of a fully dispersible SiC powder (L6SC). The particles are polycrystalline, with apparently rough surfaces and range in size from 50 to 200 nm in diameter. They are not faceted and are basically equiaxed. These characteristics result from the following reaction mechanism.

The reactant gas mixture is heated by conduction as it approaches the CO_2 laser beam. By around 1050°C, the SiH_4 is fully decomposed and solid Si particles start to grow by collisions and coalescence in a H_2/CH_4 atmosphere. The temperature of the particle-CH_4-H_2 mixture continues to increase as the laser beam is approached. If the maximum temperature does not exceed ~1200°C, the resulting powder is mostly (>82%) unreacted, small diameter (~50 nm), agglomerated Si.[3]

Any combination of process conditions that increases the temperature further results in a sudden change in reaction zone temperature, structure and turbidity. Under these conditions, the maximum temperature jumps to at least 1600°C, and two bands appear in the reaction zone. Silicon particles form and grow in the lower band.[3] Typically the residence time in the lower band is ~3 ms allowing the Si particles to grow to 60-100 nm.[3,6] The temperature at the boundary between the lower and upper bands is apparently just over 1410°C, allowing the silicon particles to coalesce just before carburization becomes rapid. The temperature increases rapidly to the maximum value in the upper band; the sudden rise is caused by the combined effects of the exothermic carburization reaction that becomes rapid only at temperatures above 1400°C and by increased CO_2 laser absorption by the SiC particles. The rate controlling step for carburization is believed to be CH_4 pyrolysis;[3] grain boundary

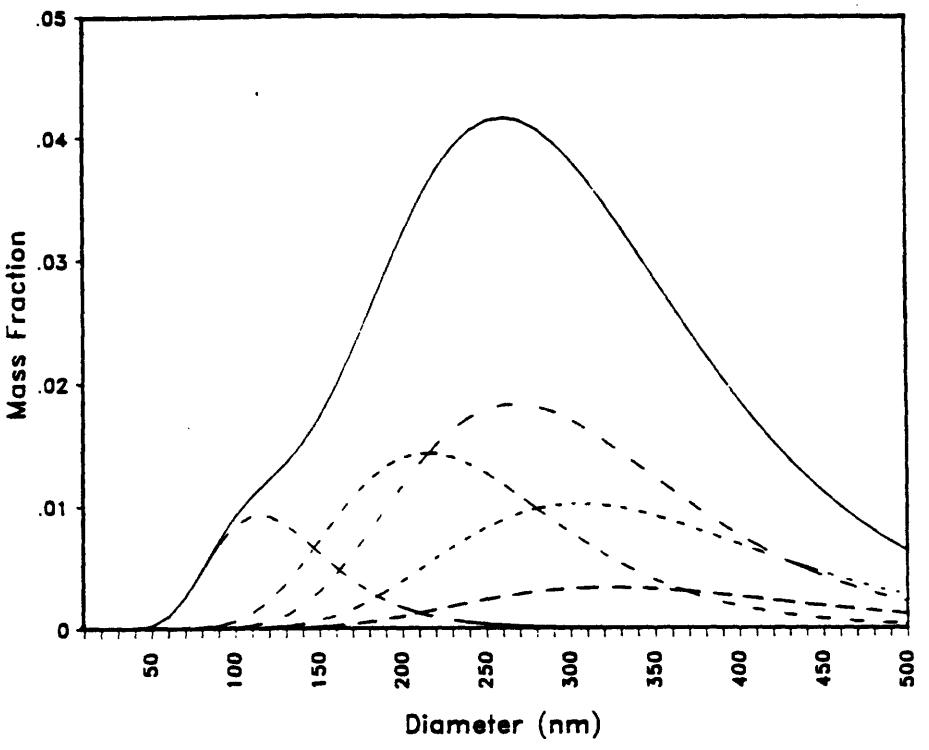

Figure 5. Individual mass distributions (dashed curves) calculated for each region of silicon reaction zone F28S, and their sum, the complete distribution (solid curve).

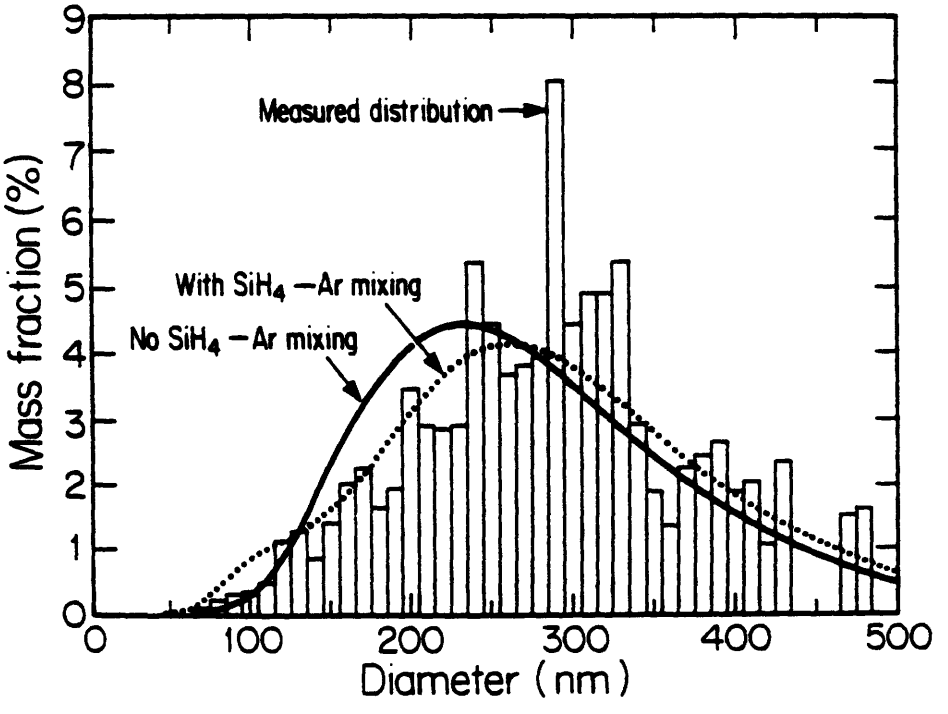

Figure 6. Histogram of the mass distribution of F28S Type III particles compared to the predicted distributions calculated with no mixing between the silane and the annular argon (solid curve), and with some mixing (dashed curve).

diffusion of Si through the SiC reaction layer is still rapid for these small, polycrystalline particles. Carburization of liquid Si particles at many nucleation sites apparently produces the rough surfaces visible in Figure 3.

Evidently the onset of the carburization reaction terminates the particle growth process. SiC is a solid at these temperatures, so coalescence by solid state diffusional processes is not possible on this time scale. The short time available between the beginning of Si particle formation and the onset of carburization is responsible for the maximum SiC particle size being ~100 nm instead of ~300 nm as in the case of silicon (Table 1). The C content of the powder depends on the reaction zone temperature and the SiH_4:CH_4 flow ratio.

Evidence for the two step reaction mechanism is the variation of the reaction zone turbidity (- ln(transmittance)) with distance from the nozzle.[3,4] Figure 7 shows how the turbidity varied for SiC run L30SC. The turbidity increases rapidly at the base of the reaction zone, reaches a maximum around 2 mm from the nozzle and then decreases as the hottest region of the reaction zone is reached. This variation is caused by the progressive formation then the conversion of the Si particles, which strongly attenuate the He-Ne laser probe beam, to SiC, which is relatively transparent.[4,10] After this decrease, the turbidity then levels off, or sometimes increases again, depending on the process conditions. A secondary increase in the turbidity probably results from making the powder C-rich, which also increases the imaginary component of the refractive index.

Only very small agglomerated particles are produced (~40 nm) when premixed streams of SiH_4 and C_2H_4 are used.[1,3] This results because C_2H_4 starts to carburize the Si particles at temperatures below the melting point of Si, preventing their coalescence and growth into larger spherical particles.

The laser synthesis of useful SiC powders depends on the correct combination of several temperature-dependent reaction rates. Carburization of liquid Si must be rapid since only a few milliseconds are available, but it must be delayed until the Si particles have had a chance to grow. Fortunately, the premixed SiH_4-CH_4 system satisfies these requirements and high-quality powder can be produced.

SILICON NITRIDE FORMATION MODEL

The synthesis of high-quality Si_3N_4[1,2,11] powder has proven to be more difficult than for Si or SiC powders. Premixed streams of laser heated SiH_4 and NH_3 can produce stoichiometric Si_3N_4 but the particles have been very small (20-30 nm) and highly agglomerated so they cannot be formed into high density green bodies. These characteristics result for reasons that are similar to issues encountered when making SiC from premixed SiH_4-C_2H_4 streams. NH_3 begins to react[12] with still solid Si particles at temperatures only slightly higher than the silane decomposition temperature, preventing the formation of large Si particles by coalescence of liquid particles.

SiH_4-N_2 mixtures were investigated[11] to determine whether the slow reaction kinetics typical of N_2 would allow a physical separation of the Si particle formation and growth step from the nitridation step. Unfortunately, the N_2 proved so inhibited that negligible nitridation occurred in the few millisecond exposure.

Larger Si_3N_4 powders have been synthesized successfully (Table 1) by injecting ammonia into SiH_4 reaction zones.[11] The physical separation of the nitrogen source from the SiH_4 decomposition region permits the required Si particle growth by collision-coalescence prior to the onset of nitridation. Figure 4 is a TEM photomicrograph of powder N31SN which is approximately 98%

Si_3N_4 (~50% α and ~50% β). It was produced by injecting 200 sccm of NH_3 into a SiH_4 reaction zone 0.5 mm above the center of the CO_2 laser beam. The reaction zone temperature was ~1600°C. Figure 4 shows that many large particles were produced. Their morphology is often faceted and elongated in contrast to the SiC particles that are equiaxed indicating that the nitriding mechanism probably differs fundamentally from the carburizing mechanism.

The Si_3N_4 particle size distribution is also broader ($\sigma_{g\ (mass)} = 1.8$) than the other optimized powders. The distribution of particle sizes probably results from radial concentration gradients since the NH_3 is injected from outside of the reaction zone. Powder on the outer edge of the powder plume was nitrided first, while still small. The silicon particles in the center continued to grow, reaching a larger size as the NH_3 diffused inward. Growth stops when nitridation begins.

CONCLUSIONS

Analyses of Si, SiC and Si_3N_4 powder synthesis conditions needed to produce 0.1-0.2 μm, non-agglomerated particles have shown that the growth process occurs by a collision and coalescence process. The solid-state coalescence process proceeds as fast as the collision process only up to particle dimensions on the order of 20nm. For larger particles under high mass flow rate conditions, growth must proceed by collisions between molten particles. With Si, this is accomplished simply by raising the reaction temperature above the melting temperature for an appropriate interval. For the compounds, the reactions must be made to occur in two steps; Si particles form and grow in the first and compounds form in the second. The separation of the two steps can be made to occur in both premixed and injected reactant streams. For both elements and compounds, the particles must be quenched at high rates to avoid formation of bonds between particles after desired diameters have been reached. Using correct synthesis conditions, fully dispersible powders of all three materials were made and formed into high density green parts.

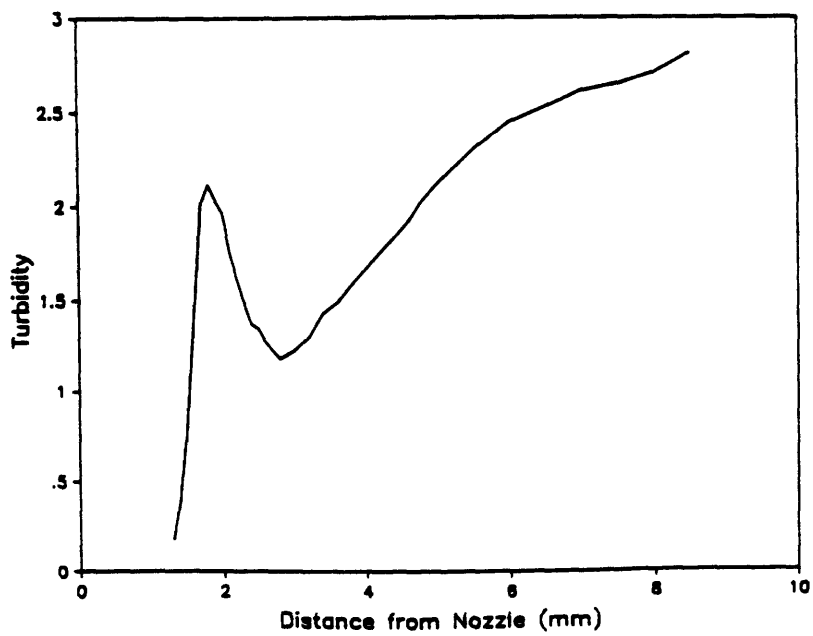

Figure 7. The turbidity of silicon carbide reaction zone L30SC as a function of the distance from the reactant gas nozzle.

ACKNOWLEDGEMENTS

This research was supported by DOD, NASA-Lewis, and an industrial consortium including ABEX Corp., Aisin Seiki Co., Alcoa, NGK Spark Plug Co., Nippon Steel, Sumitomo Electric Industries, Ltd., The Japan Steel Works, Ltd., and Toa Nenryo Kogyo K.K.. Their support is gratefully acknowledged.

REFERENCES

1. Cannon, W. R., Danforth, S. C., Flint, J. H., Haggerty, J. S., Marra, R. A., "Sinterable Ceramic Powders from Laser Driven Reactions, Part I; Process Description and Modeling," J. Am. Ceram. Soc., 65 [7], 324-30 (1982).
2. Cannon, W. R., Danforth, S. C., Haggerty, J. S., Marra, R.A., "Sinterable Ceramic Powders from Laser Driven Reactions, Part II; Powder Characteristics and Process Variables," J. Am. Ceram. Soc., 65 [7], 330-5 (1982).
3. Sawano, K., Haggerty, J. S. and Bowen, H. K., "Formation of SiC Powder from Laser Heated Vapor Phase Reactions," Yogyo-Kyokai-Shi (J. of Ceram. Soc. Japan), 95 [1], 64-9 (1987).
4. Flint, J. H., Marra, R. A. and Haggerty, J. S., "Powder Temperature, Size, and Number Density in Laser Driven Reactions," Aerosol Sci. and Tech., 5, 249-261 (1986).
5. Akmandor, I. S., "Theoretical and Computational Models of Reacting Silane Gas Flows: Laser Driven Pyrolysis of Subsonic and Supersonic Jets," Ph.D. Thesis, MIT, 1985.
6. Flint, J. H. and Haggerty, J.S., "A Model for the Growth of Silicon Particles from Laser-Heated Gases," submitted to Aerosol Science and Technology.
7. Coltrin, M. E., Kee, R. J. and Miller, J. A., "A Mathematical Model of the Coupled Fluid Mechanics and Chemical Kinetics in a Chemical Vapor Deposition Reactor," J. Electrochm. Soc., 131, 425-434 (1984).
8. Lee, K. W., Chen, H. and Gieseke, J. A., "Log-Normally Preserving Size Distribution for Brownian Coagultion in the Free-Molecule Regime," Aerosol Sci. and Tech., 3, 53-62 (1984).
9. Ulrich, G. D. and Subramanian, N. S., "Particle Growth in Flames, III. Coalescence as a Rate-Controlling Process," Combustion Sciences and Technology, 17, 210-26 (1977).
10. Philip, H. R. and Taft, E. A., "Intrinsic Optical Absorption in Single Crystal Silicon Carbide," in Silicon Carbide, J. R. O'Connor and J. Smittens (eds.), Smiltens, Pergamon Press, New York NY, 1960.
11. Aoki, M., Flint, J. H. and Haggerty, J. S., "Laser Synthesis of Silicon Nitride Powders for Ceramic Processing," to be published in Proceedings of the First International Conference on Ceramic Powder Processing Science, Orlando FL, Nov. 1987.
12. Yumura, M., Asaba, T., Matsumoto, Y., and Matsui, H., "Thermal Decomposition of Ammonia in Shock Waves," Intl. J. Chem. Kinetics, 12, 439 (1980).

Powder Temperature, Size, and Number Density in Laser-Driven Reactions

John H. Flint, Robert A. Marra,* and John S. Haggerty
Massachusetts Institute of Technology, 12-009 Cambridge, MA 02139

A technique to accurately measure the temperature of powders in a laser-driven reaction has been developed. Particles are formed by heating reactant gases with a 150-W CO_2 laser. The brightness temperature of the particulate cloud was measured with a micro-optical pyrometer. The emissivity was determined from scattering and transmission measurements. A correction for high turbidity was derived. The scattering and transmission measurements also allow the determination of the size and number density of the particles. The temperature and particle size as a function of height are reported for five silicon powder reaction conditions, and for one silicon carbide reaction. The measurements indicate that particles are often nucleated before the reactant gas has reached the CO_2 laser beam. The reaction zone temperature decreases once most of the reactant gas is consumed, unless the produced powder absorbs 10.6 μm radiation as does SiC. The silicon particles nucleate as amorphous silicon, and then crystallize as they move into hotter regions of the reaction zone.

INTRODUCTION

A method of producing sinterable powders through the heating of gases with a CO_2 laser has been developed which has potential application in the manufacture of silicon nitride and silicon carbide as well as other high-temperature ceramics (Cannon et al., 1982a, b; Suyama et al., 1985). Although variations in the product powder characteristics have been studied extensively as a function of process parameters, the properties of the reaction itself have been more difficult to characterize. The most important of these properties are the thermal range within which the reaction takes place, and the evolution in time (and space) of the particle size, particle number density, and crystallinity.

This paper describes a technique that has been developed and used to rapidly and accurately measure these properties with a spatial resolution of 1 mm. Results for the laser synthesis of silicon and silicon carbide powders are also presented.

EXPERIMENTAL APPARATUS AND METHODOLOGY

The powder synthesis process involves passing a jet of reactant gases through a CW CO_2 laser beam inside a controlled atmosphere reaction cell. Figure 1 is a schematic of the reaction zone. The reactant gases and the CO_2 laser beam intersect at the center of the cell. The gas is heated rapidly, and reacts to form small particles, which are swept out of the cell and captured in a filter. Argon is injected in a concentric annular flow at the base of the nozzle to constrain the reactant gases in a narrow stream and to carry the products to the filter.

By this method, silane gas is converted into silicon powder by the simple overall reaction

$$SiH_4(g) \rightarrow 2H_2(g) + Si(s).$$

The resulting silicon powder is ideal for form-

*Present Address: Alcoa Technical Center Alcoa Center, PA 15069.

Aerosol Science and Technology 5:249–260 (1986)
© 1986 Elsevier Science Publishing Co., Inc.

0278-6826/86/$3.50

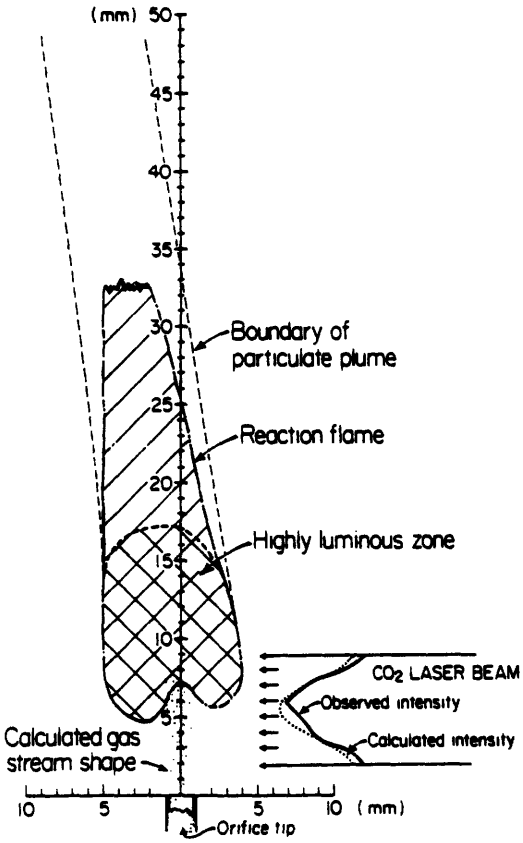

FIGURE 1. Schematic of the reaction zone.

ing reaction-bonded silicon nitride because of its small particle size (10–250 nm diameter depending on process parameters), very narrow size distribution, high purity, and loose agglomeration. The same technique has been used to produce silicon nitride (Cannon et al., 1982a, b) and silicon carbide powders (Suyama et al., 1985).

To measure the process parameters of interest, an apparatus based on a He–Ne probe laser was developed. The extinction and scattering of the polarized He–Ne beam by the cloud of particles provide the needed data (D'Alessio et al., 1975), by the following methodology.

Optical pyrometry determines the brightness temperature, S, of a radiating body, at a single wavelength. The absolute emissivity, ϵ, of the area being viewed must be known before the true temperature can be calculated. This can be readily seen from Wien's approximation to the Planck radiation law (Rutgers and Devos, 1954) written in terms of the radiance N_λ, and the brightness temperature, S, and the true temperature, T:

$$N_\lambda = \frac{C_1 \epsilon e^{(-C_2/\lambda T)}}{\lambda^5} = \frac{C_1 e^{(-C_2/\lambda S)}}{\lambda^5}. \quad (1)$$

If the emissivity is known, the true temperature T can be found by rearranging Eq. (1) to yield

$$\frac{1}{T} = \frac{1}{S} + \frac{\lambda \ln \epsilon}{C_2}. \quad (2)$$

The accuracy of the true temperature calculation is essentially equal to the accuracy of the brightness temperature measurement ($\pm 10°C$). This is because the emissivity calculations are insensitive to the only quantity that is not directly measured, the index of refraction of the particles.

The emissivity of a body is given by its absorptivity,

$$\epsilon = \alpha = 1 - t - \rho, \quad (3)$$

which is the fraction of incident light that is neither reflected, ρ, nor transmitted, t. For a diffuse cloud of particles such as exists in the reactions of interest, light is scattered in many directions rather than reflected as one wave. Thus, the emissivity of a cloud is (Lowes and Newall, 1974)

$$\epsilon = (1 - t)\left(\frac{C_{abs}}{C_{ext}}\right), \quad (4)$$

where C_{ext} and C_{abs} are, respectively, the extinction and absorption cross sections per particle. The integrated scattering cross section C_{sca} is related to C_{abs} and C_{ext} by

$$C_{sca} = C_{ext} - C_{abs}. \quad (5)$$

The cross sections are functions of the wavelength, the particle size, and the complex index of refraction, $m = n - ik$, of the particles, and can be calculated using the Lorenz–Mie scattering equations (Kerker, 1969). C_{ext} is related to the transmissivity

through

$$t = \frac{I}{I_0} = \exp(-lNC_{ext}), \tag{6}$$

where I_0 and I are the incident and transmitted intensities, N is the particle number density, and l is the thickness of the cloud. Using these substitutions, Eq. (4) can be rewritten as

$$\epsilon = \left(1 - \frac{I}{I_0}\right)\left(1 - \frac{C_{sca}}{C_{ext}}\right). \tag{7}$$

The first term is determined from a transmission measurement. The second term requires that the scatter–extinction ratio be measured.

If the incident and scattered light are plane polarized orthogonal to the scattering plane, the scatter–extinction ratio is defined by

$$\frac{\dot{E}_\perp(\theta)}{E_0 \delta\Omega \ln(I_0/I)} = \frac{\lambda^2 i_\perp(\theta)}{4\pi^2 C_{ext}}, \tag{8}$$

where the quantities on the left-hand side are measurable, and those on the right-hand side are calculable. $\dot{E}_\perp(\theta)$ is the power scattered at angle θ into solid angle $\delta\Omega$ for an incident power of E_0, and $i_\perp(\theta)$ is the Mie scattering function for light scattered at angle θ. Equation (8) is written for the case where the transmission and scattering measurements are made simultaneously, so that the path length and number density dependencies cancel. The Mie scattering function, $i_\perp(\theta)$, depends on the particle radius, the particle index of refraction, and the wavelength of incident light (Kerker, 1969).

Values for C_{ext}, C_{sca}, and $i_\perp(\theta)$ were calculated as a function of particle radius for the values of θ and λ used in the experiment with an appropriate index of refraction. The results of this calculation are plotted as C_{sca}/C_{ext} versus $\lambda^2 i_\perp(\theta)/4\pi^2 C_{ext}$. The value of C_{sca}/C_{ext} corresponding to an experimentally measured scatter–extinction ratio is then determined from this plot. The emissivity of the portion of the cloud on which the transmission and scattering measurements were made can then be calculated from Eq. (7). The particle size can be determined from a plot of the scatter–extinction ratio versus particle size. The cross sections C_{ext} and C_{sca} can be found using similar plots. Once C_{ext} and the width of the cloud have been determined, the particle number density can be calculated using Eq. (6).

The Lorenz–Mie scattering theory can be applied to the scattering of light by a cloud of spherical particles if the following three conditions are met (Jones, 1979):

1. Each particle scatters separately; that is, the particles are not agglomerated, and are separated by at least three radii (Kerker, 1969);
2. There is no optical interference among different scattered waves;
3. There is no multiple scattering.

It will be shown in the fourth section that condition 1 is true. Condition 2 is almost always valid for random systems (Jones, 1979). But, condition 3 requires that the turbidity be less than 0.1 (Kerker, 1969) and is not generally met by regions of the clouds of particles under study.

The most significant result of high turbidity is a *reduction* of the scattered power $\dot{E}_\perp(\theta)$ because both the probe beam and the scattered light from the interior of the cloud are attenuated. For small-angle scattering, this effect reduces the scattered power by a factor of $[1 - (I/I_0)^2]/2\ln(I_0/I)$. (See Appendix A for the derivation of this correction.) Therefore, using $2\dot{E}_\perp(\theta)\ln(I_0/I)/[1 - (I/I_0)^2]$ in place of $\dot{E}_\perp(\theta)$ in Eq. (8) allows the use of the Mie scattering theory in spite of the reduction in scattered light caused by high turbidity.

The other result of high turbidity is that it leads to multiple scattering, which *increases* the scattered power $\dot{E}_\perp(\theta)$. This effect is more difficult to account for analytically. Luckily, small silicon particles absorb rather than scatter red light. For example, for $m = 4.38 - 0.26i$, the scattering cross section of a 24-nm radius particle is one third of its absorption cross section. Therefore, the correc-

tion derived in Appendix A will be most valid for smaller particles.

All of the calculations assume a monodisperse particle distribution. The laser process produces fairly narrow distributions (σ/mean ~ 0.3) (Cannon et al., 1982b). Since the scattering cross section increases rapidly with particle size, calculated sizes will be somewhat larger than the actual average particle size (Koon Gee Neoh, 1980).

The optical properties of silicon have been studied extensively. In the visible region of the spectrum, the complex index of refraction ($m = n - ik$) varies strongly with wavelength, temperature, and degree of crystallinity (Dash and Newman, 1955; Kuhl et al., 1974; Janai and Karlson, 1979). Since the powders being studied are changing temperature rapidly, and perhaps crystallizing as they grow, a series of calculations were performed using various possible values of m.

Figures 2 and 3 were generated from computer calculations (Koon Gee Neoh, 1980) of the Mie scattering functions and cross sections using three different values for the index of refraction. An index of $m = 4.1 - 0.113i$ is appropriate for polycrystalline silicon at 500°C, and $m = 4.38 - 0.99i$ is for amorphous silicon at 500°C (Janai and Karlson, 1979). An extrapolated value of $m = 4.38 - 0.26i$ should be valid for polycrystalline silicon around 1100°C or for a polycrystalline–amorphous mix at some lower temperature. Figure 2 shows the calculated scatter–extinction ratios versus C_{sca}/C_{ext} for $\theta = 20°$. It is apparent that the relationship between the scatter–extinction ratio and C_{sca}/C_{ext} is independent of the index up to a ratio of approximately 0.025. The C_{sca}/C_{ext} values remain close to one another for the two polycrystalline indices for higher values of the ratio. At a scatter–extinction ratio of 0.04, the maximum uncertainty in ϵ results in a true temperature difference of only 26°C for a brightness temperature of 1100°C (~ 2.5%). This indicates that even though the index as a function of position in the reaction zone is not precisely known, the emissivity and the temperature can still be determined to high accuracy.

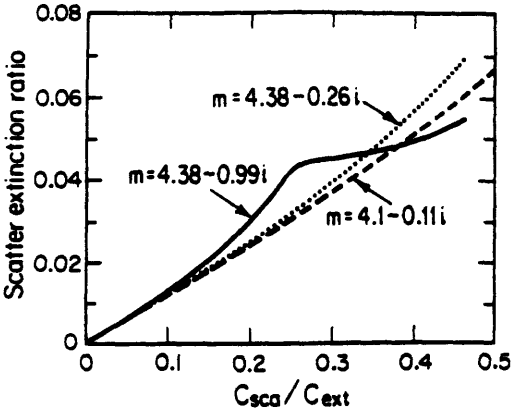

FIGURE 2. Scatter–extinction ratio versus C_{sca}/C_{ext}.

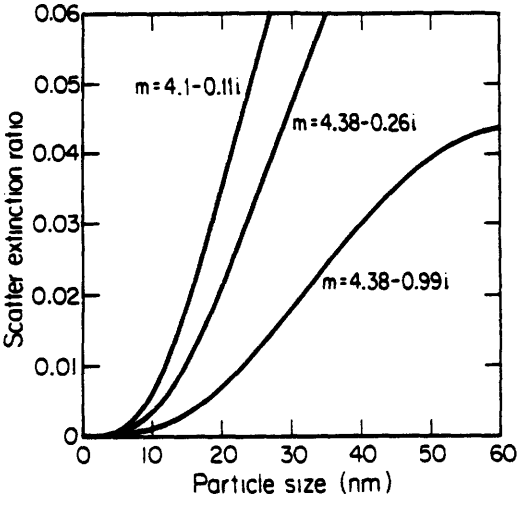

FIGURE 3. Scatter–extinction ratio versus particle radius.

Figure 3 is a plot of the scatter–extinction ratio versus particle radius for the same three indices. A much larger dependence on index is noted. Although this introduces some uncertainty to the absolute particle size and number density calculations, this is not a serious problem since the final particle size can be measured by BET surface area analysis and transmission electron microscopy.

Without question, the scatter–extinction measurements can be used to monitor changes in particle size and number density throughout the reaction. It may also be possible to extract information on the variation of the index of refraction of the particles within the reaction zone from the scatter–extinction measurements as a function of position.

EXPERIMENTAL PROCEDURE

A He–Ne laser is used as the probe in an apparatus that simultaneously measures the extinction of the He–Ne laser beam and the intensity of the scattered light at an angle of 20°. Figure 4 is a schematic of the optical layout.

The 5-mW vertically polarized He–Ne laser is mounted on a cathetometer, enabling measurements to be made as a function of height by simply translating the laser. The transmitted He–Ne laser light, I, is measured by a silicon photodiode mounted on an x–y translator. The scattered He–Ne light, $\dot{E}_{\perp}(20°)$, is detected by an RCA C53050 photomultiplier. An 8.13-mm-diam aperture determines the solid angle viewed, which is 2.23×10^{-4} sr. Focusing optics are not used to minimize alignment problems as the probe laser is moved. A 632.8-nm bandpass filter passes the He–Ne laser light, but rejects most of the thermal emission from the reaction zone. A vertical polarizer analyzes the polarization of the scattered light. The incident probe laser power, E_0, was measured by directing a calibrated fraction of the He–Ne laser beam through the same collection filters to the photomultiplier using a beam splitter temporarily mounted at the center of the reaction cell.

A micro-optical pyrometer (made by Pyrometer Instruments, Inc.) is mounted alongside the photodiode so that it views the reaction zone in the scattering plane. The field of view of the pyrometer is such that a 1-mm^2 area is monitored. The sensitivity peak of the pyrometer (650 nm) is sufficiently close to 632.8 nm that no correction was needed for variation of the optical properties of the powder over this range.

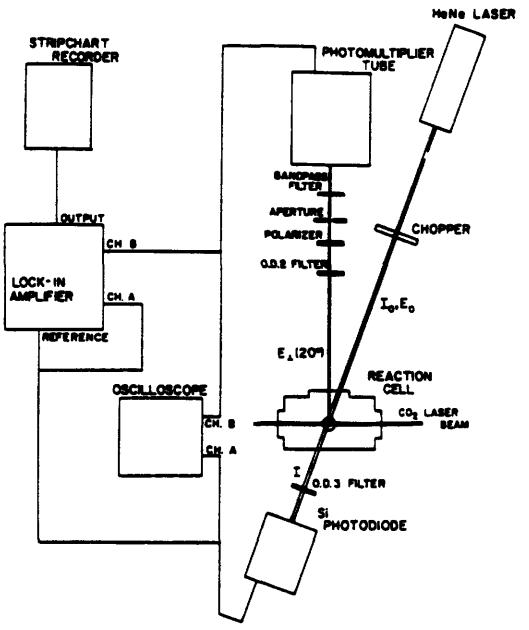

FIGURE 4. Scatter–extinction optical layout.

At each height the following sequence of adjustments and measurements is required: the cathetometer is set to the desired height: the photodiode is adjusted with its x–y translator for peak signal; I and $\dot{E}_{\perp}(20°)$ are measured with the lock-in amplifier; the optical pyrometer is focused on the point where the He–Ne beam intersects the reaction zone, then the He–Ne laser is blocked while a temperature reading is made. In this way the scattering, extinction, and brightness temperature measurements are all made on the identical volume of the reaction zone.

RESULTS AND DISCUSSION

Measurements were made on laser-heated silicon powder synthesis reactions under a range of process conditions. Table 1 lists the parameters of the reactions studied and the equivalent particle sizes determined by BET surface area analysis for similar runs

TABLE 1. Powder Synthesis Reactions Studied

Run No.	Cell pressure (atm)	Reactant Gas Flow Rates: Silane (cm^3/min)	Argon (cm^3/min)	C_2H_4 (cm^3/min)	Radius by BET (nm)	Maximum turbidity	Height $\tau = 0.25$ (mm)
631S	0.2	38	0	0	30.5	2.08	3.0
654S	0.2	13	25	0	17.5	0.325	8.5
634S	0.2	6.5	31	0	14.8	0.095	—
630S	0.2	109	0	0	22.2	1.59	7
650S	0.6	66	0	0	73.5	5.83	2.75
910SiC	0.6	36	0	20	17.0	0.66	3.0

(Cannon et al., 1982a, b). The maximum turbidity and the height above the nozzle where the turbidity reaches 0.25 are also listed.

Figure 5 is the measured scattered power, $\dot{E}_\perp(20°)$, and transmitted intensity, I, in millivolts RMS for run 631S as a function of position above the reactant gas nozzle. The scatter–extinction ratio is also plotted. Figure 6 shows the emissivity, ϵ, the brightness temperature, S, and the true temperature, T, as a function of position for the same reaction. Figure 7 shows, ϵ, S, and T for run 654S. These plots are representative of the data from the other runs. Figure 8 summarizes the true temperature distributions for all of the reactions studied. Figure 9 summarizes the calculated particle sizes.

The number density of particles as a function of position in the reaction zone is presented in Figure 10 for run 654S. Two different calculations are presented, since the calculated number density is a strong function of the value of the index of refraction used.

Figures 8 and 9 reveal that the heating of the reactants is rapid, and the reaction is often underway before the reactants intersect the CO_2 laser beam. In the case of runs 650S and 631S, the measured temperatures at the edge of the laser beam are over 900°C.

Possible heating mechanisms of the gas below the CO_2 laser beam are thermal conduction from the hot zone, and resonant emission from vibrationally excited SiH_4 molecules in the hot zone. The maximum rate of infrared emission from the reaction zone can be calculated from the Planck radiation law. At $\lambda = 4$ μm, and 1100°C, the emission rate is about 3 W/cm^2/μm. If the

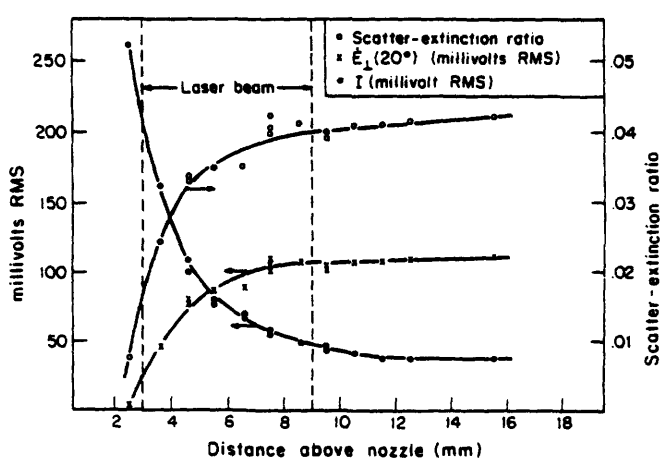

FIGURE 5. I, $\dot{E}_\perp$ (20°), and scatter–extinction ratio for run 631S.

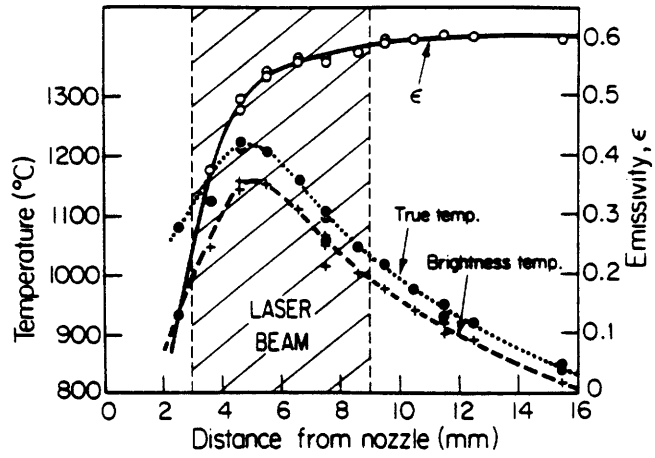

FIGURE 6. Temperature and emissivity for run 631S.

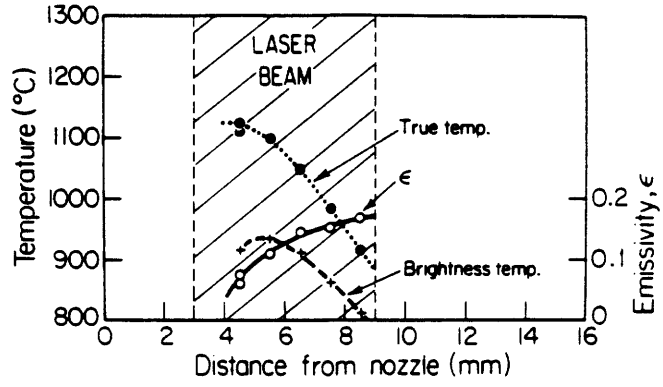

FIGURE 7. Temperature and emissivity for run 654S.

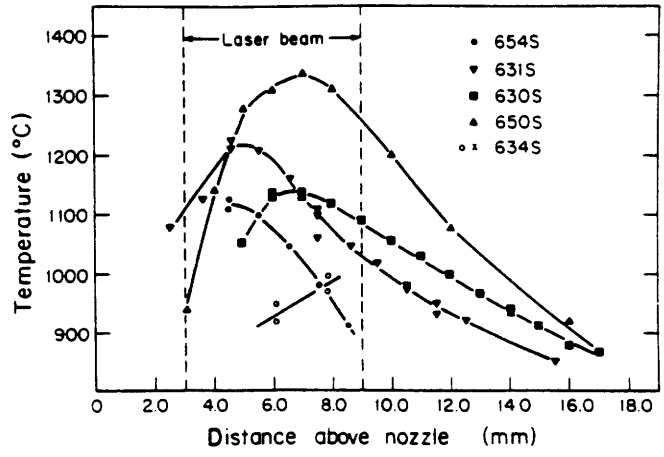

FIGURE 8. Temperature versus distance from nozzle.

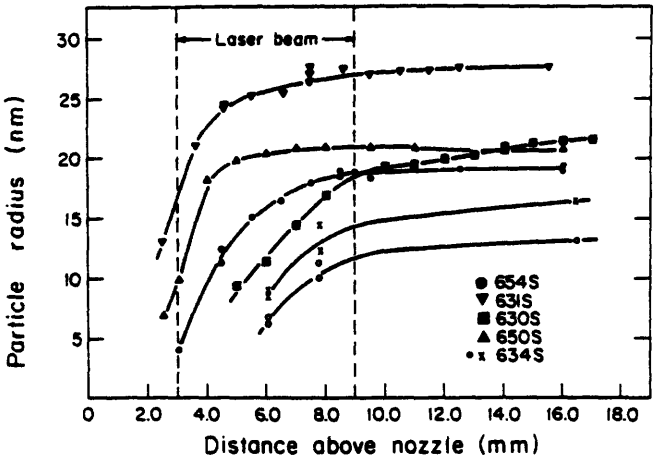

FIGURE 9. Particle size versus distance from nozzle.

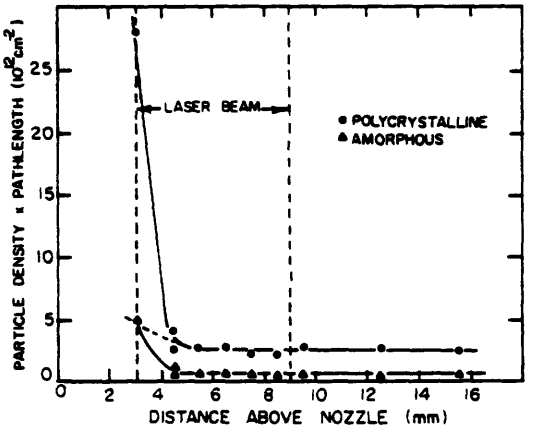

FIGURE 10. Particle number density versus distance from nozzle.

width of the 4-μm silane absorption band is 0.33 μm. 1.0 W/cm^2 could be transferred by radiation. Hot bands and the 10-μm band will also contribute to some extent. Thermal conductivity across a 3-mm gap of silane is about 2 W/cm^2 for a 1000°C temperature difference. From this simple analysis it appears that both thermal conductivity and vibrational radiation from excited silane molecules are significant in the preheating of the reactants.

Figure 8 also indicates that for all reaction conditions studied, the temperature of the silicon powder begins decreasing while the particles are still in the CO_2 laser beam, suggesting that the particles themselves are not strongly heated by the laser. Once most or all of the silane has reacted to form solid silicon, the gas–powder mixture stops absorbing and starts to cool off. The half-life of a silane molecule is only 10 μsec at 1200°C (Coltrin et al., 1984), which explains why most of it is consumed at temperatures significantly below the silicon melting point.

Since the particle size determinations are sensitive to the index of refraction, the quantitative conclusions based on these measurements must be more tentative. It is clear that the particles grow rapidly, and that the growth process usually terminates within the CO_2 laser beam volume. Significant growth past the laser beam only occurs at the high flow rates (as in run 630S). For the undiluted 0.2-atm runs, agreement between these measurements and BET size measurements is good, suggesting that the polycrystalline indices extrapolated above 500°C are the best choice. For diluted reactions, which are not as hot, better agreement is obtained when the lower temperature indices are used. The overall good agreement indicates that the high turbidity correction is reasonably good for turbidities up to about 2.

The run at 0.6 atm (650S) requires additional interpretation. The measured particle size is much smaller than the BET re-

sults. However, since the final turbidity of this reaction is almost 6, it is quite possible that the turbidity correction is not accurate at very high turbidities. The other two conditions for the validity of Mie scattering should still hold. Large turbidity should produce multiple scattering, resulting in a larger scatter–extinction ratio, and a larger calculated particle size. Interestingly, just the opposite is observed. On the other hand, for such a turbid cloud virtually all of the detected scattering comes from the outer edge, where the silane reactant is the most strongly diluted with argon. Since diluted conditions produced smaller particles, it is likely that small particles are created at the edges of the reaction zone. The effect of this would be to reduce the scatter–extinction ratio, leading to a small calculated particle size.

Finally, the leveling off of the scatter–extinction ratio, hence the particle size, under all conditions indicates that the large loose agglomerates that are typical of the powder after it has been collected in the filter are produced by the collection process. This justifies the assumption that condition 1 for Mie scattering is valid. It also suggests that a liquid collection process should produce a monodisperse suspension of silicon particles. This would allow the fabrication of uniform high-density compacts, which would have much improved sintering properties.

The particle number density calculations are extremely sensitive to the value of the refractive index used in the calculation. A calculation based on a constant index indicates that the number density decreases from a maximum value at the inception of the reaction to a constant value (Figure 10). Several factors can contribute to the apparent decrease in number density from levels calculated at the base of the reaction zone. Although expansion of the reactant gases with heating is a factor, the number density change is too great for this to be solely responsible. Small particles could be agglomerating as they move into the CO_2 laser beam. We feel this is unlikely because there is no reason why the agglomeration process would terminate abruptly, particularly before the reaction had neared completion. Figure 9 shows that the major portion of the reaction occurs via growth after the number density has reached a constant value. The final explanation is that the particles are amorphous at the base of the reaction zone and crystallize as they grow while traveling into the hotter regions of the zone. Under this assumption, the number density curve would be a combination of the amorphous curve and the polycrystalline curve, as shown by the dashed line in Figure 10. The transition corresponds to the region within the zone where the amorphous particles crystallize. The temperature at the end of the transition, 4.5 mm from the nozzle, was 1120°C. At the beginning point, 3 mm from the nozzle, the reaction zone was not luminous, so the temperature there is unknown. A linear extrapolation of the temperature indicates 750°C, which is probably an upper limit. Because of the large growth rates, and the short length of time at this low temperature, 750°C is consistent with the formation of amorphous silicon. However, 1120°C is so far above the crystallization temperature of silicon (~ 650°C), that the particles are certainly polycrystalline by that point. The formation of amorphous powders and their progressive crystallization is therefore probably responsible for the apparent number density decrease with height when a constant refractive index is assumed. The dashed line in Figure 10 indicates a relatively constant number density.

Preliminary scatter–extinction and temperature measurements have been performed on SiC powders made from SiH_4 and C_2H_4. Figure 11 shows the brightness temperature, true temperature, and emissivity for a typical silicon carbide synthesis run. The run conditions are listed in Table 1. As was observed in the silane reaction, the heating of the reactants is very rapid and the reaction is initiated significantly before the reactants enter the laser beam. The emissivity increased

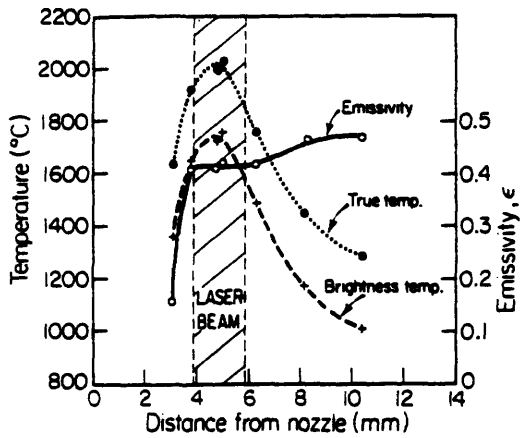

FIGURE 11. Temperature and emissivity for run No. 910SiC.

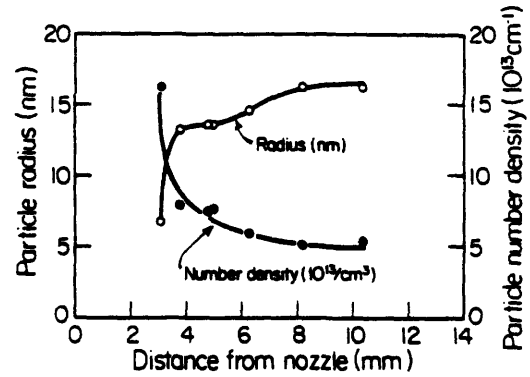

FIGURE 12. Particle size and number density for run No. 910SiC.

rapidly until a nearly constant value was achieved. The temperature distribution within the laser-irradiated region was sufficiently similar in shape to the Gaussian intensity distribution of the laser beam to suggest that the SiC particles are heated directly by the CO_2 laser beam.

The calculated particle radius is shown in Figure 12. The high-temperature optical properties of SiC (Nishino et al., 1975) are not precisely known, and the imaginary part varies strongly with small departures from stoichiometry. Therefore a series of calculations using various values for the refractive index was carried out; the set of calculations that produces a final particle size that agrees the closest with the BET value is plotted in Figure 12. It is evident that the nucleation and growth processes are nearly complete by the time the particles reach the laser beam, suggesting a very rapid growth rate. Better data on the SiC optical properties should enable more accurate comparisons between the scatter–extinction results and the particle size determined by other analytical techniques.

Figure 12 also shows a plot of the particle number density, N, as a function of position in the reaction zone. The calculated number density decreases from a maximum value at the base of the reaction zone and continues to decrease slightly as the particles travel further from the inlet nozzle. The decrease in particle number density may indicate the particles are agglomerating within the reaction zone, or, as suggested in the silicon synthesis, the particles may initially form as amorphous SiC and crystallize in the hotter regions of the reaction zone. A transition from silicon rich to nearly stoichiometric SiC would also explain this decrease. A more detailed study is required to interpret these results with respect to the particle formation mechanisms.

CONCLUSION

The analytical techniques presented here are applicable to the accurate determination of the temperature distribution and average particle size and number density of a cloud of particulates, including silicon, silicon carbide, or silicon nitride, produced in a CO_2 laser-driven reaction. While the technique has been primarily used to study the production of Si powder from silane gas, an equivalent study of the SiC and Si_3N_4 reactions requires only some idea of their high-temperature optical properties. This technique is relatively insensitive to the optical thickness of the cloud, or to whether the individual particles primarily absorb or scatter light (although a finite absorption cross section is required).

This research was funded by ONR/ARO under contract No. N00014-82-K-0350, 1982–1984, and by NASA/Lewis under contract No. NSG 7645. We would like to thank Professor Adel Sarofim for the gift of the computer program and helpful discussions. We are also indebted to Professor Tom Eager for the loan of the He–Ne laser and for letting us use his computer facility, and to Professor Kent Bowen.

APPENDIX A: CORRECTION FOR HIGH TURBIDITY IN SCATTERING MEASUREMENTS

The derivations from Lorenz–Mie scattering theory are valid only when the three conditions cited in the text for single scattering are met. If the probe beam is attenuated significantly by the cloud, the last volume element will experience an incident power less than E_0, so it will scatter less light than does the first volume element. In small-angle scattering, the light from the last volume element of the cloud will have to travel back through the cloud, being further attenuated. From Lorenz–Mie theory, the light scattered at position p, $\dot{E}(\theta, p)$ is

$$\dot{E}(\theta, p) = NC_{sca}(\theta)E(p)\,\delta\Omega\,\delta v, \qquad (A.1)$$

where N is the particle number density, $C_{sca}(\theta)$ is the scattering cross section at angle θ, $E(p)$ is the probe power at position p, and $\delta\Omega$ and δp are the solid-angle and volume depth, respectively. If the cloud is optically thin, $E(p) = E_0$, and the scattered light is not attenuated as it leaves the cloud, so the total scattered light from the entire cloud of thickness D is

$$\dot{E}(\theta) = \int_0^D \dot{E}(\theta, p)\,dp = NC_{sca}(\theta)E_0\,\delta\Omega\,D. \qquad (A.2)$$

If the cloud is not optically thin, then the power at position p is

$$E(p) = E_0 e^{-NC_{ext}p} \qquad (A.3)$$

and the scattered light is attenuated by $e^{-NC_{ext}L}$, where L is the distance out of the cloud at an angle θ from position p. Figure A.1 illustrates these relations for a circular cloud with the probe beam passing along the diameter, D. The total scattered power is

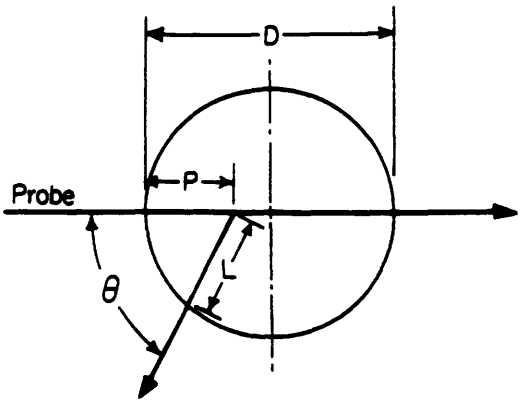

FIGURE A.1. Scattering diagram with cylindrical symmetry.

$$\dot{E}(\theta) = \int_0^D \dot{E}(\theta, p)\,dp = \int_0^D NC_{sca}(\theta)\,\delta\Omega \times E_0 e^{-NC_{ext}p} e^{-NC_{ext}L}\,dp. \qquad (A.4)$$

For $\theta = 20°$, L is equal to p within 5% so Eq. (A.4) can be integrated:

$$\dot{E}(\theta) = NC_{sca}(\theta)\,\delta\Omega\,E_0 \int_0^D e^{-2NC_{ext}p}\,dp = NC_{sca}(\theta)\,\delta\Omega\,E_0 D\left(\frac{1 - e^{-2NC_{ext}D}}{2NC_{ext}D}\right). \qquad (A.5)$$

From the Beer–Lambert relation:

$$\frac{I}{I_0} = e^{-NC_{ext}D} \qquad (A.6)$$

or

$$\ln(I_0/I) = NC_{ext}D. \qquad (A.7)$$

Equation (A.5) can therefore be rewritten as

$$\dot{E}(\theta) = NC_{sca}(\theta)\,\delta\Omega\,E_0 D\left[\frac{1 - (I/I_0)^2}{2\ln(I_0/I)}\right]. \qquad (A.8)$$

For the case where the incident and scattered waves are orthogonal to the scattering plane,

$(\lambda^2/4\pi^2)i_\perp(\theta)$ is substituted for $C_{sca}(\theta)$, leading to

$$\frac{2\dot{E}_\perp(\theta)\ln(I_0/I)}{E_0\delta\Omega\left[1-(I/I_0)^2\right]}=\frac{\lambda^2 i_\perp(\theta)ND}{4\pi^2}. \quad (A.9)$$

Again, the right-hand side is calculable from the Mie equations, the left is measured. Dividing by $\ln(I_0/I)=NC_{ext}D$ leads to the scatter–extinction ratio corrected for high turbidity,

$$\frac{2\dot{E}_\perp(\theta)(\text{measured})}{E_0\delta\Omega\left[1-(I/I_0)^2\right]}=\frac{\lambda^2 i_\perp(\theta)}{4\pi^2 C_{ext}}. \quad (A.10)$$

REFERENCES

Cannon, W. R., Danforth, S. C., Flint, J. H., Haggerty, J. S., and Marra, R. A. (1982a). *J. Am. Ceram. Soc.* 65(7):324–330.

Cannon, W. R., Danforth, S. C., Haggerty, J. S., and Marra, R. A. (1982b). *J. Am. Ceram. Soc.* 65(7):330–335.

Coltrin, M. E., Kee, R. J., and Miller, J. A. (1984). *J. Electrochem. Soc.* 131:425–434.

D'Alessio, A., Dilorenzo, A., Sarofim, A. F., Beretta, F., Masi, S., and Venitozzi, C. (1975). Fifteenth Symposium (International) on Combustion, p. 1427.

Dash, W. C., and Newman, R. (1955). *Phys. Rev.* 99:1151–1155.

Janai, M., and Karlson, B. (1979). *Solar Energy Mater.* 1:387–395.

Jones, A. R. (1979). *Prog. Energy Combust. Sci.* 5:73.

Kerker, M. (1969). *The Scattering of Light and Other Electromagnetic Radiation*, Academic, New York.

Koon Gee Neoh (1980). S. D. thesis, Department of Chemical Engineering, Massachusetts Institute of Technology, Cambridge, MA.

Kuhl, Ch., Schlotterer, H., and Schwidefsky, F. (1974). *J. Electrochem. Soc.: Solid-State Sci. Technol.* 121:1496–1500.

Lowes, T. M., and Newall, A. J. (1974). *Combust. Flame* 16:191–194.

Nishino, S., Matsunami, H., and Tanaka, T. (1975). *Jpn. J. Appl. Phys.* 14:1833–1834.

Rutgers, G. A. W., and DeVos, J. C. (1954). *Physica* 20:715–720.

Suyama, Y., Marra, R. A., Haggerty, J. S., and Bowen, H. K. (1985). *J. Am. Ceram. Soc.* 10:1356–1359.

Received 16 November 1984; accepted 28 January 1986

Reprinted from the Journal of the American Ceramic Society, Vol. 70, No. 1, January 1987
Copyright 1987 by The American Ceramic Society

Crystal Structure of Silicon Powders Produced from Laser-Heated Silane

ROBERT A. MARRA*,* AND JOHN S. HAGGERTY*

Department of Materials Science and Engineering, Massachusetts Institute of Technology, 12-009, Cambridge, Massachusetts 02139

The crystallinity and microstructure of fine silicon particles produced by the decomposition of laser-heated silane gas were studied in as-synthesized and annealed states. Amorphous, partially crystalline, and fully crystalline particles can be produced. With annealing at 550°C, partially crystalline particles become fully crystalline; amorphous particles remain amorphous. The results agree with previous interpretations of formation, growth, and crystallization processes in the reaction zone based on light scattering and transmission diagnostics.

THE laser-initiated gas-phase synthesis process is a very promising method for producing powders with the ideal characteristics required for technical ceramic applications. The process description[1] and the characteristics[2] of Si, SiC, and Si_3N_4 powders produced by this technique and the superior properties of resulting parts[3] have been discussed in previous publications. The present work examines the crystallinity and microstructure of fine silicon powders produced by pyrolysis of laser-heated silane gas. Depending upon the reaction conditions, the resulting particulate product can be amorphous, partially crystalline, or fully crystalline. Importantly, these results confirm critical aspects of previous, independent interpretations of particle formation and growth processes.

Detailed TEM characterization[4,5] of the Si powders shows that the primary Si particles agglomerate and ultimately fuse into larger particles as reaction temperatures approach and then exceed the melting point of Si. These agglomerates and fused particles form by processes that are distinct from the formation of the primary particles. This research addresses the latter and was initiated to corroborate interpretations[6] of formation and growth processes deduced from light scattering and transmission measurements.

EXPERIMENTAL PROCEDURE

Silicon powders were produced from laser-heated silane gas using the conditions summarized in Table I. The effects of the synthesis conditions (laser intensity, pressure, dilution with argon, and reactant flow rates) on the particle nucleation and growth kinetics and the resulting powder characteristics have been studied in detail.[7] The reaction zone temperatures were determined by micro optical-pyrometry corrected for nonunity emissivities. Emissivities of the reaction zone and particulate plume were measured[6,8] using the scattered and transmitted intensities of a HeNe laser beam. This scatter-extinction technique also yields the local particle number density and

CONTRIBUTING EDITOR — P. K. GALLAGHER

Received July 14, 1986; revised copy received August 29, 1986; approved September 18, 1986.
Supported by the Department of Defense under Contract No. N0014-77-C-0581.
*Member, the American Ceramic Society.
*Present address: Alcoa Technical Center, Alcoa Center, PA 15069.

Table I. Summary of Synthesis Conditions as Measured Particle and Crystallite Diameters for As-Synthesized and Annealed Si Powders*

Run designation	Laser intensity (W/cm²)	Maximum reaction temp (°C)	Measured diameter (nm)							
			As-synthesized				Annealed			
			Particle		Crystallite		Particle		Crystallite	
			BET	STEM	X-ray*	STEM	BET	STEM	X-ray*	STEM
658S‡	135	930	32.1	30	4.0	0	31.6	22	8.2	≈15
640S	175	960	35.2	30	6.2	≈10	34.4	30	11.4	10
638S	265	1020	38.0	NA	7.1	NA	38.7	NA	11.2	NA
648S	410	1120	68.9	NA	21.7	NA	65.1	NA	24.2	NA
646S	425	NA	75.5	NA	25.4	NA	80.9	NA	23.1	NA
635S	530	1190	93.2	≈85	33.8	≈30	88.9	≈80	30.3	≈40

*Assumes Gaussian peak shapes. ‡STEM analysis showed as-synthesized powder 658S to be completely amorphous and annealed powder to be <1% crystalline.

diameter, permitting nucleation and growth processes to be monitored within the reaction zone.

Numerous techniques were employed to determine the physical, chemical, and crystalline characteristics of as-synthesized and annealed powders. Particle densities were measured by He pycnometry. The surface area was measured by the BET method. The particle and crystalline sizes were measured using TEM, STEM, and X-ray line broadening. The broadening of a single X-ray diffraction peak was used to determine the crystalline size presuming both Gaussian and Cauchy shaped peaks;[9] lattice distortions and stacking faults had negligible effects[7] on the peaks.

Powders synthesized with varied laser intensities were annealed to elucidate the crystalline microstructures of the as-synthesized powders. The powders were annealed for 6 h at 550°C in argon. At this temperature, there should be no homogeneous nucleation of crystalline material within the amorphous regions but existing crystallites should grow rapidly into amorphous regions.[10,11] Also, both normal and secondary grain growth rates are negligible at this temperature.[12-14]

Results

In general, the silicon powders were all similar in character. The primary particles were fine (average particle sizes from 20 to 95 nm), were nearly monodispersed, were pure (spectrographically ≤200 ppm total impurities and ≤0.1 wt% O_2), and were spherically shaped. The physical and crystalline characteristics are summarized in Table I. For the Si powders used in these studies, the BET equivalent spherical diameters and the diameters measured from TEM micrographs were always nearly equal, indicating that the particles had both no porosity accessible to the surfaces and smooth surfaces. Powder densities determined from helium pycnometry indicated the particles had no appreciable closed porosity. Most Si powders were at least partially crystalline to both X-ray and electron diffraction. In all cases, the crystallite sizes were substantially smaller than both the BET equivalent and the (S)TEM particle diameters; each individual particle contained numerous crystallites.

It was found that the ratio of the crystallite size, determined from X-ray line broadening, to the overall particle size, determined by BET surface area measurements, varied systematically with synthesis conditions. Figure 1 shows the effect that laser intensity, and the dependent maximum reaction zone temperature, had on the ratio of the crystallite diameter, $d_{X\text{-ray}}$, to the particle diameter, d_{BET}, in the as-synthesized powders. The relative crystallite size initially becomes larger with increasing reaction zone temperature. Above a specific reaction zone temperature (≈1080°C), the $d_{X\text{-ray}}/d_{BET}$ ratio remains constant. Similar results[8] were observed with temperature changes induced by varied reactant gas flow rates and dilution of the reactant gas stream with argon.

If the as-synthesized powders with the relatively small crystallite sizes were fully crystalline, the low-temperature annealing treatment should have little effect on either the crystallite or particle sizes because both growth rates are negligible until temperatures approach the melting point,[12-14] even in heavily doped powders. If the powders were partially crystalline, the annealing cycle should cause the crystallite size to increase while the overall particle size should remain unchanged because the transformation (growth) rate is appreciable at 550°C.[10,11] The annealing results are summarized in Table I and presented graphically in Fig. 1. As anticipated, this low-temperature anneal caused no observable effect on the size or shape of the particles. However, annealing did alter their microstructures in some cases.

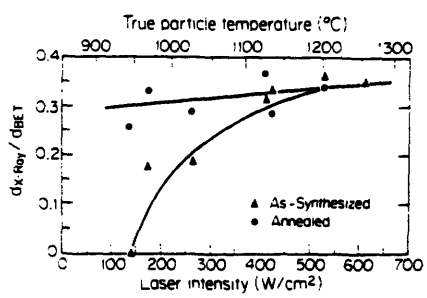

Fig. 1. Effect of laser intensity and a 550°C, 6-h postsynthesis annealing treatment on the crystallite-to-particle size ratio of laser-synthesized Si powders. The correlation between the maximum true reaction zone temperature experienced by the particles and the laser intensity is shown.

For the lowest intensity run, 658S (T_{max}=930°C), the as-synthesized powder appeared completely amorphous by STEM analysis. X-ray diffraction peaks were extremely weak with breadths corresponding to crystallite sizes of nominally 4.0 nm. Since this dimension is much larger than the STEM resolution limit (≈1.5 nm),[15] we presume that a very few crystalline particles exist in this as-synthesized powder. The annealed 658S powder remained almost completely amorphous, confirming that a 550°C annealing temperature does not permit appreciable nucleation. After annealing, STEM analysis indicated that a very small number (<1%) of particles contained crystalline regions that were surrounded by still amorphous material. It is unlikely that these 8- to 15-nm crystallites existed in the as-synthesized powder; rather, they grew either from preexisting microcrystallites that were too small to be imaged by STEM or from a very small number of nuclei formed and propagated during this annealing process.

The individual as-synthesized particles from the intermediate intensity run 640S (T_{max}=960°C) contained both amorphous and crystalline regions. No amorphous areas remained in any of the annealed particles. Dark-field images of the as-synthesized and annealed powders showed that annealing caused both the fraction of crystalline material and the crystallite size to increase.

Powder 635S made at the highest intensity (T_{max}=1190°C) was entirely crystalline in both the as-synthesized and annealed states. Their grain sizes were typically a large fraction (⅓ to ½) of their particle sizes.

The STEM, X-ray line broadening, and BET surface area results corroborate one another. The 550°C anneal had no appreciable effect on particle size. At sufficiently low synthesis temperatures, the as-synthesized powders were amorphous; annealing at 550°C for 6 h did not cause appreciable crystallization. With somewhat higher synthesis temperatures, the as-synthesized particles contained both amorphous and crystalline regions. With annealing, the crystallites in these powders

grew into the surrounding, initially amorphous regions producing fully crystalline particles. With still higher synthesis temperatures, the as-synthesized powder was fully crystalline and the low-temperature anneal had negligible effect on the microstructure.

The total number of nuclei that ultimately form and propagate to the point of impingement are approximately the same ($\approx 3^3 = 27$) in each particle for all powder types. This same result has been observed by Phillips[16] for SiC powders made with plasma-heated gaseous materials.

Discussion

The formation of initially amorphous solid nuclei directly from the vapor phase, subsequent growth by accretion of vapor molecules, and possible crystallization of the amorphous particles in the hotter regions of the reaction zone were postulated independently on the basis of the light scatter-extinction results.[6] If reaction temperatures remained below the spontaneous crystallization temperature of amorphous silicon, the particles remained amorphous. In numerical agreement with measured diameters and mass flow rates, the number density of particles calculated by the scatter-extinction technique remained essentially constant if the particles were assumed to have refractive indices characteristic of amorphous silicon at the base of the reaction zone and refractive indices of either polycrystalline or a mixture of polycrystalline and amorphous silicon at positions further into the reaction zone where temperatures were higher. The majority of particle growth occurred under conditions where a constant particle number density was observed.[6,7] The accuracy of this description depends largely on the presumed crystallization of initially amorphous particles being correct.

These annealing studies showed that the crystallization process is inhibited by the absence of nuclei within particles that have not been exposed to synthesis temperatures in excess of nominally 930°C, a temperature level which exceeds spontaneous crystallization temperatures normally observed[11] for amorphous Si films. The difference between the temperature levels probably results primarily from the extremely short exposure time ($\approx 10^{-3}$ s) in the laser synthesis process; however, other factors may be important because nucleation and growth rates of crystalline Si are extremely sensitive[11] to the composition and microstructure of the amorphous matrix. Once reaction temperature levels are reached (>930°C) where nuclei form in the initially amorphous particles, the crystallites grow until they impinge and the particles become fully crystalline. Although this temperature level is higher than both normal spontaneous crystallization temperatures and the annealing temperature used in these experiments, growth of Si crystallites into amorphous material without simultaneous homogeneous nucleation has been observed[17,18] in amorphous Si films.

The crystallite growth rates within these Si powders can be deduced qualitatively. During particle growth, the crystallites grew to a diameter of 6 to 10 nm in $\leq 10^{-3}$ s at $T \leq 960$°C corresponding to a minimum radial growth rate of 3×10^3 nm/s. During annealing at 550°C, growth rates were at least 9×10^{-5} nm/s. These compare with reported rates[11,19,20] of 8×10^{-4} to 2 nm/s at 550°C and estimated rates of 8×10^3 to 8×10^5 nm/s at 960°C based on extrapolations of rates measured in films at temperatures up to 650°C. The crystallite growth rates observed in these powders appear reasonable based on the ranges of reported rates.

The persistent constancy of the number of nuclei that form within otherwise highly variable particles remains puzzling; nucleation usually occurs either heterogeneously at free-particle surfaces, heterogeneously on contained impurity inclusions, or homogeneously within the volumes leading to $\approx d^2$ or $\approx d^3$ rate dependencies that increase exponentially with temperature. The observed result would follow if nucleation occurred (probably heterogeneously) only over a narrow range of particle diameters and temperatures during growth for all synthesis conditions because final particle diameters range over a factor of ≈ 3. Although the occurrence of similar time-temperature-diameter histories might be argued for specific portions of all synthesis experiments, nucleation would have to cease abruptly in all cases even with a continually rising temperature since these synthesis experiments did not have the same maximum temperatures. This postulated behavior is inconsistent with this study's findings; nucleation in the amorphous regions of the particles was shown to be kinetically inhibited at lower temperatures hence normally would be expected to increase exponentially in rate with increasing temperature rather than ceasing abruptly. Another possible explanation for this study's findings could be rapid epitaxial growth of grains from a fixed number of nuclei during deposition causing an absence of amorphous material in which homogeneous nuclei could form. This postulate is also contradicted by the study's results; the particles grow faster ($\approx 10^5$ nm/s) than the crystallites, thereby producing partially crystalline particles. To summarize, for unexplained reasons, nuclei do not form homogeneously within the primary particles under conditions for which they are expected based on other studies.[17-20]

These results reflect on the particles' formation and growth history from SiH_4 gas. They are consistent with the sustained growth of amorphous material onto initially amorphous nuclei by the accretion of vapor molecules during the initial stages of growth of the primary Si particles. The emergence of a fixed number of nuclei per particle and the apparent cessation of nucleation with rising temperature are the two important anomalies revealed by these results.

Acknowledgment

The authors gratefully acknowledge Dr. Tom Kelly of MIT for his assistance with the STEM characterization.

References

[1] W. R. Cannon, S. C. Danforth, J. H. Flint, J. S. Haggerty, and R. A. Marra, "Sinterable Ceramic Powders from Laser-Driven Reactions: I, Process Description and Modeling," *J. Am. Ceram. Soc.*, **65** [7] 324–30 (1982).

[2] W. R. Cannon, S. C. Danforth, J. S. Haggerty, and R. A. Marra, "Sinterable Ceramic Powders from Laser-Driven Reactions: II, Powder Characteristics and Process Variables," *J. Am. Ceram. Soc.*, **65** [7] 331–35 (1982).

[3] J. S. Haggerty, J. H. Flint, G. J. Garvey, J.-M. Lihrmann, and J. E. Ritter, "High Strength, Oxidation Resistant Reaction-Bonded Silicon Nitride from Laser-Synthesized Silicon Powder"; in Proceedings of the 2nd International Symposium, Ceramic Materials and Components for Engines, Lübeck-Travenmunde, Federal Republic of Germany, April 1986.

[4] J. S. Haggerty, "Sinterable Ceramic Powders from Laser-Heated Gas-Phase Reactions and Rapidly Solidified Ceramic Materials," July 1984, Chapter V, pp. 75–106, under Contract N00014–82–K–0350, MIT, Cambridge, MA.

[5] K. Sawano, "Formation of Silicon Carbide Powder from Laser-Induced Vapor-Phase Reactions"; Ph.D. Thesis, Department of Materials Science and Engineering, MIT, Cambridge, MA, 1985.

[6] J. H. Flint, "Powder Temperatures in Laser-Driven Reactions"; S.M. Thesis, Department of Materials Science and Engineering, MIT, Cambridge, MA, 1982.

[7] R. A. Marra, "Homogeneous Nucleation and Growth of Silicon Powder from Laser-Heated Gas-Phase Reaction"; Ph.D. Thesis, Department of Materials Science and Engineering, MIT, Cambridge, MA, 1983.

[8] J. H. Flint, R. A. Marra, and J. S. Haggerty, "Powder Temperature, Size, and Number Density in Laser-Driven Reactions," *Aerosol Sci. Technol.*, **5** [2] 249–60 (1986).

[9] B. B. Cullity, Elements of X-Ray Diffraction, Addison-Wesley, Reading, MA, 1959.

[10] K. Zellama *et al.*, "Crystallization in Amorphous Silicon," *J. Appl. Phys.*, **50**, 6995–7000 (1979).

[11] F. D. Van Gieson, "Kinetics of Crystallization of Selected Amorphous Silicon Films"; S.M. Thesis, Department of Materials Science and Engineering, MIT, Cambridge, MA, 1982.

[12] L. Mei, M. Rivier, Y. Kwark, and R. W. Dutton, "Grain-Growth Mechanisms in Polysilicon," *J. Electrochem. Soc.*, **129** [8] 1791–95 (1982).

[13] Y. Wada and S. Nishimatsu, "Grain Growth Mechanism of Heavily Phosphorus-Implanted Polycrystalline Silicon," *J. Electrochem. Soc.*, **125** [9] 1499–504 (1978).

[14] C. V. Thompson and H. I. Smith, "Surface-Energy-Driven Secondary Grain Growth in Ultra Thin (<100 nm) Films of Silicon," *Appl. Phys. Lett.*, **44** [6] 603–605 (1984).

[15] J. B. Vandersande, MIT, Cambridge, MA; private communication.

[16] D. S. Phillips, Los Alamos National Laboratory, NM; private communication.

[17] A. M. Glaeser, J. S. Haggerty, and S. C. Danforth, "Polycrystalline Semiconductor Processing," U.S. Pat. No. 4 379 020, April 5, 1983.

[18] S. C. Danforth, F. Van Gieson, J. S. Haggerty, and I. Kohatsu, "Laser-Induced Controlled Nucleation and Growth Process for Large Grained Polycrystalline Silicon"; pp. 443–48 in Materials Research Society Symposia Proceedings, Vol. 1, Laser and Electron-Beam Solid Interactions and Materials Processing. Edited by J. F. Gibbons, L. D. Hess, and T. W. Sigmon. North-Holland, New York, 1981.

[19] E. F. Kennedy, L. Csepregi, J. M. Mayer, and T. W. Sigmon, "Influence of ^{16}O, ^{12}C, ^{14}N, and Noble Gases on the Crystallization of Amorphous Si," *J. Appl. Phys.*, **48** [10] 4241 (1977).

[20] L. Csepregi, E. F. Kennedy, T. J. Gallagher, J. W. Mayer, and T. W. Sigmon, "Reordering of Amorphous Layers of Si Implanted with ^{31}P, ^{75}As, ^{11}B, Ions," *J. Appl. Phys.*, **48** [10] 4234 (1977). □

Wetting and Dispersion of Silicon Powder Without Deflocculants

SUSUMA MIZUTA, W. ROGER CANNON, ALAN BLEIER, and JOHN S. HAGGERTY

Dept. of Materials Science and Engineering, Massachusetts Institute of Technology, Cambridge, MA 02139

The dispersion characteristics of fine, pure silicon powders in a number of liquids were studied under controlled atmospheric conditions. A simple screening test was used to judge the dispersion characteristics qualitatively. Sessile drops were examined to determine whether or not the contact angles measured on single crystalline silicon correlated with the dispersion behavior. The stability of powder suspensions depended on the dielectric constant of the liquid. Agglomerates within the suspensions were examined by several direct techniques. Also, powder was centrifugally cast from one of the suspensions permitting the degree of uniformity in green parts to be used as a qualitative measure of dispersion quality.

Early studies on the dispersibility of silicon were conducted near the beginning of this century. Weiser[1] cites Kuzal as first preparing hydrosols of thoroughly pulverized silicon by treating the powder alternately with acid and alkali; while Wegelin[2] also prepared silicon hydrosols by mechanical grinding. Astalk and Gutbier[3] investigated the chemical preparation of colloidal silicon by reduction of silicon dioxide with magnesium. By processes which involved grinding and washing silicon with hydrochloric acid, they produced both unstable and concentrated sols.

Recent interest[4] in silicon dispersions has focused on aqueous slips for casting parts to be subsequently nitrided to reaction-bonded silicon nitride. This study is directed toward forming reaction-bonded silicon nitride parts with a very fine, highly pure silicon powder synthesized by a laser gas-phase process.[4] Initial experiments showed that aqueous media introduce uncertainties about oxidation which adversely affect the nitriding process. We have, therefore, chosen to study dispersions of silicon in various organic solvents, some of which sufficiently volatile that they are eliminated easily during drying. The work reported here concentrates on organic dispersions in the absence of surfactants or polymer deflocculants, since these additives are often difficult to eliminate from a green part.

According to Williams and Goodman,[5] a single crystalline silicon wafer is oxidized immediately when exposed to air, producing a layer of SiO_2 which in turn controls the wetting characteristics of the wafer. Apparently, previous investigations[1-3] on silicon dispersions were conducted in aqueous media without controlling the atmosphere (air), resulting in ambiguous results, especially in view of Williams and Goodman's comments. Special care was taken to control the processing atmosphere in our experiments to avoid this problem.

This study uses a fine, monosized, highly pure silicon as the starting powder, prepared according to Haggerty and Cannon[4] and addresses (1) the basic wetting properties of this new silicon powder using representative families of organic liquids and (2) the dispersion properties of this powder, including states of agglomeration.

Experimental

Materials

The silicon powder used in this study was synthesized from the laser-driven decomposition of $SiH_4(g)$ under the following conditions: 760 $W \cdot cm^{-2}$ CO_2 laser intensity, 2×10^4 Pa (0.2 atm) cell pressure, 11 cm^3 SiH_4 min^{-1}, and 1000 cm^3 Ar min^{-1}.[4] The surface area from single-point BET measurements is 55.4 $m^2 \cdot g^{-1}$, corresponding to an equivalent spherical diameter of 46.5 nm. Neutron activation analysis indicated 0.14 wt% oxygen and spectroscopic analysis indicated <30 ppm of other elements.

Commercially available grades of the organic liquids were used in this study; selected physical properties[7,8] are given in Table I. These liquids represent commonly available organic families, including aliphatic and aromatic hydrocarbon, alcohol, ketone, ether, carboxylic acid, and aldehyde classes; water is also included.

The single-crystalline silicon wafer used for contact angle measurements was boron-doped (10^{17} cm^{-3}). The wafer was cleaned to remove oxidic layers which may have been present in the "as-received" material. This was accomplished by ultrasonic agitation in trichloroethylene, acetone, methanol, and pure water for 5 min in each. The silicon wafer was then treated with 2.9*M* HF for an additional 5 min. With the aid of a nitrogen purge, the HF solution was removed by successively diluting the cleaning liquor with pure water. The silicon wafer was dried and placed into a sealed plastic chamber equipped with an optical glass window and a rubber cover under glove box conditions. This arrangement permitted contact angles to be measured under $N_2(g)$ atmosphere, containing less than 1 ppm oxygen and water.

Dispersion Test

A simple screening test was used to determine the wetting behavior and stability of suspensions consisting of the silicon powder and the various liquids. Preparation of a system was conducted by introducing a small amount of powder (100 mg) into a glass bottle under nitrogen atmosphere in a glove box and then sealing it with a thin rubber cover. After the selected liquid (15 cm^3) was injected through the rubber cover into the bottle via a syringe, the powder was dispersed by first shaking the mixture lightly and, subsequently, subjecting the systems to an ultrasonic probe for three minutes to mix thoroughly. After standing for 5 days, the suspensions were visually evaluated.

Contact Angle Measurement

The equilibrium contact angle (θ_e) established with sessile drops (0.01 cm^3) of desired liquids on single crystalline silicon was measured at 23°C with a contact angle goniometer.*

Detailed Agglomeration Evaluation for n-Propanol Systems

Dispersion Preparation: The state of agglomeration was evaluated in systems of silicon dispersed in *n*-propanol via three preparative methods.

a.) Hand Mixing: A small amount of silicon powder (~1 mg) and *n*-propanol (10 cm^3) were mixed under a controlled $N_2(g)$

*Member, the American Ceramic Society.
*Model A-100, Rame-Hart, Inc., Mountain Lakes, NJ.
†Model W255R, Heat Systems-Ultrasonic, Inc., Plainview, NY.
‡Coulter Electronics, Inc., Nanosizer, Hialeah, FL.
§Brice Phoenix, Inc., Virtus Co., Cardiner, NY.

Presented at the 83rd Annual Meeting of the American Ceramic Society, Washington, DC, May 5, 1981 (No. 73-B-81).
Received August 3, 1981; revised copy received March 4, 1982; approved March 10, 1982.

Table I. Physical Properties of Liquids*

Liquid	Grade	Dielectric constant[7]	Surface tension[2] (mN·m⁻¹)	Dispersion test results*	Angle (degrees)
		Aliphatic hydrocarbons			
n-hexane	Certified[§]	1.89	18.4	Poor	0
Cyclohexane	Analytical[‖]	2.02	25.2	Poor	‖‖
n-octane	**	1.95	21.6	Poor	0
		Benzene group			
Benzene	Analytical	2.28	28.9	Poor	0
Toluene	Reagent**	2.4	28.5	Poor	0
Xylene	Certified[§]	2.3-2.5	28-30	Poor	‖‖
		Alcohols			
Methanol	Absolute[‡‡]	32.6	22.5	Good	0
Ethanol	Absolute[‡‡]	24.3	22.4	Good	‖‖
n-Propanol	Analytical[‖]	20.1	23.7	Good	0
Isopropanol	Certified[§]	18.3	21.3	Good	‖‖
n-butanol	Reagent[‡‡]	17.8	25.4	Good	‖‖
n-heptanol	‡‡			Good	‖‖
n-octanol	Certified[§]	10.3	27.5	Good	0
Benzyl alcohol	Analytical[‖]	13.1	35.5	Good	14
Ethylene glycol	Certified[§]	38.7	48.4	Good	45
		Ketones			
Acetone	Analytical[‖]	20.7	25.1	Good	0
2-pentanone	**	15.4	23.6	Good	0
2-heptanone	Technical[§§]	9.8	26.7	Good	0
		Ether			
Isopentyl ether	**	2.82	22.9	Poor	§§
		Aliphatic acids			
Propionic acid	Certified[§]	3.30	26.7	Poor	0
Butyric acid		2.97	26.5	Poor	‖‖
		Aldehyde			
Benzaldehyde	Reagent**	17.8	38.5	Good	6
		Inorganic			
Water	Distilled	78.5	72.75	Flotation	78

*17°–25°C. [7]Ref. 6. [2]Ref. 7. [§]Fisher Scientific Co., Pittsburgh, PA. [‖]Mallinckrodt Inc., St. Louis, MO. **J. T. Baker Chemical Co., Phillipsburg, NJ. [‡‡]U. S. Industries, Inc., New York, NY. [‡‡]Eastman Kodak Co., Rochester, NY. [§§]Aldrich Chemical Co., Inc., Milwaukee, WI. [‖‖]Not Measured.

atmosphere. The mixture was shaken lightly by hand and diluted to convenient concentrations for particle size measurements.

b.) Ultrasonic Agitation: By subjecting the powder suspension to an ultrasonic probe, agglomerates were broken down, allowing the powder to be fully wetted and dispersed in the liquid. Powder was mixed with *n*-propanol in the manner just described. The suspension (25 cm^3) was subsequently subjected to an ultrasonic probe[*] equipped with a 1.27-cm diameter disruptor horn for ~3 min; input power was 150 watts. The suspension was cooled with an *n*-propanol/dry ice mixture while being agitated.

c.) Centrifugation: After mixing silicon powder (0.5 g) and *n*-propanol (15 cm^3), the suspension was subjected to the ultrasonic probe for 3 min. Samples were centrifuged at 12 000 rpm for 10 min to remove large agglomerates, which comprised approximately one half the mass of the initial powder. After this treatment, the equivalent spherical diameter of the largest agglomerates remaining in suspension is 260 nm based on Stokes' settling velocity. This supernatant was recentrifuged at 17 000 rpm for 2 h. The supernatant of the second centrifugation contained very little powder, yet enough remained suspended to impart a tan color to the supernatant.

Analysis Techniques

The state of agglomeration of silicon powder in *n*-propanol was determined using three analytical techniques.

a.) TEM: Specimens were prepared by dipping carbon-deposited TEM grids in suspensions of approximately 1×10^{-4} mol Si/L. Excess suspension was removed by drawing liquid off with the edge of an absorbent paper. Since agglomerates were found to be separated on the grid by several hundred diameters, agglomeration during drying is not deemed important.

b.) Laser-Doppler Particle Size Analysis[7]: This technique yields the equivalent particle diameter owing to Brownian motion. The width of the size distribution is indicated qualitatively by the dispersion factor: ranging on a scale from 1 to 10 for narrow and wide distributions, respectively.

c.) Light Scattering: Dissymmetry measurements were taken with a universal light-scattering photometer[§] at a wavelength $\lambda_0=546$ nm to estimate the agglomerate size.[10] Accurate values can be obtained only for dissymmetry values less than ~2.0, corresponding to an average size of ~200 nm; thus, the technique was useful only for the smallest agglomerates described in the next section. The intensity of light scattered by suspensions containing agglomerates whose sizes were approximately $0.1\lambda_0$ (i.e., ~55 nm) exhibited a distinct angular dependence typical of Rayleigh scattering.

Results and Discussion

Dispersion Test

Three types of dispersion behavior were observed and are summarized in the fifth column of Table I and in Fig. 1.

1) Good Dispersion: Most of the particles were well dispersed, even after several days. This phenomenon was observed for liquids such as aliphatic alcohols, ketones, benzyl alcohol, and benzaldehyde. Each solvent in this group has a high dielectric constant.

2) Poor Dispersion: Most of the particles settled out of the suspension within one hour after preparation. This phenomenon was observed for liquids such as *n*-hexane, cyclohexane, *n*-octane, benzene, toluene, xylene, isopentyl ether, and propionic and butyric acids, each of which has a low dielectric constant.

3) Particle Flotation: All silicon powder remained on the liquid surface and particles could not be incorporated into the liquid, even after vigorous agitation. This phenomenon was observed only for water. Interestingly, in a separate experiment in which the powder was exposed to air for several hours prior to mixing with liquid, it was easily wetted by water.

Although the tests suggest that each of the liquids designated as giving good dispersion in Table I and Fig. 1 should prove adequate

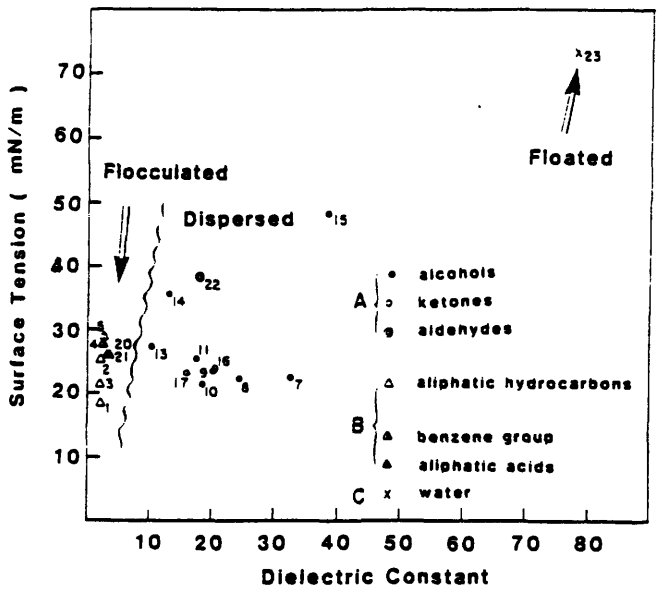

Fig. 1. Relation between dispersibility of Si powder and surface tension and dielectric constant of liquid. Solvents in group A gave good dispersion, those in group B poor dispersion and settling, and that in group C flotation.

for casting silicon powder, some appear to be realistically less desirable than others. Methanol and acetone are quite volatile, whereas butanol, heptanol, octanol, benzyl alcohol, and ethylene glycol may be difficult to remove from the powder due to their high viscosities. Benzaldehyde, on the other hand, is chemically unstable.[7] Thus, *n*-propanol was chosen for subsequent experiments since it has generally acceptable physical properties and represents the remaining candidate liquids which gave good dispersions.

Contact Angle Measurements

Measured contact angles are also given in Table I. Zero-degree contact angles were found for liquids with surface tensions less than 30 $mN \cdot m^{-1}$, while nonzero values were measured for higher surface tension liquids such as benzyl alcohol, ethylene glycol, benzaldehyde, and water.

The contact angle reported here for water on silicon (78°) is less than those measured by Williams and Goodman[5] (85-88°) using the bubble method for pure water and an HF solution. Although the most likely cause for the discrepancy is a difference in purity, the smaller contact angle in our study may result from the drop-size effect discussed recently by Neumann and Good[9] which is due ultimately to surface heterogeneity or roughness. Another explanation for the discrepancy in θ_e can be understood by considering minute levels of oxidation. Using the contact angles and oxide thicknesses reported by Williams and Goodman,[5] our value of 78° suggests the existence of an oxide layer ~0.25 nm thick. Although the atmosphere in our experiments is controlled to less than 1 ppm oxygen, such an oxidic monolayer is possible.

The correlation between measured contact angles and reported surface tensions (γ_{LV}) follow from

$$\cos\theta_e = (\gamma_{SV} - \gamma_{SL})/\gamma_{LV}$$

for which γ_{SL}, γ_{SV}, and γ_{LV} refer to the excess energies of the solid-liquid, solid-vapor, and liquid-vapor interfacial regions. Since the term ($\gamma_{SV} - \gamma_{SL}$) is essentially the same for most of the organic liquids studied[11] and in view of the nonpolar character of silicon, a 0° contact angle for essentially nonpolar liquids such as hydrocarbons, aliphatic alcohols, ketones, and propionic acid is anticipated, whereas for water, a highly polar solvent, nonwetting behavior toward Si-powder is not surprising.

Agglomeration Evaluation

Table II contains results of size analyses for Si-agglomerates suspended in *n*-propanol. Of the three preparative techniques used, only centrifugal separation was capable of producing suspensions which were essentially free of agglomerates. The ultimate particle size range, 50 to 55 nm, is confirmed by the three techniques and agrees well with the equivalent spherical diameter determined using BET gas adsorption.

The particles in *n*-propanol suspensions which were prepared by hand mixing or with ultrasonic agitation retain the chain-like structures characteristic of the "as-synthesized" powders.[4] Apparently, these particulate structures comprise the agglomerates because data in Table II from Laser-Doppler analysis agree approximately with those from TEM analysis. The most important result is that interparticle bonds within chain-like structures can be broken using *n*-propanol as a dispersing medium. The data indicate that the agglomerates are reduced in size when suspensions are subjected to the ultrasonic probe and that the first centrifugal separation leaves a large fraction of the mass suspended as single particles or small agglomerates containing fewer than four or five primary particles.

Fracture surfaces of pellets cast from an *n*-propanol suspension during the second centrifugal separation process described earlier were examined as a qualitative measure of the dispersion (Fig. 2). Uniform, defect-free castings were taken as an indication that the powders were dispersed well and were largely free of agglomerates. The almost cleavage-like fracture surfaces were flatter than observed for dry-pressed pellets,[4] suggesting a greater uniformity in the former. The cast pellet did not exhibit 'relic' structures attributable to agglomerates. Void diameters were on the order of a particle size. In contrast, the pressed pieces[4] exhibit 2- to 5-μm voids which probably result from agglomerates. This result indicates further that agglomerates were removed centrifugally prior to casting since corresponding voids are not observed in the cast pellet. The green density was typically in the range 45–50% of the theoretical value. Cast pellets did not exhibit long range microstructural features, for example, those which typically result from stratification occurring during settling. The results of these preliminary casting experiments also indicate that this silicon powder can be dispersed well.

Conclusions and Summary

The results of the dispersion tests, summarized in Fig. 1, emphasize the effects of surface tension and dielectric constant. Based on the contact angles and this surface tension-vs-dielectric constant profile, wetting and dispersion properties of silicon are as follows:

a.) Liquids having high surface tensions, >30 $mN \cdot m^{-1}$, exhibit nonzero contact angles. Examples are benzaldehyde, ethylene glycol, and benzyl alcohol. Although powder was incorporated into these three liquids which belong to Group A (Fig. 1), it seems that the agglomerates are either partially wetted by these solvents and

Table II. Results of Size Analyses for *n*-Propanol Suspensions

Preparative method*	Light scattering analysis: Dissymmetry factor, Z	Light scattering analysis: Diameter (nm)	TEM: Min. size (nm)	TEM: Max. size (nm)	Laser-Doppler analysis: Diameter (nm)	Laser-Doppler analysis: Dispersion factor
Hand mixing	2.5		440	620	800	8
Ultrasonic agitation	2.7		200	420	200	4
Centrifugation†	1.1	50	50	55	50	3

*See text for details. †Supernatant from second centrifugation.

Fig. 2. Scanning electron micrograph of cast green Si compact (bar=1 μm).

that other factors such as van der Waals dispersion forces are insufficient to induce agglomeration. The effects of the latter are discussed in detail elsewhere[11]; nevertheless, these solvents seem unfavorable as "best" dispersing media for silicon powder.

b.) Powders could not be dispersed well in liquids having a dielectric constant less than ~5. Examples are aliphatic hydrocarbons, members of the benzene group, isopentyl ether, and acids. This phenomenon appears to be independent of surface tension and the behavior is in accord with the concept that the powder's tendency to remain agglomerated is directly related to the silicon-solvent interfacial free energy and is not strongly dependent on the liquid's surface tension. Particulate cohesion, rather than complete wetting and dispersion, occurs in these liquids. This can be understood in terms of the low dielectric constant and the nonpolar nature of these liquids.[11] It is anticipated that silicon-solvent interactions are weak for liquids with very low dielectric constants. These interactions should increase with increased polarity or dielectric constant. This trend was observed: see the next section and Ref. 11 for details.

c.) Liquids having high dielectric constants seem ideal dispersing media. However, the liquid surface tension should be low enough to ensure that the powder agglomerates are immersed in the liquid and that the liquid fully penetrates the agglomerates and breaks them down.

In summary, by using a simple dispersion test and by controlling the atmospheric composition, it was found that all classes of organic liquids which were tested incorporate this Si powder and that water does not. Although the organic liquids incorporate the powder, three of them (viz., benzyl alcohol, ethylene glycol, and benzaldehyde) exhibited a nonzero degree contact angle on a single crystalline Si-wafer. Thus, it appears that, while a 0° contact angle is not necessary to incorporate the powder into a given liquid, a low θ_c-value is desirable. Since the stability of these suspensions relates to the solvent's dielectric constant and polar nature, liquids which have a high dielectric constant formed the most stable suspensions. It is noteworthy that for both good and poor dispersants (Table I), the dispersibility of Si powder was not sensitive to the solvent's chemical nature, e.g., acids vs alcohols, except as generally reflected by the dielectric constant. Data in Table II demonstrate that even suspensions prepared with a good dispersing medium contain agglomerates that could be broken down by ultrasonic agitation or removed by centrifugation.

Susuma Mizuta is a research associate in the Energy Chemistry Div. of the National Chemical Lab for Industry, Yatabe, Ibaraki, Japan. When this work was done, he was a postdoctoral research associate at Massachusetts Institute of Technology. A graduate of Tokyo University, he holds a B.S. and a Ph.D. in industrial chemistry.

John S. Haggerty

W. Roger Cannon is associate professor, Dept. of Ceramics, Rutgers University. Before joining the Rutgers faculty in 1981, he was a member of the research staff at MIT, participating for four years in the Ceramics Processing Lab. He earned his B.S. from the University of Utah, and both his M.S. and Ph.D. from Stanford University.

Alan Bleier is Corning assistant professor of ceramics, Dept. of Materials Science and Engineering at MIT. He received three degrees from Clarkson College of Technology: a B.S. in chemistry in 1970, and an M.S. in 1973 and a Ph.D. in 1976, both in physical chemistry. Dr. Bleier was with Union Carbide Corp. before joining MIT in 1980.

John S. Haggerty is a senior research scientist at MIT; he holds a joint appointment with the Energy Lab and the Dept. of Materials Science and Engineering. Dr. Haggerty graduated from MIT with a B.S. in mechanical engineering in 1961, an M.S. in ceramics in 1963, and a Ph.D. in ceramics in 1965. From 1964 to 1977 he was with Arthur D. Little Inc.

Acknowledgment

We acknowledge the support of both Standard Oil of Indiana and the Defense Advanced Research Projects Agency.

References

[1]H. B. Weiser, "Inorganic Colloid Chemistry," in The Colloidal Elements, pp. 14–16, 163, Vol. 1, Wiley and Sons, New York, 1933.

[2]G. Weglin, "Production of Colloidal Suspensions through Mechanical Combination," *Kolloid-Z.*, 14 [2] 65–69 (1914).

[3]R. Astfalk and A. Gutbier, "A Report on Mechanical Mixing and Dispersion of Colloidal Silicon," *Kolloid-Z.*, 15 [1] 23–27 (1914).

[4]J. S. Haggerty and W. R. Cannon, "Sinterable Powders from Laser Driven Reactions," Annual Report on Contract No. N00014–77–C–0581, M.I.T. Report No. MIT EL 79-047, (1980).

[5]R. Williams and A. M. Goodman, "Wetting of Thin Layers of SiO_2 by Water," *Appl. Phys. Lett.*, 25 [10] 351–32 (1974).

[6]Handbook of Chemistry and Physics, 55th Ed., Chemical Rubber Co., 1974.

[7]J. J. Jasper, "The Surface Tension of Pure Liquid Compounds," Reprint J. Phys. Chem. Ref. Data 1 [4] 841–1010 (1972).

[8]A. W. Neumann and R. J. Good, Surface and Colloid Science, pp. 31–91, Vol. 11, Plenum Press, New York, 1979.

[9]M. Kerker, The Scattering of Light and Other Electromagnetic Radiation, Chapter 1, Academic Press, 1969.

[10]A. Peterlin, "Determination of Molecular Dimensions from Light Scattering Data," *Progress in Biophysics*, 9, 175–237 (1959).

[11]A. Bleier, "Role of van der Waals Forces in Determining the Wetting and Dispersion Properties of Silicon Powder," unpublished paper.

Submitted to Journal of
Am. Cer. Soc. J87-15

Dispersion of SiC Powders in Non-aqueous Solvents

by

M. Okuyama[1], G. Garvey[2], T. A. Ring[3] and J. S. Haggerty

Massachusetts Institute of Technology
77 Massachusetts Avenue
Cambridge, Massachusetts 02139

ABSTRACT

Thirty-two pure solvents were used to disperse laser-synthesized SiC powder, oxidized laser-synthesized SiC powder, and commercially available SiC powder. Five day sedimentation tests were used to screen the solvents with relative turbidity of the supernatant as a quantitative measure if the degree of dispersion. Coagulation kinetics were measured by Photon Correlation Spectroscopy to determine the coagulation rate. Stabilized powders were centrifugally cast into ceramic green bodies and their green densities measured. Experimental dispersion results were correlated with various solvent properties including dielectric constant, hydrogen bond index, pH_a and Lewis acid/base interaction energy. To determine the Lewis interaction energy parameters for the powder surfaces, microcalorimetry was used to measure the heat of wetting of the powders in various acidic and basic solvents.

Oxidized SiC powder, either laser or commercial, was shown to have an acidic surface and was stabilized by basic solvents. Pure laser-synthesized SiC powder was shown to have a basic surface and was stabilized by acidic solvents. Solvents with high hydrogen bond indices also gave high packing densities. Other solvent properties had a much smaller influence on powder dispersibility. Good dispersibility gave ceramic green bodies with high green density.

---

[1] Present address NGK Spark Plug Co., LTD. 2808 Iwasaki, Komaki-shi Aichi-Ken, 485 Japan

[2] Present address ABER Corp. Research Center, Mahawah, N.J. 07430

[3] Present address: Department of Chemical Engineering, University of Utah, Salt Lake City, Utah 84112, address as of January 1988 Materials Department Ecole Polytechnique Federal Lausanne, Switzerland

I. INTRODUCTION

A stable powder dispersion is necessary to produce uniform, dense ceramic green bodies. Two types of dispersion systems may be used: pure solvent systems and solvent-dispersant systems. Solvent-dispersant systems are known to be more effective for dispersing fine powders than pure solvent systems, however dispersants are more difficult to remove from the green body during binder burn-out.

Because the dispersion characteristics of powders are strongly dependent upon their surface characteristics, the extremely pure laser-SiC powders are expected to behave differently from commercial SiC powders with their oxidized surfaces. The dispersion characteristics of pure silicon powders made from laser heated SiH_4 were previously studied[1]. The dispersion stability of silicon powder was found to depend upon the dielectric constant of solvents.

This paper examines the dispersibility of both pure SiC powders made by laser synthesis and oxidized SiC powders in pure solvents without dispersants. To develop a more fundamental understanding of the solvent physical properties that are responsible for the dispersion of a particular type of powder, powder dispersion was correlated with the following solvent properties; dielectric constant, hydrogen bond index, acid dissociation constant (pK_a) and Lewis acid/base interaction energy.

II. EXPERIMENTAL

A. Materials

Three types of pure laser synthesized SiC powders made under

different conditions, one commercial SiC powder (Ibiden Betarandom Ultrafine), one commercial SiO_2 powder (Cabot Corp. Hi Sil 233) and an oxidized laser powder were used in this study. The powder synthesis conditions are given in Table I and their physical properties are summarized in Table II. The oxidized laser SiC powder was prepared by heating laser-SiC powder L014 in air at 600°C for 24 hours after breaking the soft agglomerates with a 30 minute exposure to a 40 watt ultrasonic probe with the powders dispersed in isopropyl alcohol. The oxidized powder had approximately the same surface area (single point BET), morphology (TEM) and crystal phase (XRD) as the pure laser SiC powder L014; the only difference was the presence of an oxidized layer on the particle surfaces as measured by FTIR.

Commercially available grades of organic solvents were used in this study (Table III). These solvents represent commonly available organic families, including aliphatic and aromatic hydrocarbons, chlorides, ethers, ketones, esters, alcohols, aldehydes, carboxylic acids, amines, and water. The solvents were dried with a 3A molecular sieve to ~ 30 ppm H_2O as measured by Karl Fisher titration. Also listed in Table III are various properties of these solvents, including dielectric constant, Lewis acid/base interaction parameters(also known as Drago[2] E and C values), hydrogen bond index, and pK_a values.

B. Microcalorimetry of Powder Surfaces

To characterize the various SiC powder surfaces, microcalorimetry was used to measure the heat of wetting. Calorimetry was performed using a Tronac™ 450 Isoperbol Calorimeter. All powder handling

techniques were anaerobic (<70ppm O_2) and anhydrous (<10ppm H_2O). Commercial SiO_2 powder and oxidized laser SiC powder were dried at 230°C for 24 hrs. under high purity nitrogen (i.e. <10ppm H_2O and <10ppm O_2) and cooled before loading into 3 ml ampules. After drying these powders were not exposed to air. After the ampules were loaded with a net weight of powder, the ampules were capped and removed from the glove box. Once outside the glove box the ampules were fused closed using a butane torch.

The sealed ampules were loaded into the stirring dewar of the calorimeter with 50 ml of solvent. The vessel was purged with Ultra-high purity Argon (Matheson Co.) and allowed to equilibrate for 8 hrs to stabilize the thermistor baseline drift. Then the ampule was broken below the liquid level by a calibrated solenoid push rod assembly. The reaction vessel temperature increase was monitored using a Thermistor.

Experimental heats of wetting for the various solvents are given in Table IV. Two solvents, triethylamine (TEA) and acetone, are bases; two solvents, chloroform and antimony pentachloride, are acids and one solvent, cyclohexane, is neutral. The E and C values and other pertinent physical properties of these solvents are given in Table V. Using Fowkes' method[8], the Lewis acid/base interaction energies (ΔH^{ab}) between solvents and powder surfaces were determined. Lewis acid/base interaction energies are given in Table VI. The heats of wetting (ΔH) were corrected for the dispersional interaction energy using the heat of wetting for cyclohexane which has only dispersional interactions not acid/base interactions[7,8].

Based on these Lewis acid/base interaction energies, Drago E and C values for the powder surfaces were determined using Fowkes' slope intercept plotting method[7]. The E and C values for the different powder surfaces are given in Table VII. They show the SiO_2 and the oxidized SiC powder to be acidic and the laser SiC powder to be basic. The E_A and C_A values measured for SiO_2 are similar to those reported by Fowkes[8] (E_A = 4.36(kcal/mole)$^{1/2}$, C_A = 1.06 (kcal/mole)$^{1/2}$).

These E and C values can be used to predict the Lewis acid/base interaction energy for a powder surface and another solvent using Drago's[2] four parameter theory

$$- \Delta H^{ab} = E_A E_B + C_A C_B \qquad [1]$$

where the E and C values of the powder surface is used for either the acid (sub A) or the base (sub B) and the solvent for the other E and C values. (Note: an acidic surface can only have an acid/base interaction with a basic solvent and vice versa.)

C. **Dispersion Tests**

Sedimentation tests were used to determine the stability of the SiC powders dispersed in the various solvents. Preparation of suspensions for sedimentation tests was conducted under a nitrogen atmosphere using a glove box. After a small amount of powder (10 mg) was mixed with the selected solvent (10 cm^3), the powder was dispersed by subjecting the suspension to a 40 watt ultrasonic probe for two

minutes. After standing for 5 days, the stabilities of the suspensions were evaluated visually. Very good (VG) dispersion showed most particles well-dispersed. Solvents that gave good (G) dispersions, showed some particles well dispersed and poor (P) dispersions showed most particles to have settled out after one day. When particles floated on top of the solvent and could not be incorporated into the liquid an (F) designation was used. Using these designations, the sedimentation tests are shown in Table VIII. The relative turbidity of the supernatant also shown in Table VIII was measured after one month using a Bryce Pheonix Photometer. Higher turbidity corresponds to better dispersion. Turbidity experimental results are summarized in Figure 1.

D. Coagulation Rates

The coagulation rates of pure and oxidized laser-SiC L014 powders in selected solvents were measured by photon correlation spectroscopy (PCS). Three kinds of solvents with different functional groups, propyl alcohol, propionic acid, and propylamine, were chosen for this measurement. The suspensions prepared as above were diluted to optimize the powder concentration for the PCS measurement. The powder concentration used in this study was 7.0×10^9 particles/cm^3. After ultrasonic agitation, the mean particle sizes were measured periodically with a Sub-Micron Particle Analyzer, Coulter Model N4. This data is shown in Figures 2 and 3. The coagulation rate constants given in Table IX were calculated from the size versus coagulation time data using a technique described by Barringer, et. al.[3] The viscosity of propyl alcohol and propionic acid used in the Photon

Correlation measurements were obtained from Weast[4] and that for propylamine was estimated using Soudre's method[5].

E. Centrifugal Packing

Suspensions consisting of 290 mg of SiC powder and 9 cm^3 of solvent were centrifugally cast at 3000 g's for 2 hours. The sediment volumes were determined by measuring their heights on the calibrated centrifuge tubes. After drying the sediments in a nitrogen atmosphere, sediment weights were measured to premit calculation of packing densities which are given in Table VIII. The microstructures of these sediments were observed with a scanning electron microscope (SEM).

F. Colloidal Pressing

For the colloidally pressed samples, 290 mg of L014 powder was dispersed in 9 cm^3 of either hexane or octyl alcohol solvents. The suspensions were placed in a 2.54 cm diameter press with a permeable membrane on the top die surface and pressed to 69 MPa (10,000 psi). When the solvent was completely removed, the pressure was released. The disk was dried, and its dimensions measured so that the green packing density could be calcuated.

III. RESULTS AND DISCUSSION

A. Dispersion Tests

The results of sedimentation tests, relative turbidity of the supernatant, and centrifugal casting summarized in Table VIII show significant differences in dispersibility between pure laser SiC powder and oxidized laser SiC powder but not between specific pure

powder types. In the case of pure laser SiC powders, "very good" dispersion was observed only for oleic acid. "Good" dispersion was observed for the other carboxylic acids (such as propionic acid and n-octanoic acid) and high molecular weight alcohols (such as n-octyl alcohol, ethylene glycol, etc). Oxidized laser SiC powders dispersed very well in many kinds of solvents such as all alcohols, propylamine, ethyl formate, and octanoic acid.

The relative turbidity values obtained are shown in Table VIII. For pure laser-SiC powder, the solvents with carboxylic acid groups such as oleic acid, octanoic acid, and propionic acid gave high relative turbidity corresponding to stable suspensions. For oxidized laser SiC powder propylamine, acetone, ethyl formate, and all the alcohols gave high relative turbidity values.

The relative turbidities for each solvent and for both oxidized and pure laser SiC powders are plotted in Figure 1. The data points are divided into the four areas encircled with dashed lines. Solvent groups are concentrated in specific areas. Carbolylic acids such as oleic acid, octanoic acid, and propionic acid are concentrated in the upper left, showing that these solvents dispersed pure powder well but not oxidized powder. Amine and alcohol solvents are concentrated in the lower right, showing that they dispersed oxidized SiC powder well but not pure SiC powder. While inert and amphoteric solvents were generally at the origin or on the diagonal, indicating that the powder surface did not influence turbidity.

Comparisons of the relative turbidity with the hydrogen bond index and pk_a(acid) and pk_a(base) values showed a great deal of scatter

without any discernible trends. The poor fit of turbidity with respect to pk_a(acid) and pk_a(base) is contrary to that observed by Bolger[6], where the arithmatic difference of either the isoelectric point (IEP) and the pk_a(acid) or the IEP and the pk_a(base) gave a parameter that correlated with powder dispersion.

Suspensions dispersion was also evaluated in terms of the dielectric constants[4] (ϵ) of the solvents to see whether high ϵ solvents favored stable suspensions and low ϵ solvents tended to give rise to flocculation. No correlation was found for pure SiC powders, e.g., propionic acid showed good dispersion characteristics in spite of its low ϵ. The oxidized powder gave results generally similar to those observed with silicon powder[4]: dispersion stability generally improved with the increasing dielectric constant of the solvent, as shown in Figure 2.

The comparison between dispersibilities of pure laser SiC powders and oxidized laser SiC powders is shown in Table IX for the families of organic solvents studied. Some solvent families, such as carboxylic acid, amine, etc., showed different dispersibilities depending upon the specific powder type and member of the solvent family. These phenomena may be related to the acidity and basicity of the solvents and powder surfaces. Propylamine and low molecular weight alcohols act as Lewis bases, dispersing oxidized laser SiC powder well, but not pure laser SiC powder in spite of high hydrogen bond indexes. In contrast, oleic acid and propionic acid act as Lewis acids, dispersing pure laser SiC powder well but not oxidized laser SiC powder.

B. Coagulation Rates

The mean particle sizes for pure laser-SiC powder were plotted as a function of coagulation time in Figure 3. The mean particle size for propyl alcohol and propylamine increased with coagulation time, but propionic acid showed almost constant size within the measuring time of 180 minutes. In contrast the oxidized laser-SiC powder showed a different trend, as shown in Figure 4. The particles dispersed in propyl alcohol or propylamine were stable, and the particles dispersed in propionic acid coagulated rapidly. The coagulation rate constant, k, was calculated from the slope of the size versus time curves shown in Figures 3 and 4. These values are given in Table X. Smaller values of the coagulation rate constant indicate more stable dispersions.

C. Centrifugal Packing

Packing densities of centrifugal sediments are given in Table VIII for various solvents. Packing densities were directly related to the liquid functional group and the powder type. For pure laser SiC powders, octyl alcohol showed the highest packing densities. The packing densities for oleic acid, the best solvent in the sedimentation test, were not very high. A strong correlation between centrifugal packing densities and the sedimentation results was observed for the commercial powder, which had an oxidized surface layer, while some exceptions were observed for pure laser SiC powders. These exceptions may be attributed to the relatively low dispersibilities of these particular pure laser SiC powders. The average packing densities of the laser SiC powders increased in the

following order: B038, B060, L014. The commercial powder had a higher average packing density than the laser SiC powders.

Significant differences between the centrifugal sediment densities were observed among the four kinds of powders, B038, B060, L014, and the commercial powder. These differences should be attributable to powder characteristics such as particle size, particle size distribution, particle morphology, and aggregation. Packing density should be independent of particle size, when the particles are large enough to neglect electrostatic forces, surface films, and boundary effects. An increased width of the particle size distribution increases the packing density. High aspect ratio particles pack to higher densities than spheres as a result of orientation. Spheres can pack most uniformly. Agglomerates and aggregates generally (but not always) have lower packing densities than individual particles.

The packing densities achieved with type L014 powder were consistently higher than those achieved with type B038 and B060 powders. Although type L014 powder was approximately twice as large as the other two, it is unlikely that this difference was responsible for its improved packing density. All three exhibited nominally the same dispersibilities. The B038 and B060 powders consist of aggregated primary particles which can be dispersed but not packed well. The high packing densities achieved with the commercial powder is attributable to wide particle size distribution and morphology.

Packing densities of centrifugal sediments as a function of hydrogen bond indexes of the solvents are shown in Figure 5. Hydrogen bond indexes were obtained from the Paint Technology Manual[9].

Reasonably good correlations were observed between packing densities of all powders and hydrogen bond indices of the solvent. High hydrogen bond indices provided high packing densities. Good correlations between the hydrogen bond index and sedimentation results were also observed for the oxidized powder. However, sedimentation results for the pure powders and the differences in dispersibilities between pure and oxidized SiC powders could not be interpreted solely with hydrogen bond index.

Using equation 1, the Lewis acid/base interaction energy for each type of SiC powder was calculated for each solvent with appropriate E and C values listed in Table III. These Lewis acid/base interactions were correlated with the turbidity data listed in Table III without success. The correlation of packing density of centrifugal sediments with Lewis Acid/base interaction energies are shown in Figures 6 and 7. For both oxidized SiC laser powder (Figure 6) and pure SiC laser powder (Figure 7), the packing density is generally high when the Lewis acid/base interaction energy is high. Some degree of scatter in the data is observed. This correlation between packing density and Lewis acid/base interaction energy suggests that acid-base interactions are one but not the only factor in dispersion and packing of non-oxide ceramic powders.

D. Characterization of Sediment and Colloidally Pressed Bodies

The micrographs of the top surfaces of centrifugal sediments from suspensions of L014 with hexane and oxtyl alcohol are shown in Figure 8. These packing densities are 20.5% and 33.2%, respectively. The particles dispersed in octyl alcohol are packed much better, as shown

by the smaller number of large voids and loosely packed agglomerates.

Micrographs of a fracture surface and a side surface of a colloidal pressed pellet using octyl alcohol are shown in Figure 9. No voids larger than the particle size are present, and several areas show ideal close packing of spheres. The packing density of this pellet was about 62%.

IV. CONCLUSIONS

An evaluation of the effect of solvent properties on pure and oxidized SiC powder dispersibility and packing density has been performed. Dielectric constant, pH_a, hydrogen bond index and Lewis acid/base interaction energy did not correlate well with powder dispersibility. Packing density was correlated with high hydrogen bond index and high Lewis acid/base interaction energy, however, a large amount of scatter was observed with with both correlations.

Heat of wetting studies showed that oxidized SiC powders, either laser or commercial, have an acidic surface and were dispersed best by basic solvents. Pure laser-synthesized SiC powder was shown to have a basic surface and was dispersed best by acidic solvents. Oleic acid showed the best dispersibility for pure laser SiC powder, however it may not be desirable for ceramic processing because it has a high viscosity and a high boiling point. Octyl alcohol is the most suitable pure solvent studied for both pure and oxidized SiC powder. Using colloidal pressing with pure SiC powder and octyl alcohol, uniform and high density (~62%) green bodies were obtained showing that good dispersibility gave ceramic green bodies with high green

density.

V. Acknowledgement

The research was supported by the Office of Naval Research and Army Research Office under Contract N00014-82-K0350 and a group of industrial sponsors (Abex Corp., Aisin Seiki, Alcoa, Japan Steel Works, NGK Spark plug, Nippon Steel Corp., Sumitomo Electric Corp., and Toa Nenryo Kogyo). One author (TAR) was funded by the National Science Foundation contract number 8617500. These and other contributions are gratefully acknowledged.

REFERENCES

1. Mitzuta, S. Cannon, W.R., Bleier, A. and Haggerty, J.S."Dispersion and Casting of Silicon Powder without Deflocculants", Am. Ceram. Soc. Bull., 61,8,872-5(1982).

2. Drago, R.S., IXogel, G.C., and Needham, T.E., "A Four-Parameter Equation for Predicting Enthalpies of Adduct Formation", J.Am. Chem. Soc. 93, 6014-6020 (1971).

3. Barringer, E.A., Novich, B.E. and Ring, T.A. "Determination of Colloid Stability Using Photon Correlation Spectroscopy", J. Colloid Interface Sci.100,584-586 (1984).

4. Weast, E. "Handbook of Chemistry and Physics", 47th Edition, 1967.

5. Soudres, M. Jr., "Viscosity Prediction Equations", J. Am. Chem. Soc., 60, 154-6(1938)

6. Bolger, J.C. "Acid Base Interactions between Oxide Surfaces and Polar Organic Compounds",in Acid Base Interactions edited by K.L. Mittal, Elsevier, New York, 1981 p4-18.

7. Fowkes, F.M. and Mostafa, M.A. "Acid-Base Interactions in Polymer Adsorption", Ind. Eng. Chem. Prod. Res. Dev. 17, 3-7 (1978).

8. Fowkes, F.M., "Acid-Base Contributions to Polymer-Filler Interactions", Rubber Chemistry and Technology, 57, 1984, pp. 328-44.

9. "Paint Technology Manual" E. I. Dupont Nemours Company, 1968, p 6-12.

FIGURE LEGENDS

Figure 1. Comparison of Relative Turbidity of Pure and Oxidized SiC Powder.

Figure 2. Relative Turbidity versus Dielectric Constant of Solvent.

Figure 3. PCS Mean Size versus Coagulation Time For Pure L014 SiC Powder.

Figure 4. PCS Mean Size versus Coagulation Time For Oxidized L014 SiCPowder.

Figure 5. Centrifugal Packing Density versus Hydrogen Bond Index of Solvent.

Figure 6. Packing Density versus Lewis Acid/Base Interaction Energy of the Oxidized SiC Powder With the Solvent.

Figure 7. Packing Density versus Lewis Acid/Base Interaction Energy of the Pure SiC Powder With the Solvent.

Figure 8. SEM Micrographs of Centrifugally Packed Sediments A) L014 in Hexane, and B) L014 in Octyl Alcohol.

Figure 9. SEM Micrographs of Colloidally Pressed Compact of L014 Powder in Octyl Alcohol A) Fracture Surface, and B) Top Surface.

TABLE I

LASER-POWDER SYNTHESIS CONDITIONS

Run Number	Carbon Reactant	Laser Power (W)	Reaction Temp (°C)
B038	Ethylene	150	1650
B060	Methane	150	1680
L014	Methane	500	1830

TABLE II

CHARACTERISTICS OF POWDERS

	Laser-Powders			Commercial SiC	Oxidized SiC	Commercial SiO2
	B038	B060	L014			
TEM Particle size (nm)	31	52	90	130	90	
Specific surface area (m^2/g)	44.9	44.3	22.4	19.4	23.3	133
Phase	β	β	β	β	β	
Size distribution	narrow			wide	narrow	wide
Morphology	spherical			irregular	spherical	spherical
Surface	pure					

TABLE III

SOLVENTS USED AND RESULTS OF SCREENING TESTS

SOLVENT	DRAGO[2] E&C VALUES C_A	C_B	E_A	E_B (kcal/mole)$^{1/2}$	Hydrogen Bond Index[9]	pKa[6] (acid)	pKa[6] (base)
HYDROCARBONS							
1 hexane					2.2		
2 toluene		1.91		0.087	3.0	37	
CHLORIDES							
3 methylene chloride	0.02		3.40		2.7		
4 chloroform	0.150		3.31		2.2		
5 carbon tetrachloride					2.2		
6 1,2-dichloroethane					2.7		
7 trichloroethylene					2.5		
8 chlorobenzene					2.7		
CYANIDE							
9 acetonitrile		1.34		0.886	4.5	25	-10.1
ETHERS							
10 isopenthyl ether		3.19		1.11	(6.0)		
11 tetrahydrofuran		4.27		0.978	5.3		- 2.2
12 dioxane		2.38		1.09	5.7		- 2.9
KETONES							
13 acetone		2.33		0.987	5.7	20	- 7.2
14 2-butanone		2.38		1.09	5.0		
15 2-heptanone					(5.5)		
ESTERS							
16 ethyl formate					5.5		
17 ethyl acetate		1.74		0.975	5.2	26	- 6.5
ALDEHYDE							
18 benzaldehyde					5.2	14.9	- 7.1
ALCOHOLS							
19 methyl alcohol		1.12		0.975	8.9	16	- 2.2
20 ethyl alcohol	0.451		3.88		8.9	16	
21 n-propyl alcohol					8.9		
22 2-propyl alcohol					8.9		
23 2-furfuryl alcohol					(8.9)		- 3.2
24 benzyl alcohol	0.446		4.17		8.9		
25 n-octyl alcohol					8.9		
26 ethylene glycol					9.6	15.1	
AMINE							
27 propylamine		6.1		1.4	9.0		10.7
CARBOXYLIC ACID							
28 propionic acid					9.5	4.87	
29 n-octanoic acid					9.5	4.89	
30 oleic acid					9.5		
INORGANIC							
31 water	0.571		1.64				

Table IV.

Measured Heats of Wetting ($-\Delta H$ kcal/mole)

Powder	SiO_2 (Hi Sil-233)	SiC (L-014)	OxSiC (L-014)
TEA	22.0	22.8	13.59
Acetone	12.09	10.9	10.66
Cyclohexane	7.97	9.29	8.43
Choloroform	11.0	14.7	9.24
$SbCl_5$	110.8	31.2	30.2

Table V.

Solvent Properties

Solvent	Density (g/cm^3)	Molecular Weight (g/mole)	Molar Surface Area (m^2/mole x 10^5)	Surface Energy ($ergs/cm^2$)	E_B	C_B	E_A	C_A
					(kcal/mole)$^{1/2}$			
TEA	0.727	101.2	2.267	22.7	0.991	11.09	--	--
Acetone	0.790	58.1	1.482	23.7	0.987	2.33	--	--
Cyclohexane	0.779	84.2	1.927	25.5	--	--	--	--
Chloroform	1.483	119 4	1.575	27.1	--	--	3.31	0.15
$SbCl_5$	2.336	299.0	2.145	35.8	--	--	7.38	5.13

Table VI.

Lewis Acid/Base Interactional Energies ($-\Delta H^{ab}$ kcal/mole)

	SiO_2 Hi Sil -233	SiC L-014	OxSiC L-014
TEA	12.1	14.0	5.62
Acetone	6.12	1.96	2.51
Cyclohexane	-0.09	--	--
Chloroform	4.23	5.12	0.53
$SbCl_5$	101.3	20.2	20.2

Table VII

Drago E and C Values
$(kcal/mole)^{1/2}$

Powder	E_A	C_A	E_B	C_B
SiO_2(Hi-Sil-233)	4.65	0.66	--	--
Laser SiC	--	--	1.85	1.47
ox-SiC	1.45	0.43	--	--

TABLE VIII

RESULTS OF SCREENING TESTS AND CENTRIFUGAL CASTING TESTS

SOLVENT	DISPERSI-BILITY		RELATIVE TURBIDITY		PACKING DENSITY(%)			
	Pure	Oxid.	Pure	Oxid.	B038	B060	L014	Comml.
HYDROCARBONS								
1 hexane	P	P	0	0	11.9	16.4	20.5	28.4
2 toluene	P	P	0	0	12.8	19.5	23.6	31.0
CHLORIDES								
3 methylene chloride	G	G	1.9	1.3	11.8	17.2	23.9	26.8
4 chloroform	G	G	3.6	0	14.0	17.0	26.8	29.0
5 carbon tetrachloride	P	P	0	0	11.3	16.7	25.9	26.9
6 1,2-dichloroethane	G	G	3.6	0	14.0	19.8	25.6	29.4
7 trichloroethylene	P	P	0	0	12.8	17.7	25.9	27.7
8 chlorobenzene	P	P	0	0	13.9	18.7	26.2	30.9
CYANIDE								
9 acetonitrile	G	G	3.0	3.5	11.1	15.8	25.1	34.8
ETHERS								
10 isopenthyl ether	G	P	0	0	-	25.5	29.0	34.4
11 tetrahydrofuran	G	G	3.6	1.3	13.6	21.8		34.1
12 dioxane	P	P	0	0	16.1	25.8	28.7	36.7
KETONES								
13 acetone	G	G	3.6	3.7	14.7	18.3	26.8	38.0
14 2-butanone	G	G	0	3.4	15.5	20.7	26.2	34.9
15 2-heptanone	P	G	0	2.7	-	22.2	27.5	36.9
ESTERS								
16 ethyl formate	P	VG	0	3.5	12.2	22.3	-	33.0
17 ethyl acetate	G	G	3.6	3.5	15.0	22.3	26.4	34.6
ALDEHYDE								
18 benzaldehyde	P	VG	0	2.2	-	26.5	29.5	39.1
ALCOHOLS								
19 methyl alcohol	P	VG	0	2.3	16.2	24.3	25.0	37.6
20 ethyl alcohol	P	VG	0	3.2	16.1	25.2	27.7	37.8
21 n-propyl alcohol	P	VG	0	2.9	16.2	25.1	27.0	37.4
22 2-propyl alcohol	P	VG	0	3.3	16.3	25.6	30.2	38.6
23 2-furfuryl alcohol	P	VG	-		-	-	28.9	38.8
24 benzyl alcohol	P	VG	0	3.3	-	25.1	31.2	41.5
25 n-octyl alcohol	G	VG	0	1.6	-	26.4	32.4	38.4
26 ethylene glycol	G	VG	3.3	3.5	-	15.4	22.8	39.0
AMINE								
27 propylamine	P	VG	0	4.2	12.7	21.8	28.3	40.2
CARBOXYLIC ACID								
28 propionic acid	G	P	3.4	0	-	21.0	27.4	35.9
29 n-octanoic acid	G	G	2.5	0	-	22.7	29.7	39.9
30 oleic acid	VG	G	3.8	0	-	22.3	25.7	32.4
INORGANIC								
31 water	F	G			11.0	16.5	20.3	36.8

P: poor dispersion
G: good dispersion
VG: very good dispersion
F: flotation

TABLE IX

COMPARISON OF DISPERSIBILITY

BETWEEN PURE LASER-POWDER AND OXIDIZED LASER-POWDER

		DISPERSIBILITY FOR OXIDIZED POWDERS		
		Poor	Good	Very Good
DISPERSIBILITY FOR PURE POWDER	Poor	Hydrocarbons Chlorides Ether	Ketone	Amine Low-alcohols Ester Aldehyde
	Good	Ether Carboxylic acid	Ketones Ester Ether Nitrile Chlorides Carboxylic acid	High-alcohols
	Very Good	Carboxylic acid		

TABLE X

Coagulation Rate Constant, K (cm^3/sec)

Solvent	Pure Powder	Oxidized Powder
2-propyl alcohol	1.23E-11	1.37E-12
propionic acid	7.41E-14	1.37E-11
2-propyl amine	3.38E-12	5.15E-14

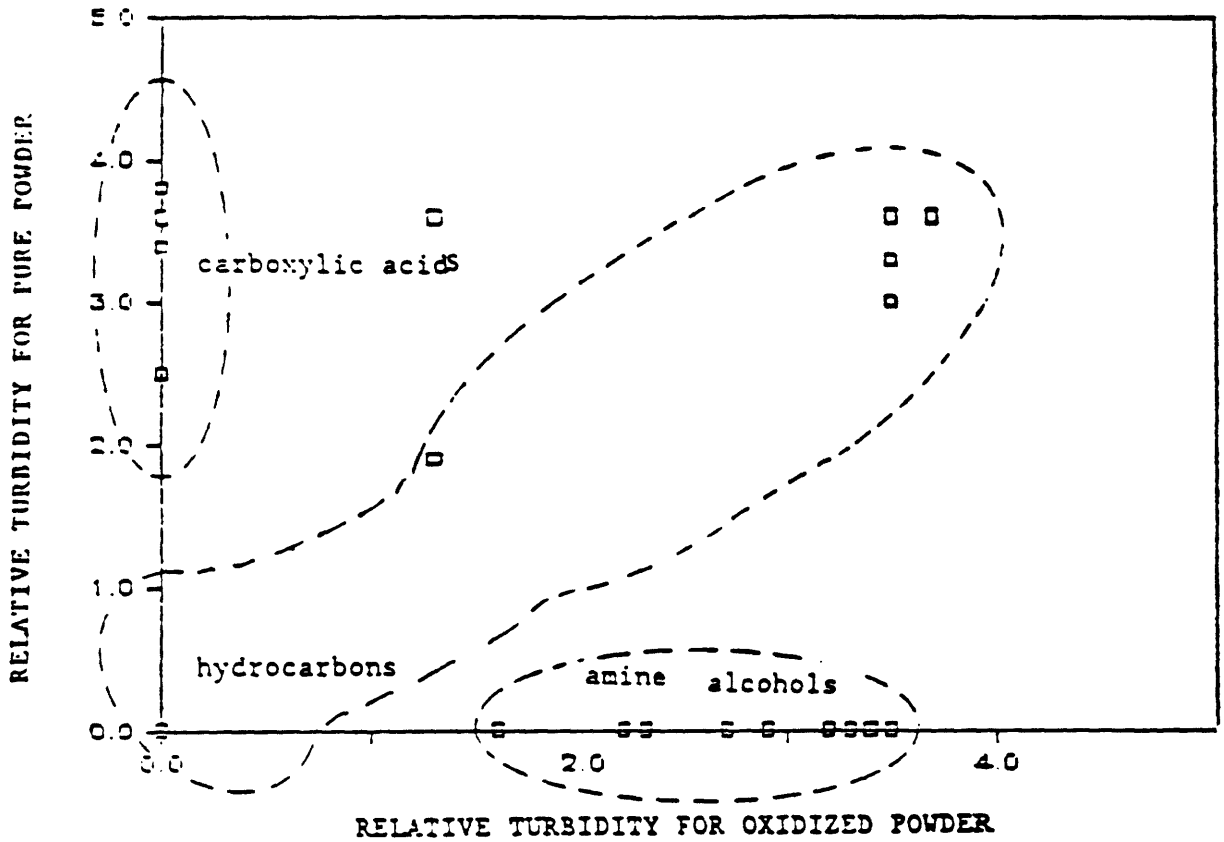

Fig. 1 Comparison of Relative Turbidity of Pure and Oxidized Powder

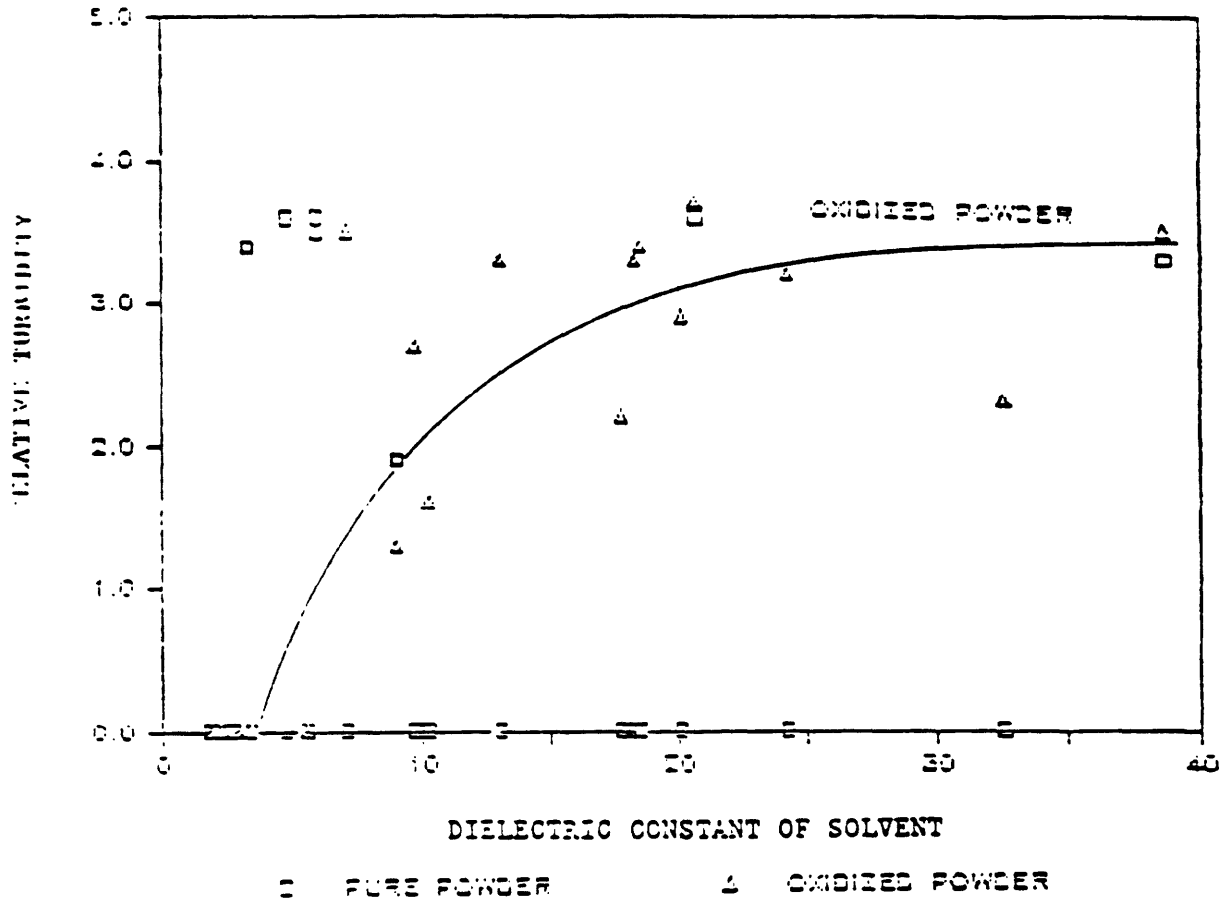

Fig. 2 Relative Turbidity as a Function of Dielectric Constant of Solvents

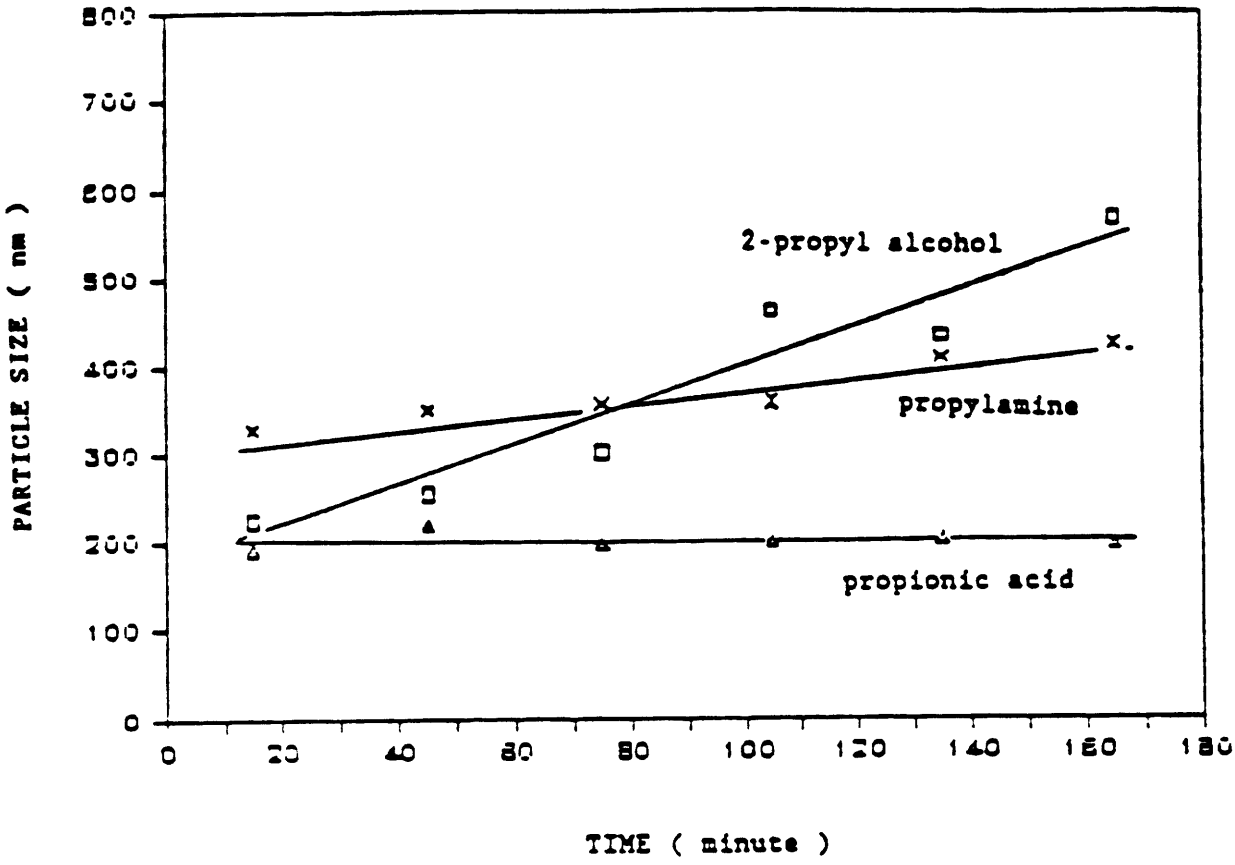

Fig. 3 Particle Size versus Coagulation Time for Pure SiC Powder

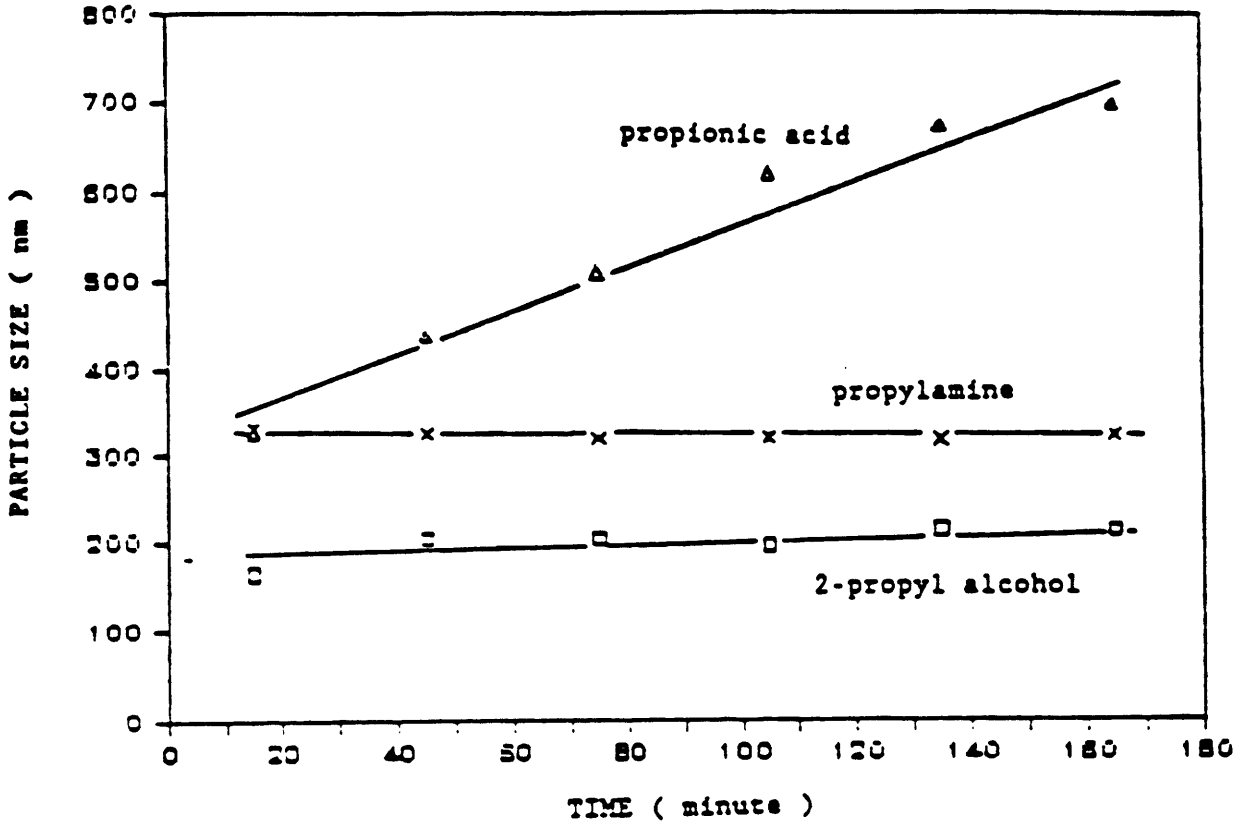

Fig. 4 Particle Size versus
Coaguation Time for Oxidized SiC Powder

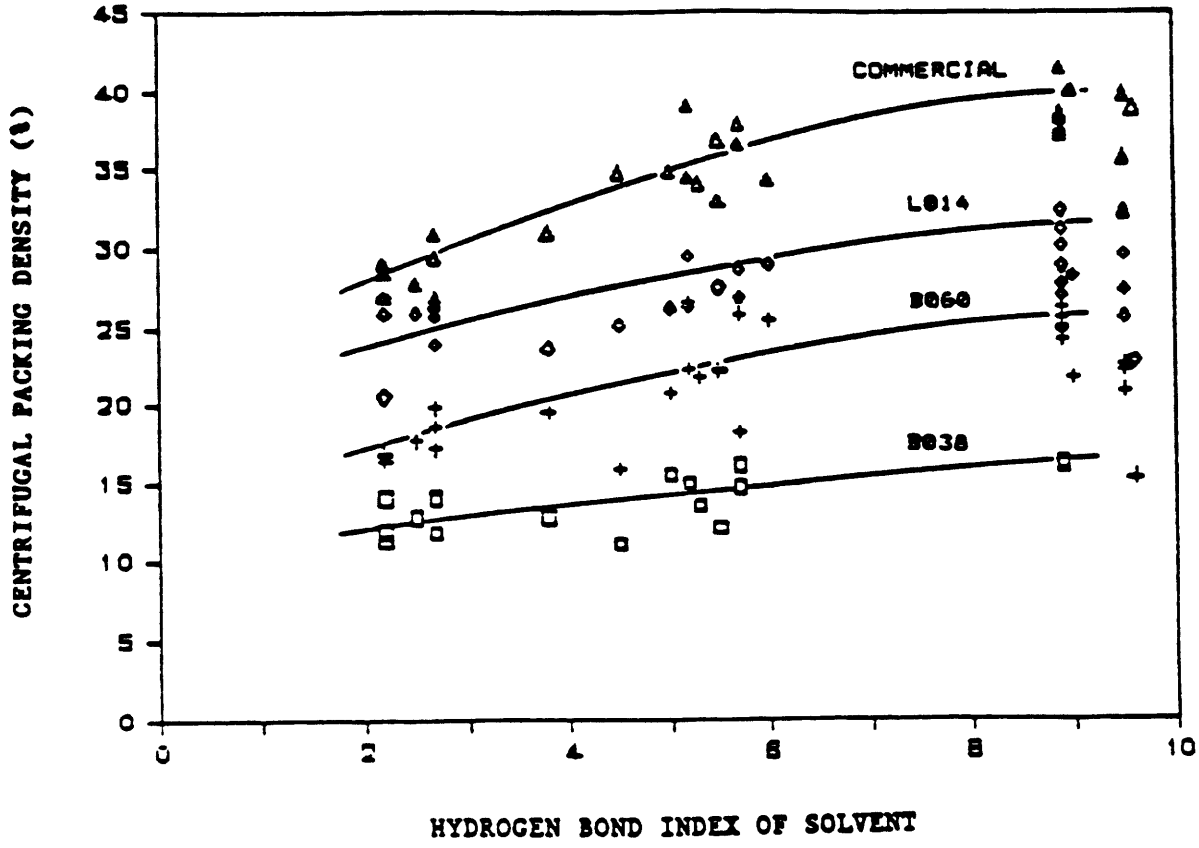

Fig. 5 Centrifugal Packing Densities as a function of Hydrogen Bond Indexes of Solvents.

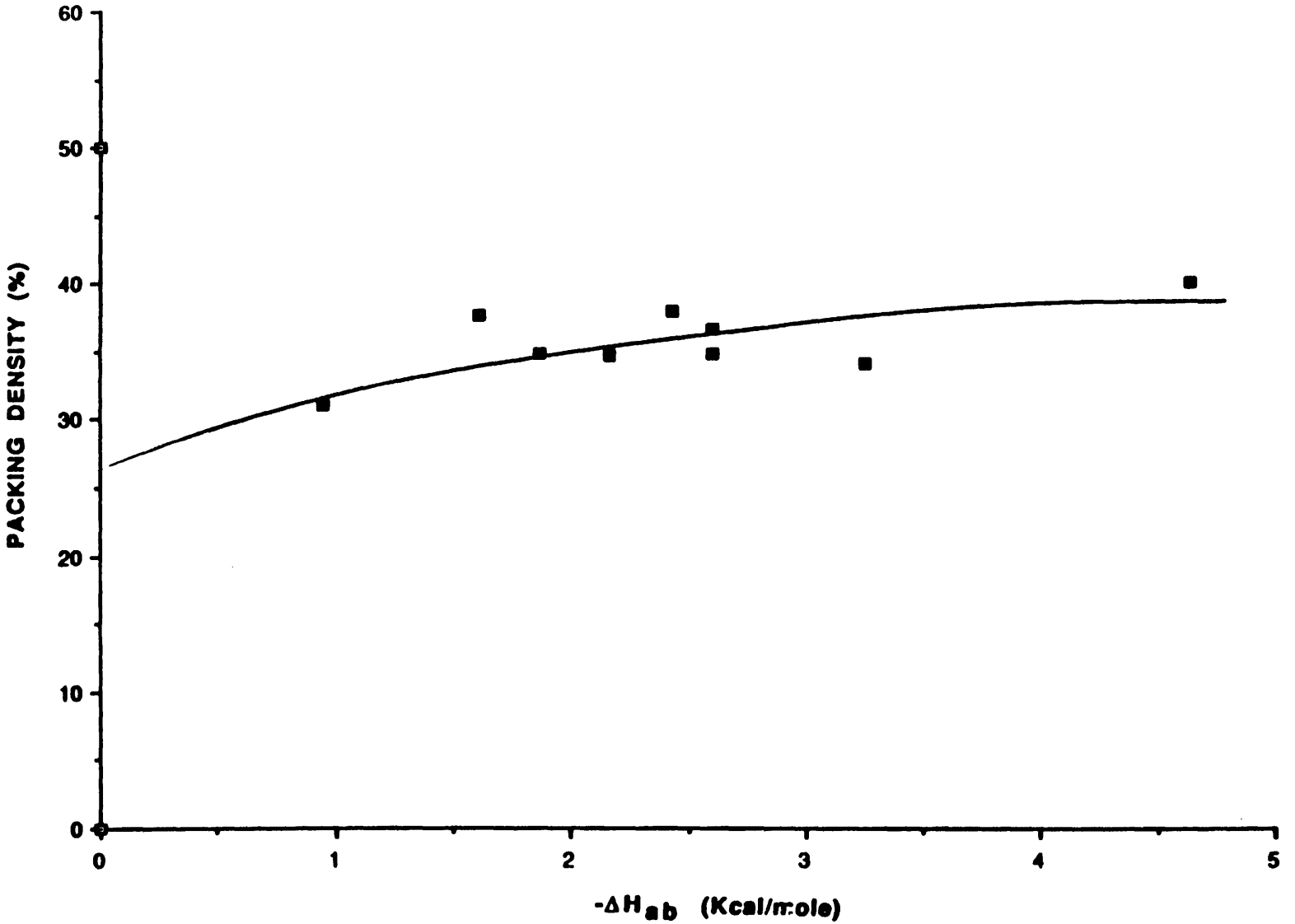

Figure 6. Oxidized-SiC, E_A = 1.45 (Kcal/mole)$^{1/2}$, C_A = 0.43 (Kcal/mole)$^{1/2}$.

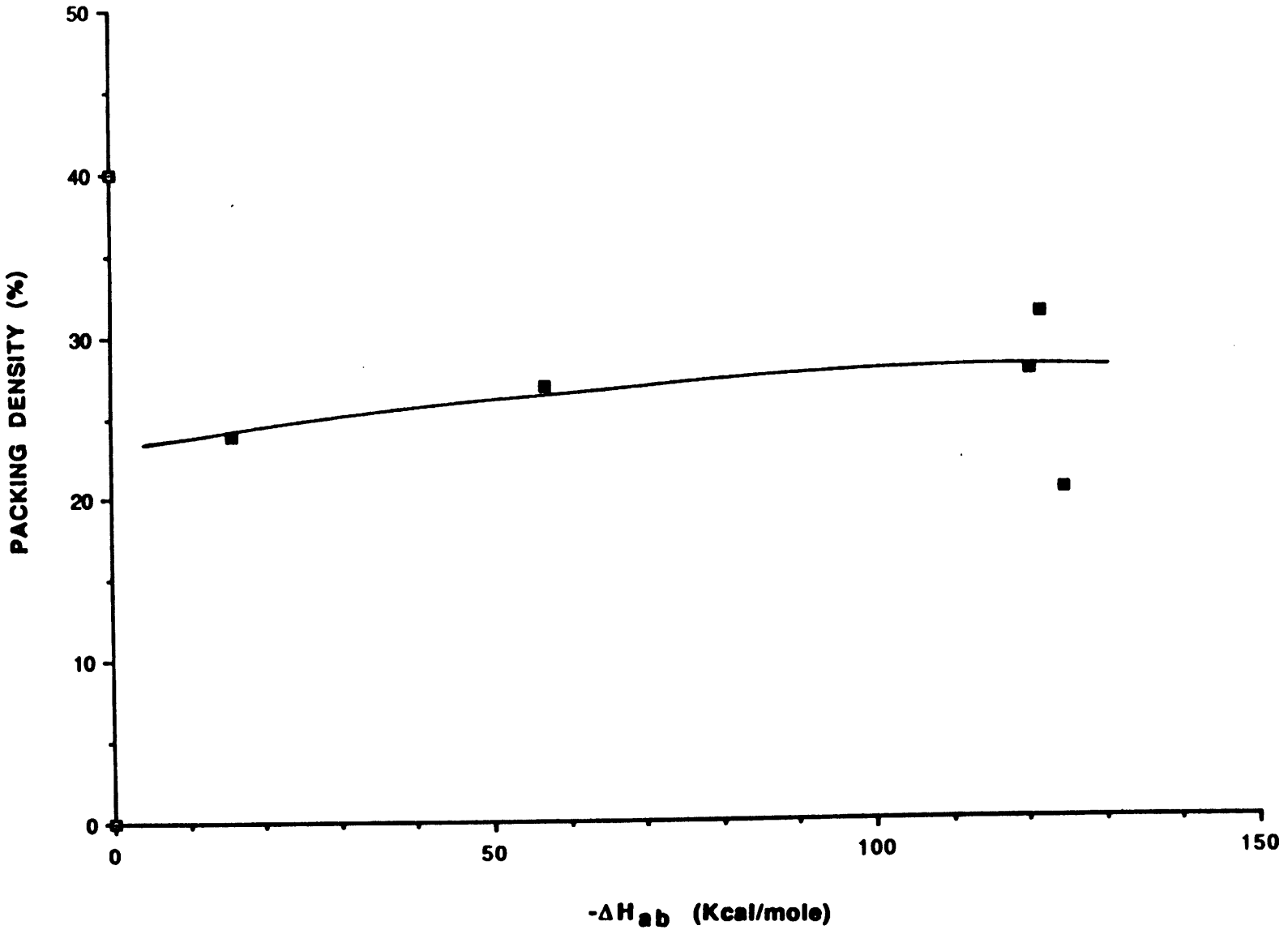

Figure 7. Pure SiC, E_B = 8.4 (Kcal/mole)$^{1/2}$,
C_B = 19.4 (Kcal/mole)$^{1/2}$.

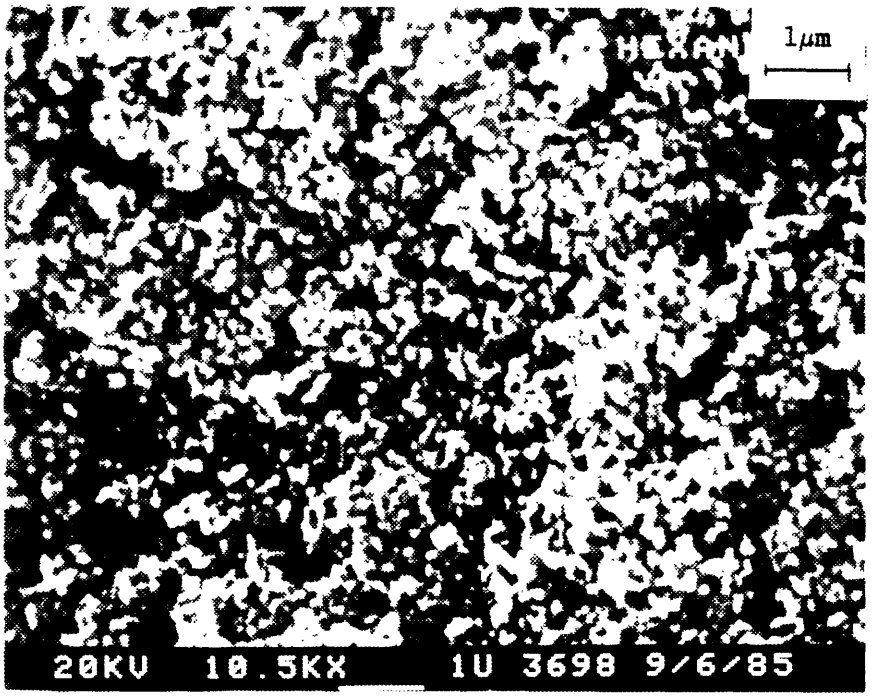

a

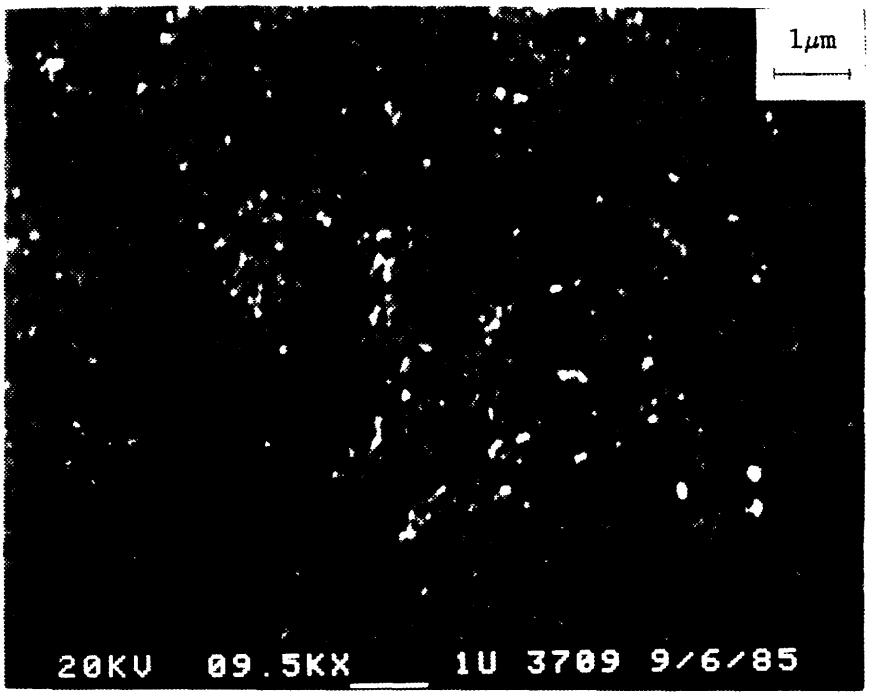

b

Figure 8. SEM Micrographs of Centrifugally Packed Sediments A) L014 in Hexane, and B) L014 in Octyl Alcohol.

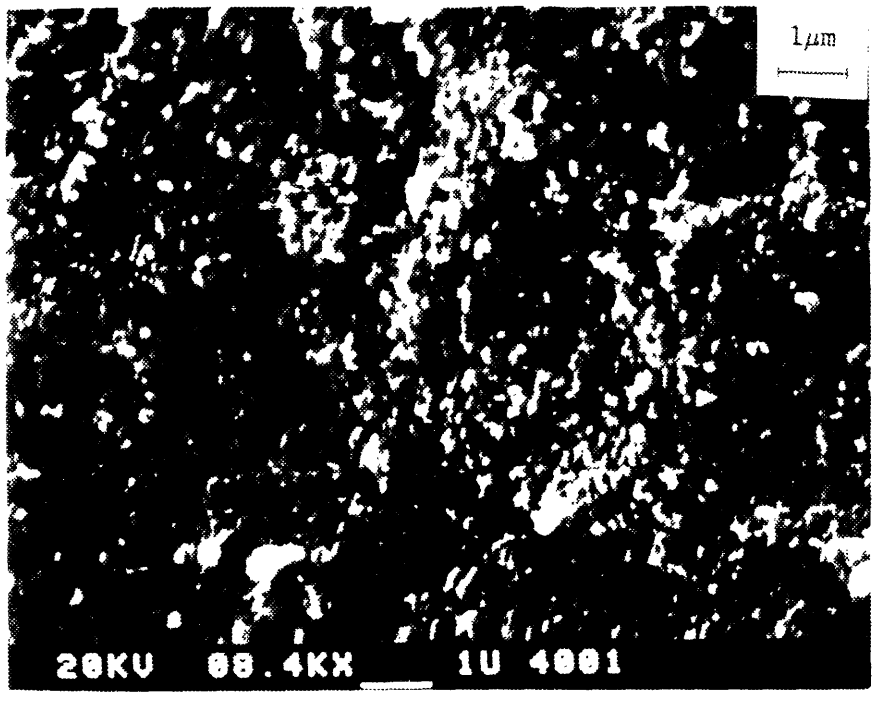

a

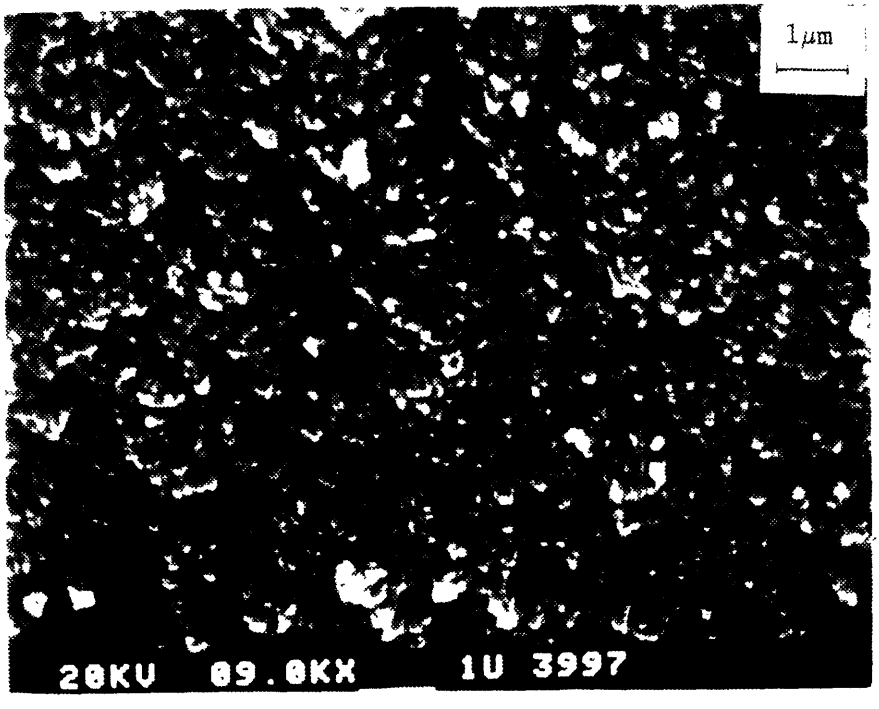

b

Figure 9. SEM Micrographs of Colloidally Pressed Compact of L014 Powder in Octyl Alcohol A) Fracture Surface, and B) Top Surface.

ADVANCED CERAMIC MATERIALS, 3 [2] 162–66 (1988)

Drying of Silicon Powder Compacts

DANIEL CASTRO, TERRY A. RING,*,* and JOHN S. HAGGERTY*
Massachusetts Institute of Technology, Cambridge, MA 02139

Laser-synthesized silicon powder with an average size of 0.28 μm was colloidally pressed into disks 1.27 cm in diameter using various solvents. Thermogravimetric analysis (TGA) was performed during the solvent removal at various temperatures. Two types of weight loss were observed: one proportional to time, t, indicating that external mass transfer is the rate-limiting step, and the other proportional to $t^{1/2}$, indicating that pore diffusion is the rate-determining step. After losing >99% of the solvent weight, samples were examined by Fourier transform ir spectroscopy to determine the amount of solvent that remained adsorbed on the surface of the silicon powder as a function of time for various temperatures. Temperatures much higher than the boiling points of the solvents are required to completely dry the silicon compacts.

Controlling the drying process of powder compacts is important in ceramics processing, soil science, and powder metallurgy. Macy[1] discussed both the shrinking of clay green bodies during drying and the internal mechanism of water migration during drying. Packard[2] discussed moisture stress in clay green bodies during drying. Cooper[3] developed a quantitative theory of cracking during the drying of clay green bodies using an analogy based on thermal gradients in glass objects.

This study examines the drying rate of silicon powder compacts which were colloidally pressed at 68.9 MPa (10 000 psi). Thermogravimetric analysis (TGA) was used to measure the solvent weight loss of the silicon powder compacts. Fourier transform infrared spectroscopy (FTIR) was used to follow the loss of the solvent remaining on the powder surface after drying at 50°C for 48 h. The silicon powders used in this study were nitrided after drying to form reaction-bonded Si_3N_4 (RBSN). Maximum permissible firing rates and nitriding kinetics were found to depend on complete removal of solvent from the silicon powder compacts. Nitriding results will not be discussed in this paper. In a general sense, these drying results obtained apply to all ceramic green bodies made from powder having a small diameter and high surface area.

EXPERIMENTAL PROCEDURE

The silicon powder used in this study was synthesized as an aerosol from silane using a CO_2 laser to initiate and sustain the decomposition reaction.[4–6] The silicon aerosol was collected on filters and moved to a glove box under argon atmosphere. Because of the argon-hydrogen atmosphere in which the silicon powder was made, it had an Si–H surface, as observed by FTIR[7]; the silicon powder is shown in Fig. 1. Image analysis of several hundred particles on several transmission electron microscopy (TEM) micrographs like that in Fig. 1 gave a log-normal size distribution with a geometric mass mean size of 280.0 nm and a geometric standard deviation of 1.7. Some agglomeration of the particles is observed in Fig. 1.

In a glove box, the silicon powder was mixed with solvent to form a 1% solids suspension. Reagent-grade octanol, methanol, and acetonitrile were used as solvents without further purification. No dispersants were used to prepare suspensions. Various amounts of this suspension were placed in a colloid press 1.27 cm in diameter and pressed at 68.9 MPa (10 000 psi) for 5 min to remove most of the solvent. Two thicknesses were produced: 4 and 2 mm. The packing density, based on the weight of silicon powder used and the dimensions of the sample, was 68% and did not change significantly during drying. Mercury porosimetry could not be used to measure the pore size distribution because of the friability of the dried compact. After the pellet samples were pressed, they were placed in a desiccator in an atmosphere saturated with the solvent, and TGA measurements were taken.[*]

The pellet samples were placed on the platform and the furnace, already up to temperature, was quickly placed over the sample with the N_2 flowing at predetermined rates. Three solvents, two sample thicknesses, and three gas velocities were used to separate the effects of boundary-layer thickness, vapor pressure, and pore diffusion. These samples were placed directly on a preheated pedestal with good thermal contact to avoid heat transfer through the boundary layer as one possible heat transfer mechanism. The pedestal also prevented vapor losses from the bottom surface of the pellets, simplifying the theoretical analysis to a one-dimensional model (assuming negligible vapor loss through the sides).

Methanol- and acetonitrile-dispersed samples were dried at 50°C for 48 h and examined using a Fourier transform infrared spectrometer.[‡] The pellet samples were placed in a heated ir reflectance cell, which was maintained at a constant temperature up to 300°C in N_2 and scanned periodically for up to 5 h.

Fig. 1. Transmission electron micrograph of laser-synthesized silicon powder (bar = 1 μm).

*Member, the American Ceramic Society.
*Present address: University of Utah, Dept. of Chem. Eng., Salt Lake City, UT 84112; after January 1, 1988: Ecole Polytechnique Fédérale Lausanne, 34 Chemin de Bellerive, CH 1007 Lausanne, Switzerland.
[*]Model STA 492, Netzsch, Inc. Exton, PA.
[‡]Model IR/85, IBM Instruments Inc., Armonk, NY.

Manuscript No. 199731. Received February 19, 1987; approved September 25, 1987.
Supported by the office of Naval Research and Army Research Office under Contract N00014-82-K-0350, National Science Foundation (TAR), and by a group of industrial sponsors (Abex Corp., Aisin Seiki, Alcoa, Japan Steel Works, NGK Spark Plug, Nippon Steel Corp., Sumitomo Electric Corp., and Toa Nenryo Kogyo).

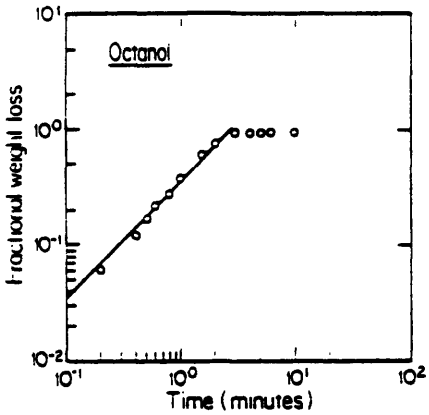

Fig. 2. Log-log plot of weight loss vs time for 2-mm octanol sample dried at 200°C with 0.1 cm/s N_2 velocity.

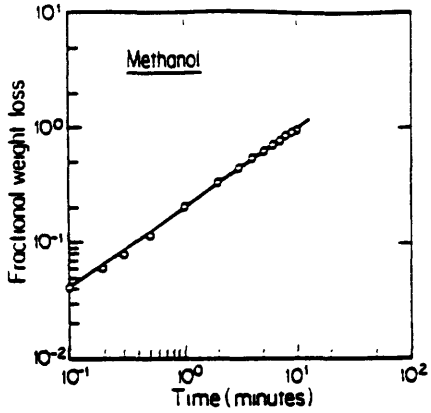

Fig. 3. Log-log plot of weight loss vs time for 4-mm methanol sample dried at 80°C with 1.3 cm/s N_2 velocity.

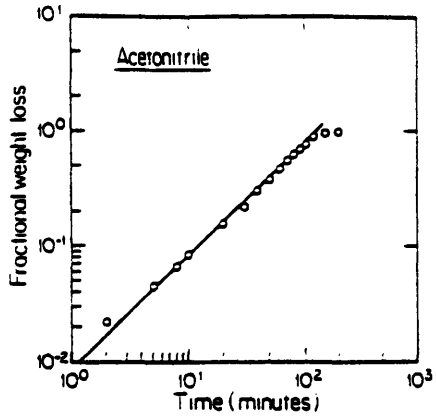

Fig. 4. Log-log plot of weight loss vs time for 2-mm acetonitrile sample dried at 27°C with ≈0 cm/s N_2 velocity.

EXPERIMENTAL RESULTS

Figure 2 shows the weight loss plotted on a log-log scale of a 2-mm-thick octanol sample dried at 200°C in N_2 flowing at a velocity of 0.1 cm/s. For most of the weight loss (i.e. 0 to 90%), a single line is followed which has a slope of one. Above 90%, an asymptotic weight loss is observed. Figure 3 shows the weight loss plotted on a log-log scale of a 4-mm-thick methanol sample dried at 80°C in N_2 flowing at a velocity of 1.3 cm/s. A linear weight loss with a slope of 0.6 is observed with this sample from 0% to 99%. Figure 4 shows the weight loss plotted on a log-log scale of a 2-mm-thick acetonitrile sample dried at 27°C in nearly stagnant N_2. For most of the weight loss (i.e. 0 to 90%), a single line is followed which has a slope of one. Above 90%, an asymptotic weight loss is observed.

Figure 5 shows examples of the FTIR spectra for an acetonitrile sample as a function of heating time at 300°C. The unheated sample revealed peaks at 3850, 2925, ≈2100, and 1100 cm^{-1} (not shown) wave numbers. The peak at 3850 cm^{-1} corresponds to O–H.[8] and the 1100-cm^{-1} peak corresponds to either Si–O or C–O[8]; both increase in intensity as time at temperature increases. The 2100-cm^{-1} peak corresponds to Si-H[8]; it shifts to a higher frequency by 150 cm^{-1} wave numbers as the 1100 cm^{-1} peak increases in intensity. Oxidation of the Si–H species will alter the frequency at which that bond stretches.[9] As the Si–H peak shifts, a new peak appears in the 3850 cm^{-1} region, which corresponds to O–H.[8] The peak is as sharp as that of the Si–O–H peak on silica gel and suggests hydrolysis of the silicon powder during heating. The peak at 2925 cm^{-1}, corresponding to C–H, decreases as time at temperature increases. This peak height was used with the Kubelka-Munk[10] equation to determine the concentration of the solvent (either the methanol or acetonitrile) as time at temperature increased. Figure 6 shows this solvent concentration in a pellet dried 48 h at 50°C in N_2 as a function of time at various temperatures. In all cases, the concentration of the solvent in the sample decreases with time at temperature.

DISCUSSION

For evaporation to take place from the top surface of a pressed ceramic pellet, the evaporated liquid must diffuse through both the porous network and the gas boundary layer to reach the bulk gas, as shown in the schematic diagram in Fig. 7. The nomenclature to be used in the analysis of this problem is incorporated into Fig. 7 and described in detail in the Appendix of this paper. The mass transfer flux resulting from the partial pressure profile shown in Fig. 7(*B*) is given by[11]

$$J = (1/K_c + x/D_e)^{-1}(P_l^s/RT^s - P_l^g/RT^g) \quad (1)$$

where K_c is the mass transfer coefficient for mass transfer in the boundary layer and D_e is the effective diffusion coefficient for vapor molecules in the porous network of a void fraction, ϵ, given by

$$D_e = (1/D_k + 1/D)^{-1}\epsilon/\xi \quad (2)$$

where D_k is the Knudsen[12] diffusion coefficient, D the molecular diffusion coefficient for vapor molecules through a stagnant drying gas, and ξ the tortuosity of the porous network (typically, $\xi \approx 2.0$).

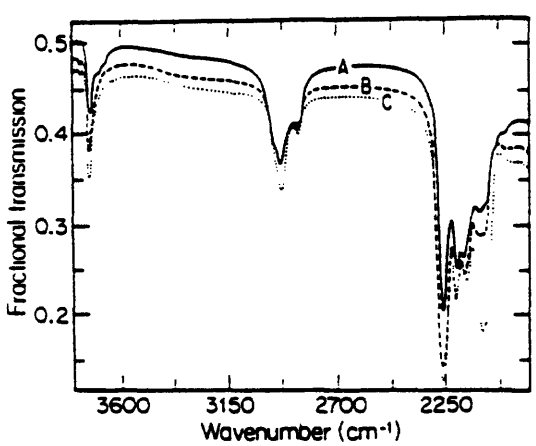

Fig. 5. Fourier transform ir spectrum of acetonitrile sample dried at 300°C for A, 0 min, B, 1 h, and C, 2 h.

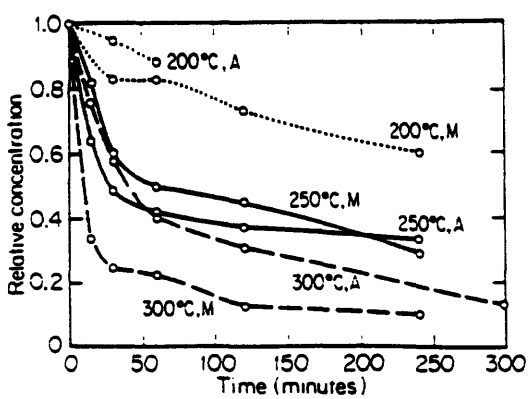

Fig. 6. Relative solvent concentration vs time at various temperatures. (A = acetonitrile; M = methanol)

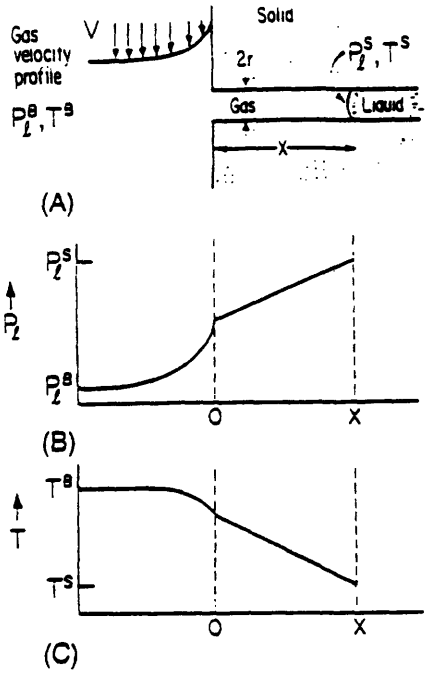

Fig. 7. Schematic diagram of evaporation in a porous network (*A*) geometry of pore and boundary layer (*B*) liquid partial pressure profile, and (*C*) temperature profile.

The partial pressure of the liquid at the surface, P_l^s, varies as a function of temperature according to the Clausius-Clapeyron[13] equation

$$P_l^s = P_0 \exp\left[\frac{\Delta H_{vap}}{R}\left(\frac{1}{T_0} - \frac{1}{T_s}\right)\right] \tag{3}$$

where ΔH_{vap} is the enthalpy of vaporization and P_0 is the vapor pressure at T_0. Usually T_0 is the normal boiling point, and P_0 is one atmosphere.

The mass transfer flux, J, (with units of moles per area per unit time) must be equivalent to the flux of molecules evaporated. The heat flux, q, required to evaporate this flux of molecules is

$$q = \Delta H_{vap} J \tag{4}$$

In general, the heat is transferred through the gas-boundary layer and through the porous network, as shown in the schematic diagram of the temperature profile in Fig. 7(*C*). The heat flux for this process is given by

$$q = (1/h + x/k_p)^{-1}(T^B - T^s) \tag{5}$$

where h is the heat transfer coefficient and k_p the effective thermal conductivity of the porous network, given by

$$k_p = [((1 - \epsilon)/ks) + (\epsilon/kg)]^{-1} \tag{6}$$

where k_s is the thermal conductivity of the solid and k_g the thermal conductivity of the gas in the pores. However, in our experiments thermal contact is made through the bottom of the pellet with the platform allowing us to assume a constant temperature for the pellet. Generally, this is not the case for drying ceramic green bodies. In general, at steady state both mass transfer flux and heat transfer flux are balanced according to Eq. (4), giving rise to a "wet bulb" temperature at the liquid interface inside the porous structure.

To determine the weight loss, dm/dt, in the sample, the rate liquid recedes in the pores, dx/dt, must be calculated from the overall mass transfer flux, J, as shown

$$dm/dt = -\epsilon\rho_l A\, dx/dt = -JAM_w^l \tag{7}$$

where A is the exposed surface area of the sample and ρ_l is the density of the liquid. Shaw[14] has shown that the liquid vapor interface in porous materials is fractally rough. Equation (7) assumes a liquid vapor interface that is smooth and located at the average location of the fractally rough interface.

The weight loss rate will depend on which step in the mass-transfer/heat-transfer sequence is the rate-determining step. For example, when mass transfer in the boundary layer is the rate-determining step, the time to dry the porous network to a liquid layer of x thickness is

$$t = \tau(x/x_0) \tag{8}$$

where x_0 is the thickness of the powder compact and τ the maximum time, given by

$$\tau = x_0\rho_l\epsilon/[M_w^l K_c(P_l^s/RT^s - P_l^B/RT^B)] \tag{9}$$

Assuming that the partial pressure of vapor of solvent in the bulk gas is essentially zero, then

$$\tau = x_0\rho_l\epsilon/[M_w^l K_c(P_l^s/RT^B)] \tag{10}$$

where P_l^s is calculated at the temperature T^B because heat transfer is fast.

If pore diffusion is the rate-limiting step, then the time to dry the porous network is given by

$$t = \tau(x/x_0)^2 \tag{11}$$

where the maximum time, τ, has a new definition:

$$\tau = x_0^2\rho_l\epsilon/[2M_w^l D_e(P_l^s/RT^B)] \tag{12}$$

If heat transfer in the boundary layer was the rate-determining step, then the time to dry the porous network is

$$t = \tau(x/x_0) \tag{13}$$

where the maximum time, τ, is defined as

$$\tau = \epsilon\rho_l x_0\Delta H_{vap}/[M_w^l h(T^B - T^s)] \tag{14}$$

If heat conduction in the pores was the rate-determining step, then the time to dry the porous network is

$$t = \tau(x/x_0)^2 \tag{15}$$

where the maximum time, τ, is defined as

$$\tau = \epsilon\rho_l x_0^2\Delta H_{vap}/[M_w^l k_p(T^B - T^s)] \tag{16}$$

Determining the maximum times for each of the possible rate-determining steps gives all of the possibilities for the actual rate-determining step. The longest maximum time is that of the actual rate-determining step for a given set of experimental conditions. When two or more maximum times are large and about equal, then both these steps are simultaneously rate-controlling (called mixed control). Under some conditions the rate-controlling step can change as drying proceeds. Mixed control during drying and changing from one rate-controlling step to another during drying will not be discussed further in this paper.

Once the rate-determining step has been determined, the weight loss can be calculated. If either boundary layer heat transfer or boundary layer mass transfer is the rate-determining step, then the weight loss is given by:

$$m(t) - m_0 = -\epsilon\rho_l A x_0 t/\tau \tag{17}$$

If either pore diffusion or pore heat conduction is the rate-determining step, then the weight loss is given by

$$m(t) - m_0 = -\epsilon\rho_l A x_0 \sqrt{t}/(\sqrt{\tau}) \tag{18}$$

In the last two equations, the appropriate expression for τ is used for the governing rate-determining step. These two weight loss expressions show either constant slope, when boundary layer heat or mass transfer is the rate-determining step, or $\sqrt{t}$ slope when pore diffusion or conduction is the rate-determining step.

To determine the rate-determining step, all of the τ values are calculated for the various drying steps. The largest τ value is that

of the slowest step, which is the rate-determining step.

Table I summarizes the calculated and observed τ values for the three investigated solvent systems. In all three cases, heat conduction through the pores has the lowest τ value and heat conduction through the boundary layer has the largest τ value. By establishing good thermal contact between the samples and the preheated pedestal, the rate-controlling process has been changed from boundary-layer heat transfer to one of the two mass transport steps. For free-standing silicon powder compacts, we would predict that boundary-layer heat transfer would be the rate-determining step.

For the octanol sample dried at 200°C with an N_2 gas velocity of 0.1 cm/s, we find that the largest τ value in Table I is 365 s for boundary-layer mass transport (neglecting boundary-layer heat transfer discussed earlier). This result suggests that the weight loss versus time curve should be linear and a log-log plot of the data should be linear with a slope of one. This behavior is observed in Fig. 2. The maximum drying time observed in Fig. 2 is ≈210 s, which is slightly smaller than the calculated τ value of 365 s for boundary-layer mass transport.

With the methanol sample dried at 80°C and an N_2 gas velocity of 1.3 cm/s, we find that the maximum τ value in Table I is 1295 s for pore diffusion. The higher gas velocity decreased the boundary-layer resistance and the thicker sample increased the pore-diffusion resistance. This behavior suggests that the weight loss versus time curve should have a $\sqrt{t}$ dependence, and a log-log plot of the data should be linear with a slope of 0.5. A linear log-log plot with a slope of 0.6 was observed in Fig. 3. The maximum drying time observed in Fig. 3 is 600 s, which is smaller than the maximum τ value. The reason that the τ value for pore diffusion is larger than the measured maximum drying time is probably due to the value used for the Knudsen diffusion coefficient. The pore radius used to calculate the Knudsen diffusion coefficient was estimated to be one tenth of the particle radius. To obtain agreement with theory, a pore radius two times larger should be used. A more accurate value of the Knudsen diffusion coefficient could be obtained if the pore size distribution was measured, but mercury porosimetry could not be used on these friable pellets.

For the acetonitrile sample dried at 27°C, we find that the largest τ value in Table I is 3140 s for boundary-layer mass transport. The combination of a near-zero gas velocity and a thin sample made the boundary-layer resistance dominate. This result suggests that the weight loss versus time curve should be linear and a log-log plot should be linear with a slope of one. This behavior is observed in Fig. 4. The maximum drying time observed in Fig. 4 is 7200 s, which is larger than the calculated τ value for boundary-layer mass transport. The reason that the maximum time is different than the τ value for boundary-layer mass transport is probably due to the value used for the mass transfer coefficient, which was calculated using the Colburn analogy[15] for natural convective mass transport from a sphere. To obtain agreement with experiment, the mass transfer coefficient should be a factor of two smaller than the one used. A more accurate mass transfer coefficient could not be calculated since the nitrogen gas velocity profile near the powder compact was not known in detail.

The FTIR results summarized in Fig. 6 show that adsorbed solvent concentrations decrease monotonically at rates that increase with increasing temperature. Within the time period investigated, the concentrations of neither acetonitrile nor methanol decreased to zero based on the 2925 cm^{-1} peak; the residual levels decreased with increasing temperature for both solvents. Analyzing these data to determine the desorption rate kinetics including the order of the desorption reaction and the rate constant at different temperatures was unsuccessful. The apparent orders of the desorption reactions varied from 1.9 to 6.0 for acetonitrile and 2.3 to 3.9 for methanol. Without a constant order for the desorption reactions for methnanol and acetonitrile, an Arrhenius plot cannot be made to determine the activation energy of the desorption reaction. These results demonstrate clearly that long exposure times at temperatures substantially above the solvent boiling point (*BP*) are required to completely dry high-purity, high-surface-area powders (BP acetonitrile 80°C, octanol 195°C and methanol 65°C). During this desorptive drying, very little gas (i.e. <1% of the liquid that occupied the pores) evolves from the powder compact. For this reason, cracking is not likely to be caused by gas evolution during desorptive drying of powder compacts.

Table I. τ Values for Various Rate-Determining Steps

	Time dependence	τ (s)
Figure 2, 200°C octanol		
Calculated		
Pore diffusion	$\sqrt{t}$	240
Boundary-layer mass transport	t	365
Pore conduction	$\sqrt{t}$	2.3
Boundary-layer heat transport	t	3050
Measured	t	210
Figure 3, 80°C methanol		
Calculated		
Pore diffusion	$\sqrt{t}$	1295
Boundary-layer mass transport	t	790
Pore conduction	$\sqrt{t}$	25
Boundary layer heat transport	t	45300
Measured	$t^{0.6}$	600
Figure 4, 27°C acetonitrile		
Calculated		
Pore diffusion	$\sqrt{t}$	2680
Boundary layer mass transport	t	3140
Pore conduction	$\sqrt{t}$	10
Boundary layer heat transport	t	3840
Measured	t	7200

CONCLUSIONS

Heat transfer in the pores was shown to be very fast compared to mass transfer. Heat transfer in the boundary layer was shown theoretically to be the slowest step. But because the powder compacts were placed on a platform through which heat was transferred, boundary-layer heat transfer was not important in these experiments. The drying of a thin silicon powder compact on a heat sink platform has been shown to be rate-limited by either boundary-layer mass transfer or pore diffusion. With boundary-layer mass transport, the weight loss versus time was linear, as predicted theoretically. With pore diffusion, the weight loss versus time was proportional to $t^{0.6}$. A $\sqrt{t}$ proportionality is predicted theoretically. The maximum times measured for the drying of these thin silicon powder compacts were of the same order of magnitude as those calculated from the τ value for the operative rate-determining step. More accurate values of τ can be obtained with better values of the mass-transfer coefficient and the Knudsen diffusion coefficient.

The removal of the last monolayer of adsorbed solvent requires temperatures well above the boiling point of the solvent. Higher and higher temperatures are required to remove more and more of the last monolayer. Some hydrolysis of the silicon powder surface was observed during extended heating at 250° to 300°C in nitrogen.

In drying other ceramic powder compacts that are not heat-sinked to a platform, all of the rate-determining steps are possible since the conductivity of the ceramic powder particles will be much lower than that of the silicon powder used here. To force a powder compact to dry at a faster rate, it is necessary to decrease the τ value for the rate-determining step. Equations listed in the text provide information on how to manipulate drying conditions to increase the drying rate for each rate-determining step. When the τ value for the operative rate-determining step has been decreased to below that of the second largest value, a new rate-determining step will be operable and require different changes in the drying conditions to further decrease the drying time.

To obtain dry ceramic bodies without cracks, it is necessary to dry the compacts gently. Exceeding the boiling point of the solvent before the pores are free of liquid is likely to cause cracks resulting from internal pressure gradients that will induce stress in

the compact, especially when mass transfer is the rate-determining step. Cracking was not observed in these experiments when drying for liquid removal was performed at temperatures slightly above the boiling point of the solvent. Higher temperatures are known to cause cracking[16] during liquid removal.

ACKNOWLEDGMENT

These and other contributions are gratefully acknowledged.

APPENDIX

NOMENCLATURE

A Surface area of compact exposed to gas,
D Diffusion coefficient ($_e$ effective, $_k$ Knudsen),
h Heat transfer coefficient,
ΔH_{vap} Enthalpy of vaporization,
J Flux of liquid molecules in gas,
K_c Mass transfer coefficient,
k Thermal conductivity ($_p$ effective for pores, $_s$ solid, $_g$ gas),
m Mass of powder compact ($_0$ at $t = 0$),
M^L_w Molecular weight of liquid,
P_l Partial pressure of the liquid (^{B} bulk, ^{s} liquid surface),
q Heat flux,
R Gas constant,
T Temperature,
t Time,
x Thickness of pores that are liquid-free ($_0$ at $t = \infty$),
ϵ Void fraction in powder compact (neglecting liquid),
ξ Tortuosity of pores (typically ≈ 2),
ρ_l Density of liquid, and
τ Maximum drying time for a particular rate-determining step.

REFERENCES

[1]H. H. Macy, "Clay-Water Relationships and the Internal Mechanism of Drying," *Trans. Br. Ceram. Soc.*, 41 [4] 73–121 (1942).
[2]R. Q. Packard, "Moisture Stress in Unfired Ceramic Clay Bodies," *J. Am. Ceram. Soc.*, 50 [5] 223–29 (1967).
[3]A. R. Cooper: Ch. 12 in Ceramics Processing Before Firing. Edited by G. Onoda and L. Hench. Wiley, New York, 1978.
[4]W. R. Cannon, S. C. Danforth, J. H. Flint, J. S. Haggerty, and R. A. Marra, "Sinterable Ceramic Powders from Laser Driven Reactions: Part I. Process Description and Modeling," *J. Am. Ceram. Soc.*, 65 [7] 324–30 (1982).
[5]W. R. Cannon, S. C. Danforth, J. H. Flint, J. S. Haggerty, and R. A. Marra, "Sinterable Ceramic Powders from Laser Driven Reactions: Part II. Powder Characteristics and Process Variables," *ibid.*, 330–35.
[6]J. S. Haggerty, G. Garvey, J-M. Lihrmann, and J. E. Ritter, "Processing and Properties of Reaction Bonded Silicon Nitride made from Laser Synthesized Silicon Powders"; in Defect Properties and Processing of High-Technology Materials. Edited by Y. Chen, W. D. Kingery, and R. J. Stokes. Proceedings of the Materials Research Society, 1986.
[7]T. Kramer, W. Rhine, and H. K. Bowen, "Oxidation of Laser Synthesized Silicon"; unpublished work.
[8]G. Socrates, Infrared Characteristic Group Frequencies, Wiley-Interscience, 1980; p. 256.
[9]D. N. Kendall, Applied Infrared Spectroscopy, Rheinhold, 1966; p. 352.
[10]Grum, Franc, and Bartleson, p. 303 in Optical Radiation Measurements, Vol. 2, Academic, 1980.
[11]R. Jackson, p. 354 in Chemical Engineering Monographs, Vol. 4, Elsevier, 1972.
[12]M. Knudsen, The Kinetic theory of Gasses, Methuen, London, 1934.
[13]G. W. Castellan, Physical Chemistry, Addison-Wesley, Reading, MA, 1964; p. 219.
[14]T. Shaw, pp. 215–24 in Better Ceramics Through Chemistry II, Vol. 73. Edited by C. J. Brinker, E. E. Clark, and D. R. Ulrich, MRS, 1986.
[15]T. H. Chilton and A. P. Colburn, "Analogy Between Heat and Mass Transfer," *Ind. Eng. Chem.*, 26, 1183 (1934).
[16]H. K. Bowen; unpublished work.

To be published in the Proceedings of the First International Conference on Ceramic Powder Processing Science, Orlando, Florida, November 1-4, 1987, to be published by the American Ceramic Society P87-09

PROCESSING AND PROPERTIES OF REACTION BONDED SILICON NITRIDE AND SINTERED SILICON CARBIDE MADE FROM LASER SYNTHESIZED POWDERS

J.S.Haggerty, G.J.Garvey*, J.H.Flint, B.W.Sheldon, M.Aoki**, and M.Okuyama***
Massachusetts Institute of Technology
Cambridge, Massachusetts 02139

J.E.Ritter and S.V.Nair
University of Massachusetts
Amherst, MA 01003

INTRODUCTION

The properties of Si_3N_4 and SiC achieve high values only if pressure and/or sintering aids are employed during consolidation, usually at the expense of increased cost, restricted maximum size and complexity of finished parts, and degraded high-temperature mechanical properties. Also, remaining bulk flaws have caused excessive variation in their properties. This processing research program was initiated for these reasons. Our strategy was based on producing flaw-free green parts made directly from high-purity, small diameter powders.

POWDER SYNTHESIS

A new synthesis process was developed[1,2] to produce small, high purity, non-agglomerated powders of Si and SiC since they were not available. The laser heated gas phase synthesis process was selected because very high quality powder can be produced and commercial-scale manufacturing costs[3] can be as low as $1.50-$2.00/kg plus the reactant costs.

The ceramic powders are synthesized by rapidly heating a reactant gas stream with a CW CO_2 laser until particles form and grow.[4] Silane (SiH_4) is used to make Si powders and SiH_4 mixed with methane (CH_4) or ethylene (C_2H_4) is used to make SiC.[5]

The powder characteristics are controlled by the cell pressure, the reactants, their flow rates and flow ratios, the laser power and intensity, and cell geometry primarily through their influence on the temperature distribution within the reaction zone. The effects of these have been investigated experimentally and mathematically.[6,7] The details of these modeling studies are presented elsewhere in this Proceedings.[8]

---

* Present Address, ABEX Corporation, Research Center, Mahwah, NJ
** Present Address, Toa Nenryo Kogyo, Tokyo, Japan
*** Present Address, NGK Spark Plug, Nagoya, Japan

Table 1. Powder Properties

Powder Designation	F28S	F45S/F55S	L6SC	L30SC-B
Material	Si	Si	SiC	B-doped SiC
Max Temp. (°C)	1455	1605	1830	1920
Pressure (10^5 Pa)	1.3	1.3/1.6	1.3	2.0
D (mass)(nm)	262	305	90	95
σ_g (number)	2.6	1.8	1.7	1.7
σ_g (mass)	1.5	1.5	1.4	1.4
Packing Density(%)	59	63	63	63

Resulting powders are small (< 500 nm) and equiaxed, contain few agglomerates, have very high purity (< 200 ppm oxygen), and for SiC have controlled Si:C ratios. The combination of small size and freedom from agglomeration allows the powders to be formed into dense, virtually flaw-free green bodies with extremely small pores. Table 1 summarizes the physical characteristics and green packing densities of the Si and SiC powders used to make the superior reaction bonded silicon nitride (RBSN) and sintered SiC (SSC). The mean size (D) and geometric standard size distributions (σ_g) are determined from TEM [7,8].

High quality Si powders are formed by the collision and coalescence of liquid Si droplets.[7,8,9] The number density of particles and collision frequency decrease rapidly from initial values as inelastic collisions result in particle growth. Once the particles solidify and cool substantially below 1410°C, collisions between the relatively large particles become elastic. The particle size and morphology distributions are directly attributable to the temperature and velocity distributions in the reaction zone.[10,11] Uniform powder is produced only when all flow streams experience similar time-temperature-concentration histories.

High quality SiC is formed from premixed streams of SiH_4 and CH_4 via a two step reaction mechanism.[5] The reactant gas mixture is heated until Si particles start to grow by collisions and coalescence in a H_2/CH_4 atmosphere. As the temperature of the particle-methane-hydrogen mixture continues to increase, two bands appear in the reaction zone. Si particles form and grow in the lower band and carburization occurs in the upper band. Evidently the onset of the carburization reaction terminates the particle growth process.

POWDER PROCESSING

Test parts were made to determine whether using laser synthesized particles resulted in superior consolidation kinetics and properties. Our objective was to form high purity, defect-free unfired bodies having constituent particles arranged with random close packed[12] rather than ordered close packed structures.[13] Parts were made from dispersions by colloidal (filter) pressing and centrifugal casting. Dispersing media were selected based on maximizing dispersion stability and drying kinetics while minimizing contaminating residuals and destructive effluents.

Powder Dispersion

Suitable dispersion systems were identified by empirical observation[14,15] and by matching solvent/dispersant systems to measured powder surface characteristics based on theoretical selection criteria.

The theoretical approach to obtain steric stability was based on Fowkes'[16] technique. This procedure requires the determination of the Lewis acid/base characteristics of the powder surfaces and the calculation of the interactional energies with candidate molecules using the E and C values tabulated by Drago.[17] Anchor, solvent and stabilizing moiety are selected based on these values and necessary energy balances.

Empirically, stability was evaluated by light-scattering, photon correlation spectroscopy (PCS), sedimentation rate, sediment density, and microelectrophoretic mobility. Pure solvents that were empirically screened[14,15] included alcohols, amines, amides, aldehydes, aromatic and aliphatic hydrocarbons, carboxylic acids, ethers and ketones. Dispersants examined included alcohols, amines, amides, carboxylic acids, fluoronated alkyls, silazanes and succinimides, each in hexane, toluene, alcohol and acetonitrile solvents. Well dispersed systems had PCS diameters only slightly larger than TEM diameters; they also had higher turbidities, higher centrifugally cast densities, lower sedimentation rates and higher microelectrophoretic mobilities than poorly dispersed systems.

Based on these results, alcohols performed best for both Si and SiC powders. Methanol was selected from among the alcohols for Si due to its low viscosity and high vapor pressure. Octyl alcohol was selected for the SiC powder because it also provided a steric barrier. Optimized ultrasonic exposures[18] were used to avoid ultrasonic induced agglomeration.

Shaping

Test parts were formed by colloidal pressing. In this technique, the solvent is extracted from the slip through membrane filters supported by porous frits that are loaded by ported pistons in a die. Unidirectional pressing was adopted because laminate flaws formed along the midplanes of bidirectionally pressed compacts.[19]

Colloidal pressing times and pressures were varied to determine their effects on green density, flaws and yield. Time had little effect. The reciprocal of the fractional green density was found to vary linearly with the log of pressing pressure implying[20] a single rearrangement mechanism. The yield of good Si parts dropped sharply from 100% for pressures in excess of 69 MPa. This is not the case for SiC parts which exhibited a constant yield of 100% for all pressing pressures investigated up to 280 MPa. After colloidal pressing, the high density Si compacts used in the mechanical testing study were cold isostatically pressed at a pressure of 280 MPa. Inclusion of even a low percentage of aggregates lowered the cake densities to less than 50% of theoretical.[19,21,22] The achieved densities of ~63% correspond to that of a random close packed structure.[12]

Drying

After pressing, the pellets were dried to avoid damage during firing. Drying and desorbtion rates were modeled[23] using TGA and FTIR techniques. The rate controlling transport step was vapor diffusion through either the boundary layer or the pores; without heat-sinking, the rate controlling

mechanism is heat transfer through the boundary layer. Adsorbed species are not removed until temperatures ~200°C above the solvents' boiling points are reached. Drying was accomplished with a 24 hour soak in a 200°C N_2 atmosphere after an 8 hour linear ramp.

Silicon Nitriding

Samples used for mechanical testing were made[19,22] from dried Si pellets nitrided without exposure to air in a top loading, cold-wall, vertical axis, tungsten furnace installed inside an Ar atmosphere glove box (<10 ppm O_2 & H_2O combined). Complete nitridation was achieved by heating at 1°C/min up to 1420°C, followed by a 1 hour hold. Studies of the nitriding kinetics and rate controlling mechanisms show[24] that laser synthesized Si parts can be completely nitrided at lower temperatures in shorter times (1150°C, 1h; 1250°C, 10m).

X-ray analysis[22] showed 80-90% α-Si_3N_4 and the balance β-Si_3N_4; no unreacted Si was detected. X-ray line broadening showed nitride crystal sizes of 28 nm for α ($2\theta = 30.8°$) and 33 nm for β ($2\theta = 33.7°$). Hg porosimetry pore neck radii were between 5 and 30 nm. The nitride phase, shown in the SEM fracture surface in Figure 1, is a continuous network with characteristic solid phase dimensions between 0.2 and 0.7 μm; this nominally agrees with both the RBSN BET equivalent size (~0.24 μm) and the initial Si particle size. Observed pore radii (50-125 nm) exceed the interpore neck dimensions measured by Hg porosimetry. Micrographs of fracture surfaces frequently revealed 5-15 μm diameter isolated voids. These microstructural features are very different from those typically observed in RBSN.[25]

Silicon Carbide Sintering

SiC pellets were made from B doped SiC powder using the procedures described in previous sections. The powder used was a L30SC type (Table 1) to which approximately 0.5% by weight B was introduced during synthesis using B_2H_6 added to the reactant gas stream. The B_2H_6 had no effect on any powder or pellet characteristic. Dried samples were fired at temperatures ranging

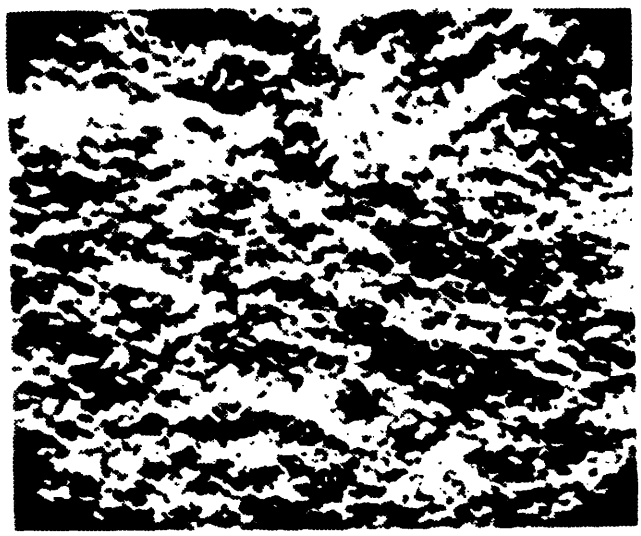

1 Micron

Figure 1. Fracture surface of RBSN made with laser-synthesized Si powder.

Table 2. Characteristics of Sintered SiC

Sintering Temp. (°C)	1800	1900	1950	2000	2050	2100
Density (%)	65.8	81.0	89.1	93.2	97.5	90.2
Pore Diameter (nm)	--	9	3.7	--	53	73.5
Grain Size (μm)	--	0.3	0.25 and 0.5 x 2.0	--	1.2 x 20	100
Tensile Strength (MPa)	--	--	--	--	645 ± 60	--
Vickers Hardness (GPa)	--	--	--	--	23.8 ± 3.1	--

from 1800°C to 2100°C in a graphite tube furnace in an Ar atmosphere. The heating cycle consisted of a 50°C/h ramp to the firing temperature, a 1 h soak and a furnace quench (50-100°C/h).

The densities of the sintered samples were determined by measuring and weighing, by immersion in water and by microstructural analysis; Table 2 lists the averages of these results. The densities increased with increasing sintering temperature up to 2050°C. An Arrhenius plot of the linear shrinkage reveals an apparent activation energy of ~120 kcal/mole, consistent with reported values for carbon diffusion through SiC grain boundaries.[26] The lower density of the 2100°C samples may result in part from measurement inaccuracies; these pellets included atypical porous regions near their surfaces, and also contained pull-outs that were counted as pores.

The sintered SiC remained 100% β phase up to a sintering temperature of 2050°C. The 2100°C samples contained approximately equal fractions of α and β phases. The grain size and morphology changed continuously with increasing firing temperature. Although many 0.1-0.15 μm grains were present in the 1900°C sample, the average grain size had already increased to 0.3 μm from 0.095 μm, the average size of the starting powder. At 1950°C, considerable coalescence of the particles into elongated grains occurred, with some individual, small equiaxial grains remaining. The sample sintered at 2050°C was made up completely of high aspect-ratio cylindrical β grains approximately

10 Microns

Figure 2. Optical photomicrograph of B doped sample sintered at 2050°C.

1.2 μm in diameter and 20 μm long (Figure 2). Pores were confined to grain boundaries. At 2100°C, equiaxed grains had grown to 100 μm, and pores were uniformly distributed throughout the grains.

PROPERTY MEASUREMENT

A ball-on-ring biaxial strength test[27,28] was used to determine the room temperature strengths of the nitrided and sintered samples to eliminate spurious edge effects. This test and the 4-point MIL-STD-1942(MR) test gave average strengths within 1 standard deviation for samples taken from a hot pressed Si_3N_4 billet donated by the Norton Co.[29] Hardness and fracture toughness were measured using a Vickers indenter. Oxidation resistance of the RBSN was measured with elevated temperature air exposures.

Figure 3 summarizes the results of strength measurements with two types of RBSN samples. An average of 544 ± 80 MPa (Max = 676 MPa) was observed for a group of 75% dense RBSN samples made using optimized procedures from an unclassified Si powder (F55S) and an average of 250 MPa (Max = 460 MPa) for 65% dense samples made from an earlier classified powder[19]. Figure 3 also includes three different lines representing least-square fits of exponential functions to RBSN, SSN and HPSN strength data reported in the literature[19,25,30] for laboratory and commercial samples with various surface finishes.

Laser-originating RBSN specimens exhibit average strengths that are 2.5 to 5.0 times the average reported values at both corresponding density levels. After eliminating initially observed processing flaws, both groups of RBSN samples exhibited strengths normally associated with sintered or hot pressed α-Si_3N_4. Fracture sources were usually either 5-15 μm diameter voids or preexisting lenticular cracks less than 50 μm deep perpendicular to the stress axis. Application of the Griffith equation[31] to the observed strengths yields flaw sizes of 4 to 16 μm.

The results of the strength measurements with the 2050°C SiC samples are included in Table 2. Although the samples are far from optimal, the observed average strength, 645 ± 60 MPa (max = 761 MPa), is approximately twice the strength levels normally observed for sintered SiC[32] and is more typical of hot pressed or HIPed SiC. The only other group that has reported SSC strength levels in this range[33] also employed SiH_4 based synthesis chemistries and similar anhydrous, anaerobic post-synthesis handling procedures.

Vickers hardness values were determined on polished surfaces using 300 and 500 gram loads. Observed values for RBSN (Figure 4) ranged from 3.5 to 11.0 GPa. The hardness of 77% dense RBSN (~10 GPa) is higher than that of 85% dense, highly optimized commercial RBSN (~8.3 GPa).[21] Using the indentation technique,[34] our dense specimens exhibited an average K_{IC} value of 2.8 MPa $m^{1/2}$ (Figure 4). These are higher than is characteristic of the optimized commercial RBSN (~2.0 MPa $m^{1/2}$)[21] and approach those of sintered α-Si_3N_4.

For SiC, the observed hardness values of 23.8 GPa are also more typical of hot pressed than sintered SiC. The hardness and strength values are presumably coupled, although there is no formal theory to relate the two properties in a brittle material as exists for ductile materials. Fracture toughness values could not be measured on the SiC using the indentation technique because stable cracks did not form.

The oxidation resistance of laser-originating RBSN at 1250°C in flowing air is strongly dependent on the porosity level and pore size. As predicted by Thümmler's[35] results at the same temperature, low density specimens undergo significant internal oxidation before saturation is attained. For densities >85% and Hg porosimetry pore radii < 60 nm, Thümmler showed that internal

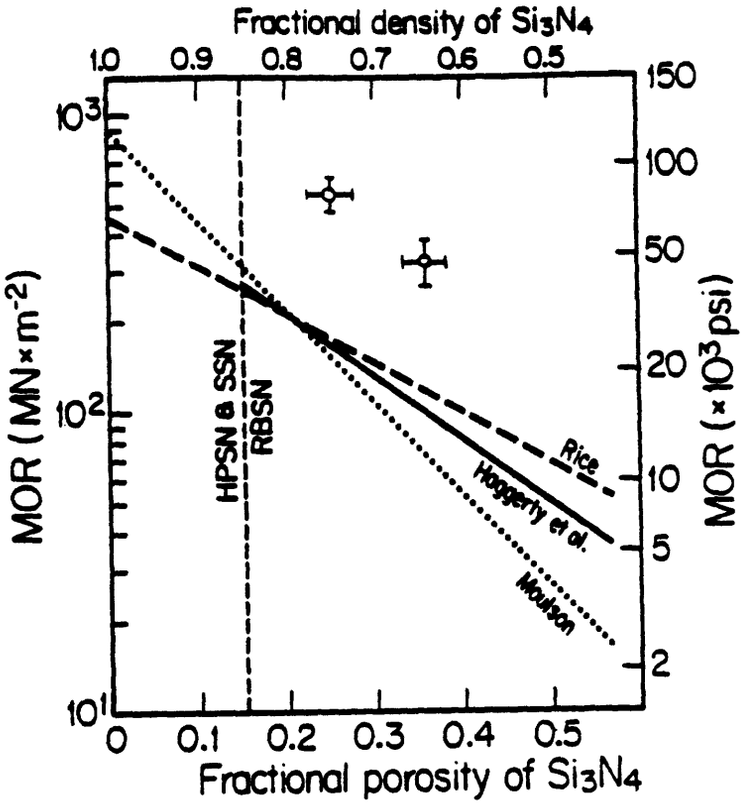

Figure 3. Room temperature strength of silicon nitride vs. density.

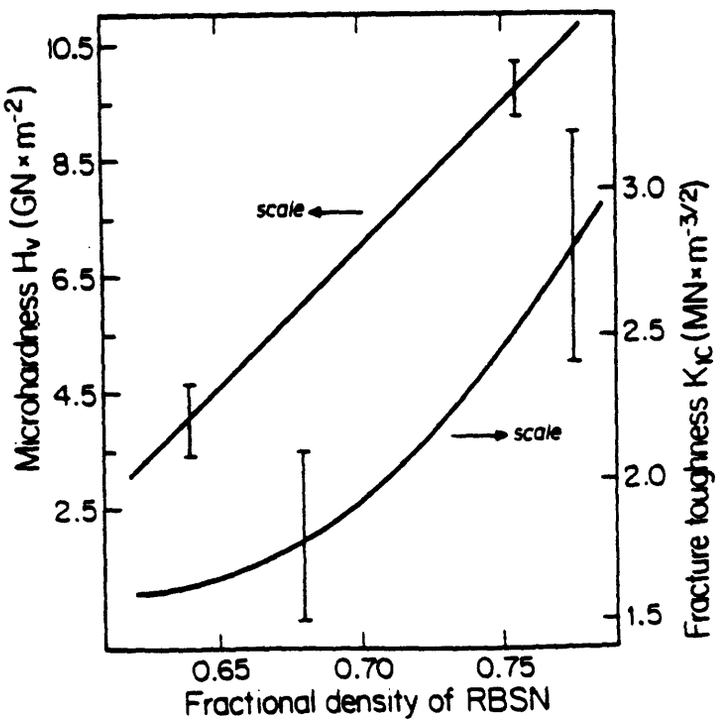

Figure 4. Hardness and fracture toughness of laser-originating RBSN vs. density. Error bars are typical.

oxidation would be reduced to less than 1% due to pore closure by the oxide product. For laser-originating RBSN, the extent of oxidation was less than 1% for specimens having densities as low as 74%. This superior performance at lower densities very likely results from our samples having smaller pore diameters and more uniform microstructures. The superior properties result from uniformly distributed, small diameter pores made possible from the combination of ideal powders and careful post-synthesis processing techniques.

CONCLUSIONS

This research program achieved its principal technical objective; superior consolidation kinetics and properties can result if powders having very specific characteristics are employed in combination with careful post-synthesis handling procedures. Failure to meet specific requirements in either area will cause adverse effects.

Generally, the required powder characteristics are the same as were postulated. Powders must be small, equiaxed, uniform in size, pure, and free of agglomerates. Of these criteria, freedom from agglomerates is the most important because agglomerates lower the achievable green density to unacceptably low levels and introduce large, localized defects.

The post-synthesis handling and processing procedures are also subject to many constraints. Cleanliness is critical if high strengths are to be realized. Exposure to O_2 or H_2O can degrade high temperature mechanical properties and consolidation/nitriding kinetics through introduction of internal oxides. Equally important, these exposures cause the surface chemistries to change so that dispersion systems no longer satisfy the requirements needed to form defect-free, high density green parts.

Obtaining nearly complete nitridation in less than 10 minutes at only 1250°C is remarkable compared to the multi-day nitriding schedules and higher temperatures that are typically used to produce RBSN; the solvent exposed samples react slower, but comparatively these rates are still very fast. The enhanced reactivity is attributable to the high purity and small particle sizes of the powders used. Equally rapid nitriding should be possible for colloidally pressed samples once the effects of the solvent on the nitriding mechanism are fully explained.

Even without many iterations of the processing variable-microstructure-property approach used in this research, we have achieved property levels that were considered unreachable with RBSN and unusual with sintered SiC. The properties of both are typical of hot pressed materials. These improvements resulted directly from our ability to make parts in which residual porosity was distributed uniformly in minimum size pores.

ACKNOWLEDGMENTS

Numerous staff and students have contributed to this work. Hopefully, all are properly referenced. This research was principally sponsored by DOD (DARPA, ONR, and ARO) and an industrial consortium including Abex Corp., Aisin Seiki Co., Alcoa, NGK Spark Plug Co., Nippon Steel, Sumitomo Electric Industries, Ltd., The Japan Steel Works, Ltd., and Toa Nenryo Kogyo K.K.. Specific topics were supported by NASA-Lewis, DOE and a second industrial consortium made up of Caterpillar Tractor, Cummins Engine Co., Deere, Inc., General Motors Corp., TRW Valve Division and Rhone Poulenc. All contributions are gratefully acknowledged.

REFERENCES

1. Cannon, W. R., Danforth, S. C., Flint, J. H., Haggerty, J. S., Marra, R. A., "Sinterable Ceramic Powders from Laser Driven Reactions, Part I; Process Description and Modeling," J. Am. Ceram. Soc., 65 [7], 324-30 (1982).
2. Cannon, W. R., Danforth, S. C., Haggerty, J. S., Marra, R.A., "Sinterable Ceramic Powders from Laser Driven Reactions, Part II; Powder Characteristics and Process Variables," J. Am. Ceram. Soc., 65 [7], 330-5 (1982).
3. Flint, J. H. and Haggerty, J. S., "Ceramic Powders from Laser Driven Reactions," Applications of Lasers to Industrial Chemistry, SPIE, Vol. 458, 1984.
4. Flint, J. H., Marra, R. A. and Haggerty, J. S., "Powder Temperature, Size, and Number Density in Laser Driven Reactions," Aerosol Sci. and Tech., 5, 249-261 (1986).
5. Sawano, K., Haggerty, J. S. and Bowen, H. K., "Formation of SiC Powder from Laser Heated Vapor Phase Reactions," Yogyo-Kyokai-Shi (J. of Ceram. Soc. Japan), 95 [1], 64-9 (1987).
6. Akmandor, I. S., "Theoretical and Computational Models of Reacting Silane Gas Flows: Laser Driven Pyrolysis of Subsonic and Supersonic Jets," Ph.D. Thesis, MIT, 1985.
7. Flint, J. H. and Haggerty, J.S., "A Model for the Growth of Silicon Particles from Laser-Heated Gases," submitted to Aerosol Science and Technology.
8. Flint, J.H. and Haggerty, J.S., "Models For Synthesis of Ceramic Powders by Vapor Phase Reactions", to be published in Proceedings of the First International Conference on Ceramic Powders Processing Science, Orlando, FL, Nov 1987.
9. Coltrin, M. E., Kee, R. J. and Miller, J. A., "A Mathematical Model of the Coupled Fluid Mechanics and Chemical Kinetics in a Chemical Vapor Deposition Reactor," J. El. Chem. Soc., 131, 425-434 (1984).
10. Lee, K. W., Chen, H. and Gieseke, J. A., "Log-Normally Preserving Size Distribution for Brownian Coagultion in the Free-Molecule Regime," Aerosol Sci. and Tech., 3, 53-62 (1984).
11. Ulrich, G. D. and Subramanian, N. S., "Particle Growth in Flames, III. Coalescence as a Rate-Controlling Process," Combustion Sciences and Technology, 17, 210-26 (1977).
12. Bernal, J. D., "Packing of Spheres," Nature, 188, 908 (1960).
13. Barringer, E. A. and Bowen, H. K., "Ceramic Powder Processing," Ceram. Eng. Sci. Proc., 5, 285-97 (1984).
14. Mizuta, S., Cannon, W. R., Bleier, A. and Haggerty, J. S., "Wetting and Dispersion of Silicon Powder Without Deflocculants," Am. Cer. Soc. Bull., 61, 872-75 (1982).
15. Okuyama, M., Garvey, G.J., Ring, T.A., and Haggerty, J.S., "Dispersion of SiC Powders in Non-Aqueous Solvents", submitted to J. Am. Ceram. Soc.
16. Fowkes, F. M., "Acid-Base Contributions to Polymer-Filler Interactions," Rubber Chemistry and Technology, 57, 328-384 (1984).
17. Drago, D. S., Vogel, G. C. and Needham, T. E., "A Four-Parameter Equation for Predicting Enthalpies of Adduct Formation," J. Amer. Chem. Soc., 93:23, Nov. 17, 1971, pp. 6014-26.
18. Aoki, M., Ring, T. A. and Haggerty, J. S., "Analysis and Modeling of the Ultrasonic Dispersing Technique," Adv. Ceram. Mat., Vol. 2, No. 3A, 1987.

19. Haggerty, J. S., Garvey, G., Lihrmann, J-M, and Ritter, J. E., "Processing and Properties of Reaction Bonded Silicon Nitride made from Laser Synthesized Silicon Powders," Defect Properties and Processing of High-Technology Nonmetallic Materials, Materials Research Society Symposia Proceedings, Vol. 60, Pittsburgh, PA, 1986, pp. 51-62.
20. Whittemore Jr., O. J., in Ceramic Processing Before Firing, G. Y. Onoda and L. L. Hench, J. Wiley & Sons, NY, 1978, 350.
21. Danforth, S. C. and Haggerty, J. S., "Mechanical Properties of Sintered and Nitrided Laser Synthesized Silicon Powder," J. Am. Ceram. Soc., 66 [4], 273-5 (1983).
22. Haggerty, J. S., Flint, J. H., Garvey, G., Lihrmann, J-M. and Ritter, J. E., "High Strength, Oxidation Resistant Reaction Bonded Silicon Nitride from Laser-Synthesized Silicon Powder," Proceedings of the Second International Symposium Ceramic Materials and Components for Engines, Lübeck-Travemünde, Federal Republic of Germany, Deutsche Keramische Gesellschaft, 147-154, April 1986.
23. Castro, D., Ring, T. A. and Haggerty, J. S., "Drying of Silicon Powder Compacts", submitted for publication to Am. Ceram. Soc.
24. Sheldon, B.W. and Haggerty, J.S., "The Nitridation of High Purity, Laser-Synthesized Silicon Powder to Form Reaction Bonded Silicon Nitride", to be published in the Proceedings of the 12th Annual Conference on Composites and Advanced Ceramics, Cocoa Beach, FL, 1988.
25. Moulson, A. J., "Reaction-bonded silicon nitride: its Formation and Properties," J. Mat. Sci., 14, 1017-1051 (1979).
26. Thümmler, F., "Sintering and High Temperature Properties of Si_3N_4 and SiC," in Sintering Processes, G. C. Kuczynski (ed.), Plenum Press, New York, NY, 1980.
27. Wachtman Jr., J. B., Capps, W. and Mandel, J., "Biaxial Flexure Tests of Ceramic Substrates," J. of Mat. 7[2], 188 (1972).
28. Shelty, D. K., Rosenfield, A. R., McGuire, P., Bansal, G. K. and Duckworth, W. H., "Biaxial Flexure Tests for Ceramics," Am. Ceram. Soc. Bull., 59[12], 1193 (1980).
29. Dr. Joseph Patchett, Norton Co., Niagara Falls, Ontario, Canada, private communication.
30. Rice, R. W., "Comment on 'Additional observations on the strength / nitrided density relationship for a reaction sintered silicon nitride,'" J. Mat. Sci., 12[7], L627 (1977).
31. Smith, F. W., Emergy, A. F. and Kobayashi, A. S., "Stress Intensity Factors for Penny-Shaped Cracks Part II: Semi-Infinite Solid," J. Appl. Mech., 34, Series E, 953-959 (1976).
32. Dudda, S., "Densification and Properties of α-Silicon Carbide," J. Am. Ceram. Soc., 68, C-269 (1985).
33. Saiki, G. and Kondo, J., "Synthesis and Sintering of B-Doped SiC Powders by Plasma Arc Method", Paper 16-BP-86 presented at the Annual Meeting of the American Ceramic Society, March 1986.
34. Anstis, G. R., Chantikui, P., Lawn, B. R. and Marshall, D. B., "A Critical Evaluation of Indentation Techniques for Measuring Fracture Toughness: I, Direct Crack Measurements," J. Am. Ceram. Soc., 64[9], 533 (1981).
35. Porz, F. and Thümmler, F., "Oxidation Mechanism of Porous Silicon Nitride," J. Mat. Sci., 19, 1203-95 (1984).

MRS Symposium on Defect Properties and Processing of High-Technology Nonmetallic Materials, December 2-4, 1985, Boston, Massachusetts P85-05

PROCESSING AND PROPERTIES OF REACTION BONDED SILICON NITRIDE MADE FROM LASER SYNTHESIZED SILICON POWDERS

*J.S. HAGGERTY, *G. GARVEY, *J-M. LIHRMANN AND J.E. RITTER**
*Massachusetts Institute of Technology, Cambridge, MA 02139
**University of Massachusetts, Amherst, MA 01003

ABSTRACT

Laser synthesized silicon powders have been used to make reaction bonded silicon nitride samples. Maximum hardness (11.3 GNm^{-2}), fracture toughness (3.6 $MNm^{-3/2}$), pore size (Hg porosimetry 50-300Å radius) and strength (~460 MNm^{-2}) values reflect the superior microstructures that are observed. With anaerobic anhydrous processing, these powders nitride to completion in less than 7 hours at 1400°C.

I. INTRODUCTION

Reaction bonded silicon nitride (RBSN) is one of the candidate ceramic materials for applications where thermal shock, high temperature strength and moderate oxidation resistance at temperatures up to ~1370°C are desired. Most RBSN properties are approximately equal to those of hot pressed and sintered silicon nitride (HPSN and SSN respectively). Room temperature strengths of RBSN are lower than those of HPSN and SSN [1] because of residual porosity levels; however, high temperature strengths can exceed those of HPSN and SSN since sintering aids generally are not employed in RBSN. One very important characteristic results from the nitride forming within the pore structure of the Si powder; parts are made with minimal changes from their as-formed dimensions.

Our interest in RBSN stemmed from the combination of these factors and recent evidence that the achievement of superior microstructures would simultaneously permit both improved oxidation resistance [2] and strengths. The required small pore dimensions and high, uniform densities appeared feasible with the Si powders produced by the laser synthesis process.

II. RBSN PROCESSING STEPS

Reaction bonded silicon nitride is made by nitriding previously shaped, low density parts made of Si powders. The processing steps generally employed are shown in Figure 1. Each processing step, from Si powder synthesis to final nitriding, can detrimentally affect properties of the parts if not properly controlled. The processing conditions used in this research were done in a manner that minimized contamination and insured complete reaction of the Si powders. Although the reported nitriding kinetics are already much faster than normal, they should not be viewed as optimized.

The silicon powders were processed entirely without direct exposure to air or water. Anaerobic, anhydrous processing avoided spurious nitriding kinetics resulting from the presence of oxygen, forced the development of new dispersion techniques and should yield improved high temperature mechanical properties. Each of the employed processing steps is discussed with the exception of the post-synthesis Si powder handling and the drying of pressed parts. Currently, both are the subjects of detailed studies. Empirically, we established that storage and handling in an Ar (<10 ppm O_2 and <3 ppm H_2O) atmosphere yielded Si parts which nitrided reproducibly in

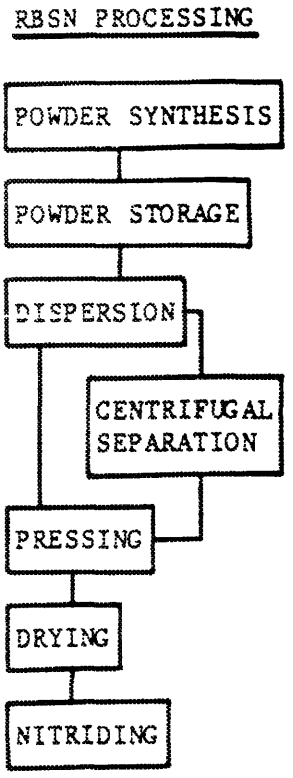

Fig. 1. Processing steps used to make RBSN

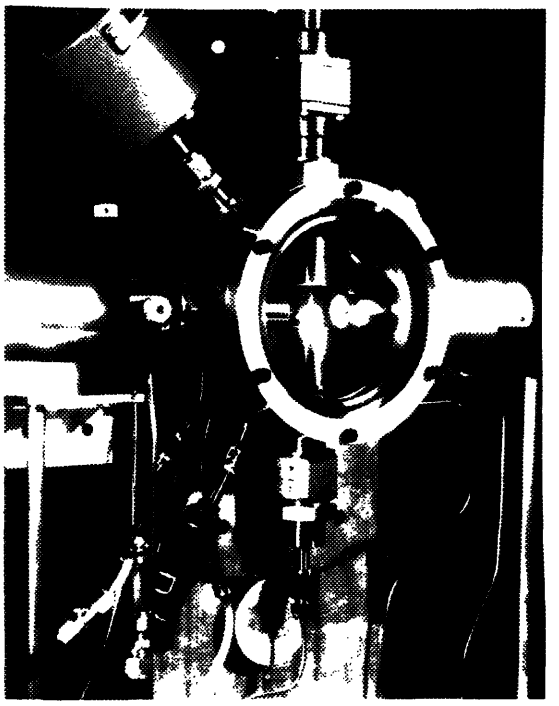

Fig. 2. Reaction cell used to synthesize Si powder from laser heated SiH_4

N_2, and that drying for one week at 27°C in Ar followed by heating to 180° over a period of 24 hours produced parts for which no further weight losses were evident. These procedures were used throughout this research.

A. Powder Synthesis

The Si powders were synthesized by the pyrolysis of CO_2 laser heated SiH_4 gas. The equipment, the process modelling and most powder characteristics have been reported previously [3,4,5]. This process was developed to produce powders having small diameters, spherical shapes, uniform diameter distributions, freedom of aggregates and high purity. Using powders with these characteristics, we anticipated that it should be possible to produce unfired parts with the highly perfect microstructures needed to achieve improved oxidation resistance and strengths.

Achievement of these powder characteristics resulted from inducing unusual and uniform time-temperature excursions for both the premixed reactants and the reaction products. Using the reaction cell shown in Figure 2 in conjunction with a 325 watt CW-CO_2 laser, reactant gas heating rates between 10^6 to 10^8°C/sec, reaction times of ~10^{-3}sec and product cooling rates of ~10^5°C are achieved. Compositional control is achieved with mass flow meters and by the relative velocities of the reactant and annular gas streams. Maximum temperature levels can be controlled to $\pm$ 20°C. These process conditions permit nucleation, growth and coalescense processes to be controlled in a manner that yields powders having the desired characteristics in high particle number density gas streams. High purities are achieved during synthesis in the hermetic, cold wall reaction vessel and are maintained by transporting the powders to a glove box under a positive Ar pressure.

B. Powder Dispersion

Our objective was to disperse and compact silicon particles in a manner that would permit defect free, high coordination number green bodies to be formed; at least random close packed structures [7] were sought. This must be effected without incorporating contaminates that will hamper nitridation, densification, or degrade high temperature strength. The criteria for selecting a dispersing medium for silicon were based on dispersion stability, oxidation, drying kinetics, residues and the absence of destructive effluent generation. The pure solvents and dispersant-solvent systems examined are summarized in Table III. Stability was evaluated by light-scattering, photon correlation spectroscopy (PCS), sedimentation rate, sediment density, and microelectrophoretic mobility.

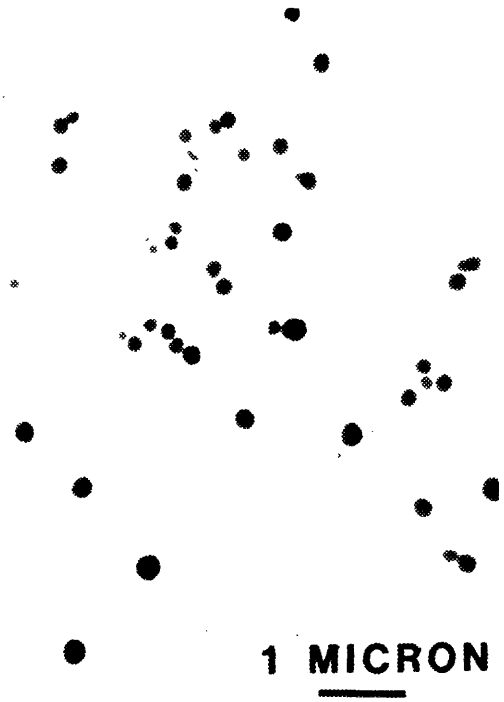

Fig. 3. TEM photomicrograph of dispersed Si powder type F-055.

TABLE III. INVESTIGATED DISPERSANT SYSTEMS

Pure Solvents	Dispersants
Alcohols	Alcohols
Aldehydes	Alkylated Chlorosilanes
Aliphatic Hydrocarbons	Alkylated Silazanes
Amides	Amides
Amines	Amines
Aromatic Hydrocarbons	Carboxylic Acids
Carboxylic Acids	Fluoronated Alkyls
Ethers	Silazanes
Ketones	Succinamides
Nitrides	

Well dispersed systems had agglomerate diameters only slightly larger than the PCS mass mean particle diameter, relatively high zeta potential values (~60 MV), and higher turbidity than the non-dispersed systems. Centrifugal casting produced higher density compacts for well dispersed systems. Optimum systems were selected on the basis of these observations.

Pure alcohols provided moderate stability by a coulombic mechanism while a succinimide of molecular weight 1200 daltons in aliphatic hydrocarbons provided good stability by a more complex mechanism (perhaps steric-coulombic combined). All other dispersing systems were eliminated due to their low stability. The purity criterion was easily satisfied by alcohols dried to 30 ppm water by molecular sieve; the alcohol dispersed Si powders exhibited oxygen contents of 0.2 wt% by neutron activation analysis after drying to 600°C in ultra high purity Ar. However, the succinimide-hexane dispersed silicon contained 2.3 wt% oxygen after similar treatment. Both systems permit drying without destructive effluent generation. Pure alcohol was chosen as the medium for this study on the basis of the oxidation results. Methanol was selected from the group of alcohols for its low viscosity and high vapor pressure which facilitate colloidal pressing and drying.

The process conditions used for powder synthesis and the resulting powder characteristics are summarized in Tables I and II respectively. Increasing the laser power and the resulting maximum particle temperatures caused major changes in the types of particles, the types of aggregates, the mean particle sizes and the particle size distribution. The powders generally contain <100 ppm total impurities by emission spectroscopy and <0.1 wt% oxygen by neutron activation.

The powder designated B-004 represents our best early attempt to increase the mean particle size when the RBSN research was initiated; it contained three particle types. The first are the primary spherical particles (10-30 nm diameter) that form directly from the gas phase; their nucleation and growth kinetics have been modelled [6]. These uniform diameter primary particles have a log normal particle size distribution width parameter of 1.25. The second particle type consisted of chainy aggregates (2 to 20 particles) of the primary particles sintered together. The third particle type was large (80 to 500 nm) single or bicrystal particles that apparently form by melting and coalesence of the other two particle types. The overall median diameter, size distribution and percent of aggregates reflect the presence of the three particle types.

The high percentage of aggregates precluded fabricating high density Si parts from the as-synthesized B-004 powders. Consequently, the fines and aggregates were centifugally separated to produce a powder with a more uniform particle size distribution (B-004 SED). These sedimented powders were used for most of the subsequent processing research while synthesis reserach continued. Compact densities improved with the elimination of the fines and aggregates.

The two other powder types (F-028 and F-055) had larger particle sizes and particle size distributions but fewer aggregates than the sedimented powder. A TEM of the dispersed F-055 powder is shown in Figure 3. Initial experiments with these improved powders gave higher compact densities than the sedimented powder.

TABLE I. SYNTHESIS CONDITIONS FOR SILICON POWDERS

Powder Sample Number	Cell Pressure (MN/m^2)	Silane Mass Flow Rate (sccm)	Laser Power (watts)	Laser Intensity ($watts/cm^2$)	Max Brightness Temp. (°C)
B-004	0.071	30	180	5.7×10^3	1280
F-028	0.131	60	325	3.2×10^3	1455
F-055	0.131	110	325	3.2×10^3	1605

TABLE II. POWDER CHARACTERISTICS

Powder Sample Number	BET Equiv. Diameter (nm)	TEM Median Diameter By Mass (nm)	Diameter Distribution Width Parameter	Mass Fraction Aggregates (%)	Compact Density* (%)
B-004	115	175	1.79	17.2	45
B-004 SED	134	205	1.41	7.8	55
F-028	227	263	1.68	2.5	64
F-055	217	305	1.76	3.8	69

*Pressed with standard (69 MNm^{-2} pressure, 15 minute) pressing conditions.

C. Shaping

Parts were formed by colloidal pressing. Facilitated by a lubricating fluid acting under hydrostatic pressure, this process is capable of producing relatively defect free, high density compacts. The die apparatus is shown schematically in Figure 4. The solvent is extracted from the slip through membrane filters which cover porous stainless steel frits that are loaded by ported stainless steel pistons. The die is brass. Two porous frits are used in bidirectional pressing; one is used for unidirectional pressing.

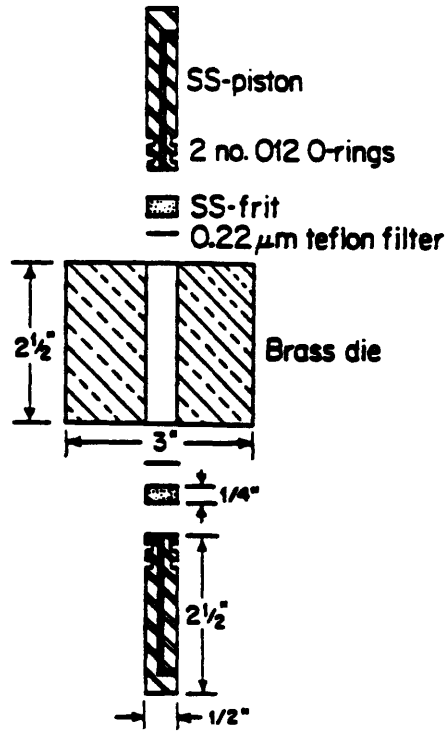

Fig. 4. Components making up colloidal pressing apparatus.

The silicon slip was prepared by sonicating a 5 vol% silicon methanol mixture in a glass vial for three minutes at a power level of 65 watts. The slip was then pipeted into the die and pressed.

Consolidation takes place in two stages, filtration and cake compaction. The slip is filtered through the porous membrane as load is applied, building up a porous cake [8]. A fluid extrusion rate of 1 cm^3 fluid/cm^2 of filter/minute was used in this study. Rearrangement of particles in the cake to form a high density compact occurs in the second stage of consolidation [9]. The final density is dependent on the die pressure.

Laminate flaws were found in the middle of the compacts formed with bidirectional pressing. These flaws formed when the opposing filter cakes met. For this reason unidirectional flow was utilized for this study.

Colloidal pressing times and pressures were varied to determine their effects on green density, flaws, yields of good parts, and nitrided strength. Time was varied between 0.5 and 60 minutes and pressure was varied between 17.3 and 276 MNm^{-2}. The results are reported in Table IV. Each box contains the yield of good green pellets (%), the green density (%) with standard deviation, the yield of "good" green pellets that survive firing, grinding and lapping (%) and the nitrided strength (MNm^{-2}) with standard deviation. With the exception of the 0.5 minute pressing time, none of these parameters change with pressing time. There is a small monotonic increase in the green density with increased pressure. The yields of both good green and fired parts drop off sharply for pressing pressures greater than 69 MNm^{-2}.

The densities achieved with the F-028 and F-055 powders (Table II) illustrate the importance of controlling aggregation and particle size distribution. Using the most reliable pressing conditions (69 MNm^{-2}, 15 minutes), these powders produced cake densities of 63 and 69% respectively.

A density of 63-64% corresponds to that of a random close packed structure [7] which is the maximum achievable without introducing ordering in uniform diameter spheres. Counting "nearly touching" neighbors, the structure achieves a coordination number in excess of 11. The volumetric expansion during nitriding should bring the "near" particles into direct contact thereby producing a structure whose perfection (pore size distribution and coordination number) approaches that of close packed arrays.

TABLE IV. COLLOIDAL PRESSING CONDITIONS AND RESULTS

USING POWDER TYPE B-004 SED

Pressing Pressure	Pressing Time (minutes)				
	0.5	1	3	15	60
17.3 MNm^{-2} 2,500 psi				100 52.7 ± 1.5 50 389	
35 MNm^{-2} 5,000 psi				100 53.3 ± 1.5 34.3 270 ± 61	
69 MNm^{-2} 10,000 psi	0 24.2 ± 2.5 NA NA	100 55.7 ± 0.9 60 330 ± 104	100 55.1 ± 0.7 40 327 ± 5	92.5 55.1 ± 2.6 58.2 311 ± 38	100 55.0 ± 0.8 80 199 ± 18*
138 MNm^{-2} 20,000 psi				58 55.6 ± 1.6 0 NA	
207 MNm^{-2} 30,000 psi	LEGEND % yield green parts % green density ± std.dev. % yield nitriding + grinding strength (MNm^{-2}) ± std. dev.			33 56.6 ± 0.3 0 NA	
276 MNm^{-2} 40,000 psi				0 57.4 ± 0.9 NA NA	

* Surface finish 600 grit, strengths not comparable to others.

D. Nitriding

Nitriding of the dried Si pellets was done in a nitrogen atmosphere (<10 ppm O_2, H_2O and CO_2 combined) without exposure to air. The kinetics were characterized by TGA/DTA prior to making samples for mechanical property measurements. With heating rates of 10°C/min up to 1200°C and 0.5°C/min up to 1400°C, nitriding commenced at approximately 1200°C and was completed below 1400°C. The mechanical test samples were nitrided by heating at 1°C/min up to 1200°C and 0.5°C/min up to 1400°C followed by a 1 hour soak at 1400°C. The slower initial heating rate was employed to avoid damaging the parts if not fully dried and the 1 hour soak insured complete nitridation. Nitriding was done in a top loading, cold-wall, vertical axis, tungsten heated furnace installed inside an Ar atmoshpere glove box.

The resulting pellets were characterized by weight gain, X-ray diffraction, optical microscopy, SEM, BET and Hg porosimetry. The average weight gain corresponds to 96.3% of the stoichiometric value based on the weight of the dry Si pellets. The discrepancy probably results from a combination of incomplete drying of the pellets and volatilization of the unreacted Si; condensates formed on the cold furnace walls. X-ray and microstructural analysis showed no evidence of unreacted Si. The α/β ratio was >9.0. Hg porosimetry showed all pores to have diameters between 10 and 60 nm for final densities ranging from 65 to 83%. The fractional densities after nitriding were close to the values anticipated from densities of the unreacted Si pellets. The small discrepancies probably result from the technique used to measure the dimensions of the fragile, unreacted Si pellets.

The features shown in the SEM fracture surface (Figure 5) corroborate the other characterizations. The nitride phase exists as a continuous network exhibiting characteristic dimensions between 0.2 and 0.7 μm, nominally agreeing with the BET equivalent size (~0.24 μm). Interparticle pore diameters range from 0.1 to 0.25 μm diameter. Because Hg porosimetry measures interparticle neck sizes rather than pore diameters, these pore dimensions are in reasonable agreement. The larger topographical features (~1.0 μm) may reflect larger internal flaws or may simply be artifacts of the crack path. The absence of typically observed needles and whiskers [10] is a direct consequence of nitriding without oxygen exposures or additions. Lower magnification micrographs of fracture surfaces revealed occasional 5-15 μm diameter pores.

The time-temperature cycle used for nitriding in this research is contrasted with normal practice in Table V. The nitriding time corresponds to the cumulative time in the nitriding temperature range. Even using a N_2 atmosphere, rather than N_2-H_2 or NH_3 atmospheres which give faster kinetics, these dispersed Si powders reacted to completion much more rapidly and at lower temperatures than have been reported. The enhanced reactivity results directly from the absence of oxygen and the small particle sizes. Exposure to oxygen inhibits the nitridation of these powders. The same rapid nitriding kinetics were observed for final densities up to 83% illustrating that the achieved structures leave open channels for the reactant gas.

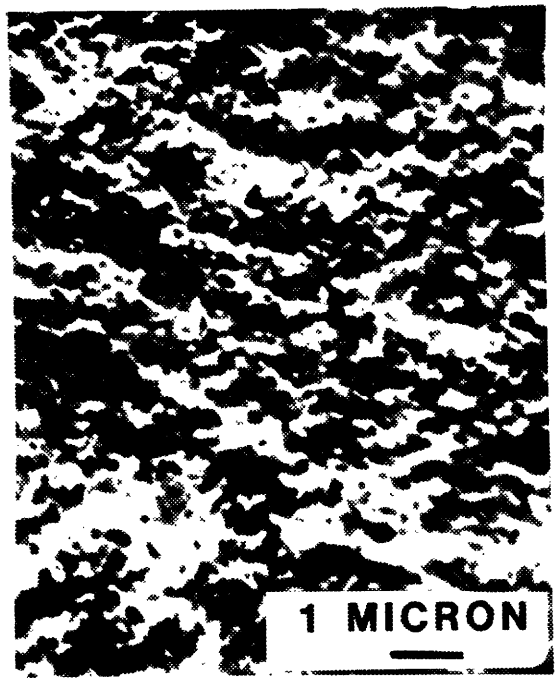

Fig. 5. Fracture surface of fully nitrided sample made from Si powder type B-004 SED RBSN.

The observed change in the BET surface area with nitriding indicates that a smooth, crack free nitride layer forms directly on the Si particles. Thus, the scale, homogeneity and perfection of the final microstructure evolve directly from those of the as-formed Si particles. We typically observed that the surface area decreased from ~15.0 m^2/g for the unreacted B-004 SED powder to a value of ~8.2 m^2/g after nitriding. This corresponds to the 55% decrease predicted on the basis of a 22% increase in the volume of solids and the change in density that result from nitriding a BCC arrangement of Si particles. These results indicate that these high purity Si particles nitride by mechanisms that differ from other reported mechanisms [10].

TABLE V. COMPARISON OF RBSN PROCESSING HISTORIES

Reference	Heating Time (hrs)	Nitriding Time (hrs)	Nitriding Temperature Range (°C)
Ford Motor Co.			
Ref. 11	-	60	1250-1460
Ref. 12	~10	150	1000-1400
AMMRC			
Ref. 13	4	68	1300-1400
Ref. 14	4	75	1350-1460
Ref. 15	4	54	1250-1460
Ref. 16	4	110	1150-1390
Brown University [17]	20	84	1100-1400
MIT			
Dry-Pressed [18]	1.3	120	1100-1410
Dispersed	20	7	1200-1400

III. MECHANICAL PROPERTY MEASUREMENTS

Room temperature strengths, fracture toughness (K_{IC}) and hardness measurements were made on nitrided samples. Strengths were measured under biaxial tension using the ball on ring technique [19]. K_{IC} values were determined by the indentation technique [20] using a Vickers Hardness instrument.

The ball on ring technique was employed rather than the conventional 3 or 4 point bending tests because it does not induce stresses at the free edges of samples. Sample fabrication costs are low because only one surface needs to be finished to high tolerance. Also, we felt that this test provided the most severe test of intrinsic strengths.

Samples were produced with three surface finishes. These were grinding with 320 grit to final dimensions, 600 grit grinding on the tensile surface to final dimensions after 320 grit roughing, and lapping with 2.0 μm diamond on the tensile surface after 320 and 600 grit roughing.

The results of the lapped strength measurements are given in Table IV and results for the 320 grit , 600 grit and lapped samples are shown as regions D, E and F respectively in Figure 6, as functions of density. Figure 6 also summarizes 377 strength results taken from 40 references [10,21-24 typical] in region B. These samples include laboratory and commercial materials with all surface finishes. To put all this data on a similar basis, four-point bend strengths were transformed to probable 3-point values [24]. Curve C represents a least square fit of an

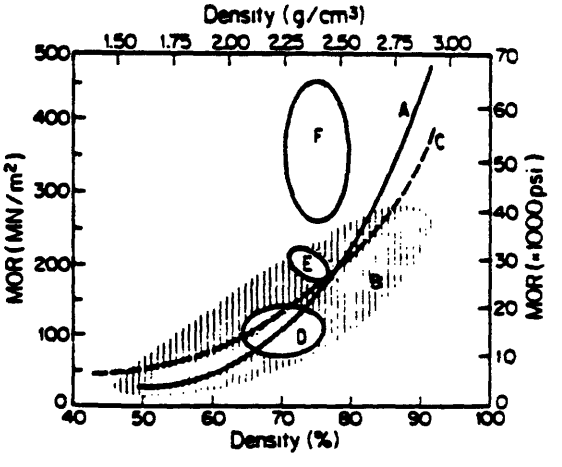

Fig. 6. RBSN modulus of rupture data as a function of sample density. See text for explanation of curves and regions.

exponential function to the data in region B. Curve A is Moulson's [10] exponential representation that was force fitted to include HPSN strengths at 100% density.

Surface finish has an obvious effect on the strengths of our samples. The orientations of the flaws which propagated matched the directions of the grinding tracks in unlapped samples. Both results show that the strengths in regions D and E are controlled by grinding induced surface flaws rather than internal flaws that are characteristic of our RBSN. The lapped samples appear to have broken from flaws that are characteristic of the material since cracks showed no preferred orientation and fracture surfaces frequently contained 5-15 μm diameter pores. Application of the simple Griffith equation [25] to the observed strengths yields flaw sizes of 5 to 27 μm.

The strengths exhibited by the laser originating RBSN samples are clearly superior to reported values. The strengths of all of our lapped samples exceed the strengths of all other cited strengths for corresponding densities. Also, others have shown [26] that the ratio between strengths of ground samples oriented parallel and perpendicular to the grinding direction is 1.5-2.0. Thus, our biaxial tests were always oriented in the least favorable orientation. Our highest strengths are 1.6 times higher than the highest strength reported for much higher density RBSN. Further strength improvements are anticipated for the high density compacts made possible with the F-028 and F-055 powders.

Vickers hardness values were determined on polished surfaces using 300 and 500 gram loads. Observed values ranged from 7.4 to 11.3 GNm^{-2}. Even for lower density samples, these values are comparable to or higher than those of 83-85% dense, highly optimized RBSN (~8.3 GNm^{-2}) [18]. All of the unidirectional flow pressed samples exhibited K_{IC} values between 2.3 and 3.6 $MNm^{-3/2}$. These are markedly higher than is characteristic of the optimized type RBSN (~2.0 $MNm^{-3/2}$) [18]. Bidirectional flow pressed samples had lower K_{IC} values (~1.2-1.5 $MNm^{-3/2}$) but did not show relatively low strengths. We are continuing to investigate the factors that gave the observed superior H and K_{IC} values. A good theoretical basis does not exist for interpreting these properties in relatively porous ceramics in terms of fracture mechanics models.

IV. CONCLUSIONS

The achievement of superior RBSN mechanical properties through improved microstructures has been demonstrated. Refined process control from the initial synthesis of the Si powders to their final nitriding is the basis for these improvements. Eliminating aggregates in reasonably uniform diameter Si powders, avoiding oxygen contamination and using nonaqueous dispersing systems are the major issues, although superior properties are realized only if care is exercised for all processing steps.

Even with relatively low density RBSN, demonstrated strengths were higher than all previously reported values. Further strength improvements are anticipated with the higher green density compacts made possible with recent powders. These 85% dense RBSN samples satisfy Thumler's pore size and density criterion for oxidation resistant RBSN.

V. ACKNOWLEDGEMENTS

Several MIT researchers contributed directly to the achievement of the improved Si powders and pressing conditions needed to carry out this research; these include J. Flint, S. Akmandor, A. Lightfoot, C. Harris, E. Paik and D. Lum. Dr. T. Service, U. Mass., assisted with mechanical

property measurements. The research was primarily supported by the Office of Naval Research and Army Research Office under contract N00014-82-K-0350. All contributions are gratefully acknowledged.

VI. REFERENCES

[1] M.L. Torti, R.A. Alliegro, D.W. Richerson, M.E. Washburn and G.Q. Weaver, Proc. Brit. Ceram. Soc. 22, 129 (1973).

[2] E. Porz and F. Thummler, J. Mat. Sci., 19 ,1283-1295 (1984)

[3] W.R. Cannon, S.C. Danforth, J.H. Flint, J.S. Haggerty and R.A. Marra, J. Am. Ceram. Soc., 65 [7], 324-330 (1982).

[4] W.R. Cannon, S.C. Danforth, J.S. Haggerty and R.A. Marra, J. Am. Ceram. Soc., 65 [7], 330-335 (1982).

[5] J.H. Flint and J.S. Haggerty, Applications of Lasers to Industrial Chemistry, SPIE, Vol. 458 (1984).

[6] R.A. Marra, PhD Thesis, MIT, 1982.

[7] J.D. Bernal and J. Mason, Nature, 188, 908 (1960).

[8] R.H. Perry and C.H. Chilton, Chemical Engineers Handbook, McGraw Hill Co., NY (1973).

[9] T.W. Lambe and R.V. Whitman, Soil Mechanics, J. Wiley & Sons, NY, 406-422, (1969).

[10] A.J. Moulson, J. Mat. Sci. 14, 1017-1051 (1979).

[11] J.A. Mangels, J. Am. Ceram. Soc., 58 [7-8], 354, (1975).

[12] J.A. Mangels, Am. Ceram. Soc. Bull., 60 [6], 613-617 (1981).

[13] D.R. Messier, P. Wong and A.E. Ingram, J. Am. Ceram. Soc., 56 [3], 171 (1973).

[14] D.R. Messier and P. Wong, J. Am. Ceram. Soc., 56 [9], 480 (1973).

[15] D.R. Messier and P. Wong, Ceramics for High Performance Applications p. 181, (1974).

[16] P. Wong and D.R. Messier, Am. Ceram. Soc. Bull., 57 [5], 525 (1978).

[17] S.C. Danforth and M.H. Richman, Am. Ceram. Soc. Bull., 62 [4], 501 (1983).

[18] S.C. Danforth and J.S. Haggerty, J. Am. Ceram. Soc. 64[4], C-58 (1983).

[19] D.K. Shetty et al., Am. Ceram. Soc. Bull., 59 [12], p. 1193-1197 (1980).

[20] G.R. Anstis et al., J. Am. Ceram. Soc., 64 [9], 533-538 (1981).

[21] D.C. Larsen and J.W. Adams, Technical Report AFWAL-TR-83-4141, April 1984.

[22] L.J. Lindberg, D.W. Richerson, N.D. Carruthers and H.M. Gersch, Am. Ceram. Soc. Bull., 61[5], 574-578 (1982).

[23] F.L. Riley, "Nitrogen Ceramics" (Nordhoff, Leyden), (1977) p. 265

[24] D.J. Godfrey and M.W. Lindley, Proc. Brit. Ceram. Soc. 22, 229 (1973).

[25] F.W. Smith, A.F. Emery and A.S. Kobayashi, J. Appl. Mech. 34, Series E, 453-459 (1967).

[26] C.A. Anderson and R.J. Bratton, The Science of Ceramic Machining and Surface Finishing II, NBS Special Publication 562 (1979), 463-476.

HIGH STRENGTH, OXIDATION RESISTANT REACTION-BONDED SILICON NITRIDE FROM LASER-SYNTHESIZED SILICON POWDER

J.S.Haggerty, J.H.Flint, G.J.Garvey, J-M.Lihrmann, J.E.Ritter*

ABSTRACT

Reaction bonded silicon nitride made from laser synthesized silicon powders has superior mechanical properties, oxidation resistance and nitriding kinetics (time < 7 hours at 1420°C). Average values of hardness (9.2 GNm^{-2}), fracture toughness (2.8 $MNm^{-3/2}$), and strength (300 MNm^{-2}) are reported. Saturation oxidation weight gains in air at 1250°C are less than 1%.

I. INTRODUCTION

Reaction bonded silicon nitride (RBSN) is a candidate ceramic for applications requiring high strength, thermal shock, and oxidation resistance up to ~1370°C. Room temperature strengths of RBSN are lower than those of hot pressed (HPSN) and sintered silicon nitride (SSN) [1] because of residual porosity; however, high temperature strengths can exceed those of HPSN and SSN since sintering aids generally are not employed in RBSN. For RBSN, nitride formation within the pore structure of the Si compact results in neglible changes in part dimensions. Recent evidence indicates that parts with superior microstructures have both improved oxidation resistance [2] and strength. It appeared feasible to produce RBSN with the required small pore dimensions and high, uniform densities using the Si powders produced by the laser synthesis process.

II. RBSN PROCESSING STEPS

Reaction bonded silicon nitride was made by nitriding previously shaped, porous parts made of Si powders. The silicon powders were processed with minimal exposure to oxygen. Anaerobic, anhydrous processing included storage, handling, forming and drying in Ar (<10ppm O_2; <3ppm H_2O).

A. Powder Synthesis

The Si powders were synthesized by the CO_2 laser induced pyrolysis of SiH_4 gas [3]. This process was developed to produce powders having small diameters, spherical shapes, uniform size distributions, freedom of aggregates and high purity. Powders with these characteristics were expected to produce unfired parts with the highly perfect microstructures needed to achieve improved oxidation resistance and strengths.

These powder characteristics result from the unusual time-temperature excursions experienced by the reactants and the reaction products. Using the reaction cell shown in Figure 1 and a CW-CO_2 laser, reactant gas heating rates ~10^6°C/sec, reaction times of ~10^{-3}sec and cooling rates of ~10^5°C/sec are achieved. These process conditions permit nucleation, growth and coalescense processes to be controlled in a manner that yields powders having the desired

Massachusetts Institute of Technology, Cambridge, MA 02139
*University of Massachusetts, Amherst, MA 01003

Proceedings 2nd International Symposium, Ceramic Materials and Components for Engineers, Lübeck-Travenmünde, Federal Republic of Germany, April 1986.

characteristics in high particle number density gas streams.

The process conditions used for powder synthesis and the resulting powder characteristics are summarized in Table I. The powders generally contained <100 ppm total impurities by emission spectroscopy and <0.1 wt% oxygen by neutron activation. The powder designated B-004 represented our best powder when the RBSN research was initiated; it contained three particle types. The first consisted of the primary spherical particles (10-30 nm diameter) that form directly from the gas phase; their nucleation and growth kinetics have been modelled [4]. These particles have a log normal particle size distribution width parameter (σ_{LN}) of 1.25. The second type consisted of chainy aggregates (2 to 20 particles) of the primary particles sintered together. The third type were large (80 to 500 nm) single or bicrystal particles that form by melting and coalescence of the other two particle types.

The high percentage of aggregates precluded fabricating high density Si parts from the as-synthesized B-004 powders. Consequently, the fines and aggregates were centrifugally separated to produce a powder with a more uniform particle size distribution (B-004-SED). These sedimented powders were used for the subsequent processing research while synthesis research continued. Compact densities improved with the elimination of the fines and aggregates.

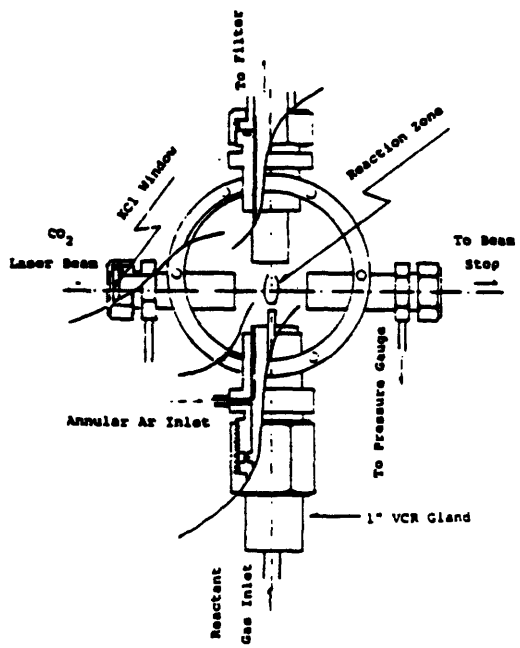

Fig. 1. Schematic of the reaction cell.

TABLE I. SYNTHESIS CONDITIONS AND POWDER CHARACTERISTICS

POWDER NUMBER	PRESSURE (NM m^{-2})	SILANE FLOW RATE (sccm)	LASER POWER (watts)	TEMP MAX (°C)	DIAMETER (nm)	MASS % AGGREGATE	Si COMPACT DENSITY (%)	RBSN DENSITY (%)
B-004	0.071	30	180	1280	175	17	45	55
"-SED	-	-	-	-	205	8	53	65
F-028	0.131	60	325	1455	263	3	59	72
F-055	0.131	110	325	1605	305	4	62	75

The two other powder types (F-028 and F-055) resulted from continued synthesis research. They have larger particle sizes and width parameters and fewer aggregates than the B-004-SED powder. A TEM of as-synthesized F-055 powder is shown in Figure 2. Both of these powders gave higher compact densities than the sedimented B-004 powder. Processing research has continued using these powders without centrifugal separation.

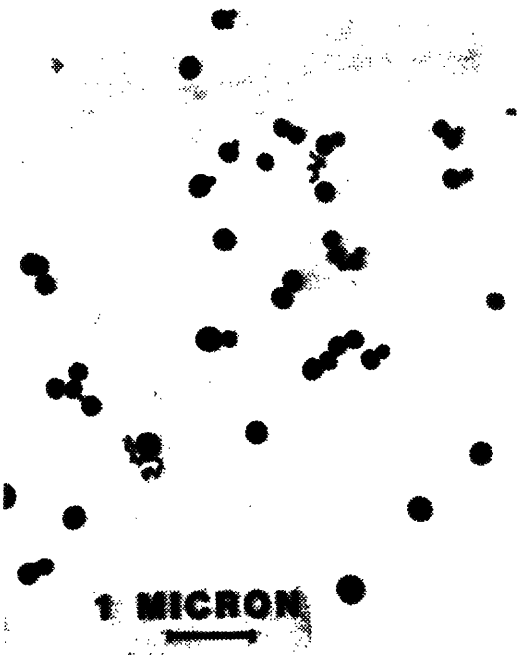

Fig. 2. TEM photomicrograph of as-synthesized Si powder (F-055).

B. Powder Dispersion

Our objective was to form defect free, high coordination number green bodies from dispersions; random close packed structures [5] were sought. The criteria for selecting a dispersing medium for silicon were based on dispersion stability, oxygen contamination, drying kinetics, residues and the absence of destructive effluents. Pure solvents screened included alcohols, amines, amides, aldehydes, aromatic and aliphatic hydrocarbons, carboxylic acids, ethers and ketones. Dispersants examined included alcohols, amines, amides, carboxylic acids, fluoronated alkyls, silazanes and succinimides, each in hexane, toluene, alcohol and acetonitrile solvents. Stability was evaluated by light-scattering, photon correlation spectroscopy (PCS), sedimentation rate, sediment density, and microelectrophoretic mobility.

Well dispersed systems had PCS diameters only slightly larger than TEM diameters, and higher turbidity than the poorly dispersed systems. Centrifugal casting produced higher density compacts for well dispersed systems.

Pure alcohols provided moderate stability by a DLVO mechanism while a succinimide of molecular weight 1200 daltons in hexane provided good stability by a more complex mechanism (perhaps steric-DLVO combined). Both systems permit drying without destructive effluent generation. All other dispersing systems were eliminated due to their lower stability. After drying at 600°C in ultra high purity Ar, alcohol dispersed powders contained less oxygen than succinimide-hexane dispersed powders (0.2 wt% vs. 2.3 wt%); methanol was selected for its low viscosity and high vapor pressure.

C. Shaping

Parts were formed using a colloidal press [6]. The solvent is extracted from the slip through membrane filters

which cover porous stainless steel frits that are loaded by ported stainless steel pistons. The die is brass. Two porous frits are used in bidirectional pressing; one is used for unidirectional pressing. Unidirectional flow was utilized because laminate flaws formed at the middles of the bidirectionally pressed compacts.

The silicon slip was prepared by sonicating a 5 vol% silicon-methanol mixture for three minutes at a power level of 65 watts. The slip was then pipeted into the die and pressed. Consolidation takes place in two stages: filtration and cake compaction. A porous cake [7] builds up as the slip is filtered through the porous membrane with an applied load. A fluid extrusion rate of 1 cm^3 fluid/cm^2 of filter/minute was used. Rearrangement of particles in the cake to form a high density compact occurs in the compaction stage [8]. The final density is dependent on the die pressure.

Colloidal pressing times and pressures were varied to determine their effects on green density, flaws, yield of good parts, and nitrided strength. There was no change in green density for times greater than 1/2 minute. The variable pressure results are described by a straight line (Fig. 3) when the reciprocal of fractional green density is plotted against the log of pressing pressure. This result implies [9] that a single rearrangement mechanism is operative. Also presented in this figure is the relationship between processing yield and pressing pressure. The yield drops off dramatically for pressing pressures above 69 MN m^{-2} due to the incorporation of laminate flaws. Evaluated samples were pressed at or below 69 MN m^{-2} (most at 69 MN m^{-2}).

The densities achieved with the F-028 and F-055 powders (Table I) illustrate the importance of controlling aggregation and particle size distribution. These powders produced cake densities of 59 and 63% respectively.

A density of 63% corresponds to that of a random close packed structure [5]. Counting "nearly touching" neighbors, it achieves a coordination number (CN) over 11. The volumetric expansion during nitriding should bring the "near" particles into direct contact thereby producing a structure whose perfection (pore size distribution and CN) approaches that of close packed arrays (CN=12).

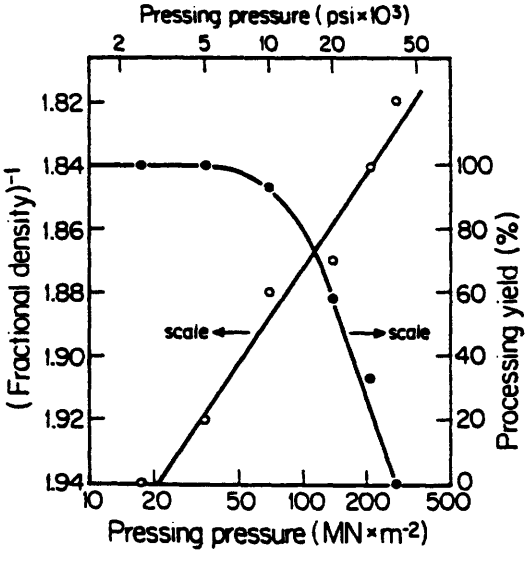

Fig. 3. Density and yield of colloidally pressed pellets as functions of pressure.

D. Nitriding

Nitriding of the dried Si pellets was done without exposure to air in a top loading, cold-wall, vertical axis, tungsten furnace installed within an Ar atmosphere glove box (<10ppm O_2 & H_2O combined). The test samples were completely nitrided by heating at 1°C/min up to 1200°C and 0.5°C/min up to either 1410°C (B-004-SED) or 1420°C (F-055), followed by a 1 hour hold. The slow initial heating rate was employed to avoid damaging the parts if not fully dried.

X-ray analysis showed no evidence of unreacted Si in the nitrided pellets of density <76%, an α/β ratio of approximately 90/10 and a nitride grain size of 28 nm for α and 33 nm for β. Hg porosimetry pore neck radii were between 5 and 30 nm for all densities. The nitride phase, shown in the SEM fracture surface in Figure 4, is a continuous network with characteristic dimensions between 0.2 and 0.7 μm, nominally agreeing with both the RSBN BET equivalent size (~0.24 μm) and the Si particles. Pore radii (50-125 nm) exceed the interpore neck dimensions measured by Hg porosimetry. The absence of typically observed needles and whiskers [10] is a direct consequence of processing without oxygen exposures or additions. Micrographs of fracture surfaces frequently revealed 5-15 μm diameter isolated voids.

Compared to conventional time-temperature cycles reported in the literature [11], these Si powders reacted to completion much more rapidly and at lower temperatures. The enhanced reactivity results from high purity and the small particle sizes. The same rapid nitriding kinetics were observed for final nitrided densities up to 76%.

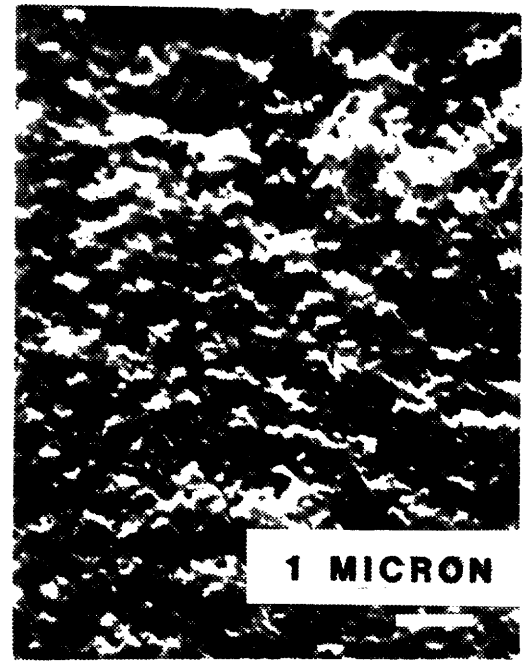

Fig. 4. Fracture surface of RBSN made with laser-synthesized Si powder (B-004-SED).

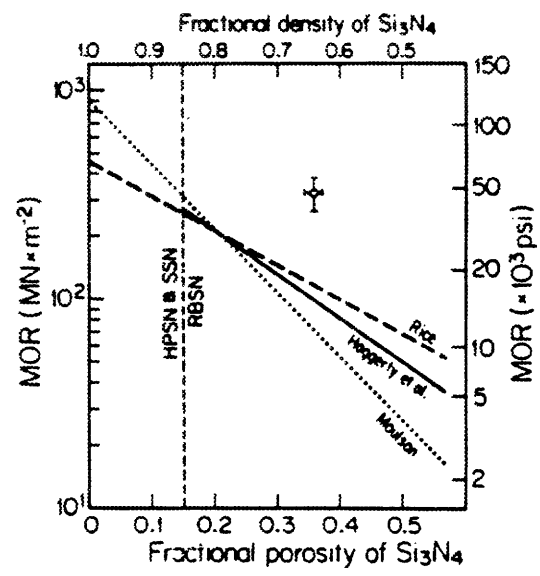

Fig. 5. Room temperature strength of silicon nitride vs. density.

The surface area decreased from ~15.0 m^2/g for the unreacted B-004-SED powder to a value of ~8.2 m^2/g after nitriding. This change corresponds to the 45% decrease in surface area predicted on the basis of a 22% increase in the volume of solids and the change in density that result from nitriding a BCC arrangement of Si particles with fixed interparticle spacing. Changes in the BET surface area with nitriding, microstructures and x-ray grain sizes indicate that the nitride forms as a dense, polycrystalline layer directly on the Si particles indicating a reaction mechanism that differs from those reported by others [10].

III. MECHANICAL PROPERTY MEASUREMENTS

A ball-on-ring biaxial strength test was used to determine the room temperature strengths of the nitrided samples; hardness and fracture toughness were measured using a Vickers indenter.

The ball-on-ring test was used to eliminate spurious edge effects. An apparatus based on the design by Wachtman et al. [12] was used in conjunction with an Instron Corp. universal testing machine. The ball diameter was 6.35 mm. The samples were tested using a fast crosshead speed (0.05cm/min). Fracture strength, σ_f, was calculated [13] from:

$$\sigma_f = \frac{3P(1+\nu)}{4\pi t^2}\left[1+2\ln\frac{a}{b}+\frac{(1-\nu)}{(1+\nu)}\left(1-\frac{b^2}{2a^2}\right)\left(\frac{a^2}{R^2}\right)\right],$$

where P = fracture load, ν = Poisson's ratio (taken to be 0.25), t=sample thickness = 1mm, R = sample radius = 6.35 mm, a = load support ring radius = 6.27 mm and b = ball contact radius (taken to be 0.333 mm = t/3).

Observed strengths were independent of the pressing times and pressures used to form the green Si parts. Figure 5 shows the average σ_f(300 MNm^{-2}) of the 20 samples made from B-004-SED with error bars corresponding to the standard deviations in density and strength (± 55 MNm^{-2}). For comparison it also gives three different lines representing least-square fits of exponential functions to RBSN, SSN and HPSN strength data reported in the literature [6,10,14] for laboratory and commercial samples with all surface finishes.

Laser-originating specimens that were diamond

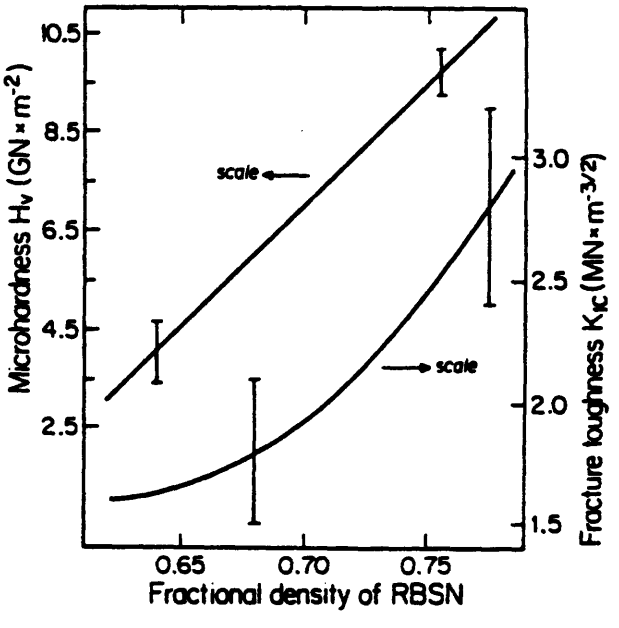

Fig. 6. Hardness and fracture toughness of laser-originating RBSN vs. density. Error bars are typical.

lapped to 4 μm exhibit an average strength that is 2.8 to 4.4 times the average reported values at a corresponding density. The highest strengths measured (450 MNm^{-2}) were 60% higher than the highest average strength reported for an optimized 85% dense RBSN (290 MNm^{-2}) [15] and 15% higher than the highest reported strength [16] for RBSN (389 MNm^{-2}). These lapped specimens broke from processing flaws of two types. Fracture sources were usually either 5-15 μm diameter voids or preexisting lenticular cracks less than 50 μm deep perpendicular to the stress axis. Application of the Griffith equation [17] to the observed strengths yields flaw sizes of 4 to 16 μm.

Vickers hardness values were determined on polished surfaces using 300 and 500 gram loads. Observed values (Figure 6) ranged from 3.5 to 11.0 GNm^{-2}. The hardness of our 77% dense RBSN (~10 GNm^{-2}) is higher than that of 85% dense, highly optimized commercial RBSN (~8.3 GNm^{-2}) [15]. Using the indentation technique [18], our dense specimens exhibited an average K_{IC} value of 2.8 $MN/m^{-3/2}$ (Figure 6). These are higher than is characteristic of the optimized commercial RBSN (~2.0 $MNm^{-3/2}$) [15]. We are continuing to investigate the factors that are responsible for these superior hardness and K_{IC} values.

IV. OXIDATION RESISTANCE

Figure 7 shows that the oxidation resistance of laser-originating RBSN at 1250°C in flowing air is strongly dependent on the porosity level and pore size. As predicted by Thummler's [2] results at the same temperature, our low density specimens undergo significant internal oxidation before saturation is attained. For densities >85% and Hg porosimetry pore radii <60 nm, he showed that internal oxidation would be reduced to less than 1% due to pore closure by the oxide product. The extent of our oxidation at 1250°C in air was less than 1% for specimens having densities as low as 74%. This superior performance at lower densities probably results from our samples having smaller pore diameters and more uniform microstructures.

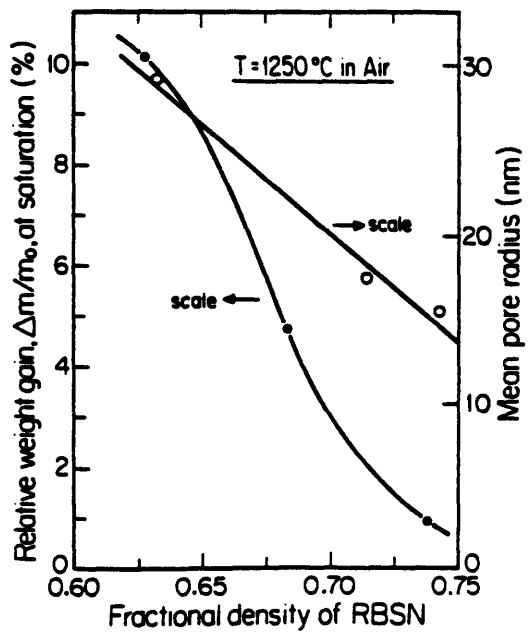

Fig. 7. Oxidation weight gain and pore size of laser-originating RBSN vs. density.

V. CONCLUSIONS

The achievement of superior RBSN mechanical properties through improved microstructures has been demonstrated. Refined process control from the initial synthesis of the Si powders to their final nitriding is the basis for these improvements; critical steps include eliminating aggregates in reasonably uniform Si pow-

ders, avoiding oxygen contamination and using nonaqueous dispersing systems. Even with relatively low density RBSN, demonstrated strengths were higher than all previously reported values. Also, these 74-77% dense RBSN samples achieved oxidation resistance that Thummler had shown was feasible for highly perfect RBSN. Further strength improvements are anticipated with the higher green density compacts made possible with recent powders.

VI. ACKNOWLEDGEMENTS

The authors acknowledge D.Lum at M.I.T. who did the fractography, and W.Dunlay and T.Service at U. Mass., who did the mechanical tests. The research was primarily supported by the Office of Naval Research and Army Research Office under contract N00014-82-K-0350 and secondarily by a group of industrial sponsors (Abex Corp., Aisin Seiki, Alcoa, Japan Steel Works, NGK Spark Pluq, Nippon Steel Corp., Sumitomo Electric Corp., and Toa Nenryo Kogyo). These and other contributions are gratefully acknowledged.

VII. REFERENCES

[1] M.L. Torti, R.A. Alliegro, D.W. Richerson, M.E. Washburn and G.Q. Weaver, Proc. Brit. Ceram. Soc. 22, 129 (1973).
[2] E.Porz and F.Thümmler, J.Mat.Sci., 19, 1283-95 (1984).
[3] Ref. 3-5 in [6].
[4] R.A. Marra, PhD Thesis, MIT, 1982.
[5] J.D. Bernal and J. Mason, Nature, 188, 908 (1960).
[6] J.S. Haggerty, G. Garvey, J.-M. Lihrmann and J.E. Ritter, Proceedings of the 1985 MRS Fall Meeting, Symposium L , in press.
[7] R.B. Bird, W.E. Stewart and E.N. Lightfoot, Transport Phenomena, J. Wiley, N.Y, (1960), pp. 196-200.
[8] T.W. Lambe and R.V. Whitman, Soil Mechanics, J. Wiley & Sons, NY, 406-422, (1969).
[9] O.J. Whittemore, Jr. in Ceramic Processing Before Firing, ed. by G.Y.Onoda and L.L.Hench, J.Wiley, NY (1978), p. 350.
[10] A.J. Moulson, J. Mat. Sci. 14, 1017-1051 (1979).
[11] Ref. 11-17 in [6].
[12] J.B. Wachtman, Jr., W. Capps and J. Mandel, J. Mater. Sci., 7 (2), 188 (1972).
[13] D.K. Shelty, A.R. Rosenfield, P. McGride, G.K. Bansal and W.H. Duckworth, Am. Ceram. Soc. Bull., 59 (12), 1193 (1980).
[14] R.W. Rice, J. Mater. Sci., 12 (7), L627 (1977).
[15] S.C. Danforth and J.S. Haggerty, J. Am. Ceram. Soc. 64 [4], C-58 (1983).
[16] M.E. Washburn and H.R. Baumgartner, Ceramics for High Performance Applications, 1974, p. 479.
[17] F.W. Smith, A.F. Emery and A.S. Kobayashi, J. Appl. Mech., 34, Series E, 1453-459 (1976).
[18] G.R. Anstis, P. Chantikul, B.R. Lawn and D.B. Marshall, J.Am. Ceram.Soc., 64 (9), 53 (1981).

Accepted for publication in
the Journal of American Ceramics
Society

J88-03

HIGH STRENGTH REACTION BONDED SILICON NITRIDE

J.E. Ritter, S. V. Nair, P. Gennari, W.A. Dunlay
University of Massachusetts
Amherst, MA 01003

and

J.S. Haggerty, G. J. Garvey*
Massachusetts Institute of Technology
Cambridge, MA 02139

ABSTRACT

High purity, small diameter silicon powders made from laser heated SiH_4 have been used to fabricate 76% dense reaction bonded silicon nitride samples with a fine, uniform microstructure. Room temperature strengths were 75% greater than conventionally processed RBSN (83% dense) with toughness and hardness values being about 10% greater. These high strengths result from uniformly distributed, small diameter pores (<15 μm) made possible from the combination of ideal powders and careful post-synthesis processing.

* Present address: ABEX Co., Mahwah, N.J.

INTRODUCTION

Reaction bonded silicon nitride (RBSN) is usually made from "commercial" silicon powder of about 5-15 μm diameter.[1] Historically, room temperature strength of RBSN is lower than hot pressed silicon nitride (HPSN) since the strength is limited by the size of the largest pore present.[1] On the other hand, high temperature strengths of RBSN can exceed those of HPSN since sintering aids are not employed in the reaction bonding process.[1,2]

This communication reports the fabrication of high strength RBSN made from nitriding extremely fine (approximately 0.3 μm diameter), high purity Si powder synthesized from laser heated SiH_4. It was believed that this starting powder would yield a RBSN of high microstructural quality with a very fine, flaw-free microstructure, resulting in an RBSN with superior properties.[3]

EXPERIMENTAL PROCEDURE

The detailed techniques used to produce RBSN samples are described elsewhere.[4-6] Briefly, high purity Si powder (approximately 0.3 μm diameter) is synthesized by the pyrolysis of CO_2 laser heated SiH_4 gas. The Si powder is dispersed in a methanol solution and disc shaped specimens are formed by colloidal pressing. In this technique the solvent is extracted through membrane filters supported by porous frit loaded by ported pistons in a die. Unidirectional pressing is used since laminate cracks formed

along the midplanes of bidirectionally pressed compacts. After removal of an optimum amount of methanol, the samples are cold isostatically pressed (275 MPa) and then dried for 24 h in a N_2 atmosphere using an 8 h linear heating ramp to 200°C. Samples are nitrided in a tungsten furnace installed inside an Ar atmosphere glove box so that the samples are never exposed to air. Complete nitridation is achieved by heating at 1°C/min to 1200°C and then 0.5°C/min to 1420°C, followed by a 1 h hold. Samples are then ground and diamond polished to 4 μm on the tensile surface. The final dimensions of the samples are 12.7 mm in diameter and 1 mm thick.

The samples have a porosity of 24% and X-ray analysis showed 90% α-Si_3N_4 and the balance β - Si_3N_4. X-ray line broadening showed nitride crystal sizes of 0.028 μm for α and 0.033 μm for β. By SEM observation the nitride phase is a continuous network with characteristic solid phase dimensions between 0.2 and 0.7 μm, which is consistent with the starting Si particle size. Hg porosimetry pore neck diameters are between 0.010 and 0.060 μm. Observed pore diameters (0.10-0.25 μm) exceed the interpore neck dimensions measured by Hg porosimetry. Micrographs reveal occasional 5-15 μm isolated pores.

Mechanical testing was done to evaluate hardness, fracture toughness, and fracture strength. Hardness was measured using a Vickers indenter+ at loads from 20 to 50 N. Fracture toughness was measured using the Vickers indentation technique where toughness (K_c) is given by:[7]

+ Tukon, Measurement Systems Division, ACCO Industries, Inc., Bridgeport, CT.

$$K_c = 0.016\ (E/H)^{1/2}\ PC^{-3/2} \qquad (1)$$

where E is elastic modulus, H is hardness, P is indentation load, and C is the average measured radial crack length. The E/H ratio was determined by measuring the diagonals of a Knoop indentation at an indent load of 12 N where:[8]

$$H/E = 0.3125 - \frac{1}{0.45}\ (b/a) \qquad (2)$$

b is the length of the short diagonal and a is the length of the long diagonal. All strength tests were done at room temperature at a crosshead speed of 0.5 cm/min, corresponding to a stressing rate of about 60 MPa/S. A ball-on-ring test apparatus with a support ring 10.46 mm was used in conjunction with a universal testing machine.[#] The appropriate equation to calculate fracture strength is given in ref. 9.

To compare the ball-on-ring test with the more standard four-point bend test, HPSN samples (NC132[@]) polished to 4 μm finish were tested using the above ball-on-ring fixture and the strengths compared to those measured by the manufacturer using the MIL-STD-1942(MR) four-point bend test.[10] The ball-on-ring test gave an average strength of 945 MPa (±60) and the four-point bend test 868 MPa (± 109). The 9% higher strength of the ball-on-ring test compares quite well with the 11% increase as predicted from Weibull statistics[11] where the effective stressed areas of the two tests were

---

Instron Corp., Canton, MA.
@ Norton Co., Worcester, MA.

calculated to be 19.6 mm^2 (ball-on-ring) and 48.8 mm^2 (four-point bend), respectively.

It is important to note that the strengths for this SiH_4-derived RBSN were systemmatically improved by identifying the fracture origins and then eliminating (or minimizing) them by processing modification.[6,12] The major large processing flaws were inclusions from die contamination, large pores introduced during sonication of the slip, and lenticular cracks introduced in colloidal pressing. The average strengths of the samples processed under optimum conditions correspond to a semi-circular flaw size of about 10 μm,[13] which is quite consistent with the observed, isolated pores of 5-15 μm diameter that exist in the structure. During the optimizing of the processing procedures, hardness and toughness did not vary, indicating that these properties depend on the microstructure of the RBSN and not on isolated defects.

RESULTS AND DISCUSSION

Table 1 summarizes the mechanical test results for the SiH_4-derived RBSN. These results are based on an average from eight samples. Commercial RBSN (NC350) and two HPSN materials are included in the table for comparative purposes. Note that the properties of NC132 are those measured by the current authors and that the four-point bending strengths of NC350 (ref. 14) and HPSN (ref. 15) were converted to the "equivalent" ball-on-ring strengths by increasing measured strengths by 11%. It is evident from these results that the mechanical properties of the SiH_4-derived RBSN are equal to

or exceed those of commercial RBSN (NC350) made from traditional Si powders. Most dramatic is the fact that the average strength of the SiH_4-derived RBSN is over 75% greater. These differences in mechanical properties are even more significant when it is considered that the density of the SiH_4-derived RBSN is about 10% less than the commercial RBSN. The fine-scale microstructure of this SiH_4-derived RBSN suggests that flaw sizes can be potentially reduced to values of the order of 0.1 to 0.25 μm; thereby, increasing the strength even further.

Since fracture toughness and strength of HPSN vary directly with the β-Si_3N_4 content,[15] the values for the SiH_4-derived RBSN are compared in Table 1 with those of a fully dense HPSN where the major phase is α-Si_3N_4. It can be seen that relative to density, the toughness and strength of the SiH_4-derived RBSN essentially equal those of the HPSN; on a specific density basis, they are superior. These results emphasize that by careful processing of high purity, small diameter powders, strength-controlling flaws do not have to scale with porosity. The properties of NC132 are greater then those of the SiH_4-derived RBSN even on a relative to density basis; however, direct comparison is not possible since NC132 contains β-Si_3N_4 as the major phase, not α-Si_3N_4 as is the case for RBSN.

To further substantiate the fracture toughness value for the SiH_4-derived RBSN, the fracture strength (σ_f) of all the samples (both those with

and without optimum processing) was correlated with the size and shape of the strength-controlling processing flaw by:[16]

$$\sigma_f = \frac{Z}{Y} \frac{K_c}{\sqrt{\pi a}} \tag{3}$$

where Y is a geometric constant (1.07 for the bending test fixture used in this study), Z is a constant related to the ellipticity of the flaw, and "a" is the depth of the flaw. Therefore, a plot of σ_f vs. $Z/(Y\sqrt{\pi a})$ gives a curve whose slope is K_c. Since the term $Z/(Y\sqrt{\pi a})$ contains both the crack depth and flaw shape, it is a measure of the severity of the strength-controlling defect. Figure 1 summarizes these results. Not all the fracture origins of the samples could be identified, especially those with strengths greater than 500 MPa. A regression line through the data gives a toughness value of 2.7 ($\pm$ 0.6) MPa $m^{1/2}$ which is in good agreement with that determined from the Vickers indentation technique.

In addition to the mechanical properties, the oxidation resistance of this SiH_4-derived RBSN was determined at 1250°C in flowing air.[5,6] Porz and Thummler[17] showed that at the same temperature, low density silicon nitride samples undergo significant internal oxidation before saturation is attained; however, internal oxidation could be reduced to less than 1% due to pore closure by the oxide for densities >85% and Hg porosimetry pore diameters <0.12 μm. For SiH_4-derived RBSN the extent of oxidation at 1250°C was less than 1% for specimens having densities of 76.5%. This superior

oxidation resistance at lower densities very likely results from the high purity combined with the extremely small channel size (0.01 to 0.06 μm) that allows for pore sealing at densities much lower than for conventional RBSN.

SUMMARY

The fabrication of 76% dense RBSN samples from nitriding laser-synthesized silicon powder have resulted in average strengths that are over 75% greater than samples made from traditional Si powder with toughness and hardness being about 10% greater. The specific strength and toughness of this SiH_4-derived RBSN are superior to that of α-HPSN. Oxidation resistance of this SiH_4-derived RBSN is also significantly better than conventional RBSN. These superior properties result from achieving a fine microstructure coupled with decreasing the largest pore size to below 15 μm. Most importantly, these results reveal largely unexplored opportunities for other processes and materials that are capable of achieving highly perfect microstructures in bodies that need not be fully dense. Other possibilities include different reaction-bonded, polymer derived, and vapor infiltrated ceramic materials.

ACKNOWLEDGMENTS

This research was supported by two industrial consortia. One includes ABEX, Aisin Seiki Co., Alcoa, NGK Spark Plug Co., Nippon Steel, Sumitomo Electric Industries Ltd., The Japan Steel Works, Ltd., and Toa Nenryo Kogyo K.K. The

second includes Caterpillar Tractor, Cummins Engine Co., Deer, Inc., General Motors, TRW Valve Division, and Rhone Poulenc.

REFERENCES

1. A.J. Moulson, "Review: Reaction Bonded Silicon Nitride: Its Formation and Properties," J. Mater. Sci., 14, 1017-1051 (1979).

2. M.L. Torti, R.A. Alliegro, D.W. Richerson, M.E. Washburn, and G.Q. Weaver, "Silicon Nitride and Silicon Carbide for High Temperature Engineering Applications," Proc. Brit. Ceram. Soc., 22, 129-147 (1973).

3. S.C. Danforth and J.S. Haggerty, "Mechanical Properties of Sintered and Nitrided Laser-Synthesized Silicon Powder," J. Am. Ceram. Soc., 66, (4), C-58-59 (1983).

4. J.S. Haggerty, G. Garvey, J-M. Lihrman, and J.E. Ritter, "Processing and Properties of Reaction Bonded Silicon Nitride Made from Laser Synthesized Silicon Powders," pp. 51-62 in Defect Properties and Processing of High Technology Nonmetallic Materials, MRS Proceedings, Vol. 60, Pittsburgh (1986).

5. J.S. Haggerty, J.H. Flint, G. Garvey, J-M Lihrman and J.E. Ritter, "High Strength, Oxidation Resistant Reaction Bonded Silicon Nitride Made from Laser-Synthesized Silicon Powder," pp. 147-54 in Proc. 2nd Int. Sym. Ceramic Materials and Components for Engines, eds. W. Bumk and H. Hausner, Gerlag Deutsche Keramische Gesellsehaft, Lubeck-Travemunde, W. Germany (1987).

6. J.S. Haggerty, G.J. Garvey, J.H. Flint, B.W. Sheldon, M. Aoki, M. Okuyama, J.E. Ritter, and S.V. Nair, "Processing and Properties of Reaction Bonded Silicon Nitride and Silicon Carbide Made From Laser Synthesized Powders," to be published in Proc. of Basic. Sci. Div., Am. Ceram. Soc., Orlando, Fla. (1987).

7. G.R. Anstis, P. Chantikul, B.R. Lawn, and D.B. Marshall, "A Critical Evaluation of Indentation Techniques for Measuring Fracture Toughness: I Direct Crack Measurements," J. Am. Ceram. Soc., 64, (9) 533-38 (1981).

8. D.B. Marshall, T. Noma, and A.G. Evans, "A Simple Method for Determining Elastic Modulus to Hardness Ratios Using Knoop Indentation Measurements," J. Am. Ceram. Soc., 65 (10) C175 (1982).

9. D.K. Shetty, A.R. Rosenfield, P. McGuire, G.K. Bansal, and W.H. Duckworth, "Biaxial Flexure Tests for Ceramics," Am. Ceram. Soc. Bull., 59 (12), 1193-97 (1980).

10. Dr. Joseph Patchett, Norton Co., Niagara Falls, Ontario, Canada, personal communication.

11. R.M. Williams and L.R. Swank, "Use of Weibull Statistics to Correlate MOR, Ball-on-Ring, and Rotational Fast Fracture Tests," J. Am. Ceram. Soc., 66 (11), 765-68 (1983).

12. W.A. Dunlay, "Mechanical Properties of Laser Synthesized Reaction Bonded Silicon Nitride," M.S. Thesis, University of Massachusetts, Amherst (1987).

13. J. Heinrich and D. Muntz, "Strength of Reaction-Bonded Silicon Nitride with Artificial Pores," J. Am. Ceram. Soc., 59 (12), 1221-22 (1980).

14. S.C. Danforth and M.H. Richman, "Strength and Fracture Toughness of Reaction-Bonded Si_3N_4," Am. Ceram. Soc. Bull., 62, (4), 501-504 (1983).

15. G. Himsolt, H. Knoch, H. Huebner, and F.W. Kleinlein, "Mechanical Properties of Hot-Pressed Silicon Nitride with Different Grain Structures," J. Am. Ceram. Soc., 62 (1-2), 29-32 (1979).

16. G.K. Bansal, "Effect of Flaw Shape on Strength of Ceramics," J. Am. Ceram. Soc., 59 (1-2), 87-88 (1979).

17. E. Porz and F. Thummler, "Oxidation Mechanisms of Porous Silicon Nitride," J. Mater. Sci., 19, 1283-95 (1984).

Table 1. Summary of Mechanical Properties

Property	Material			
	SiH_4-originating RBSN	NC350 (Ref.14)	HPSN (Ref. 15)	NC132
Phase Composition (α/β)	90/10	90/10	90/10	20/80
Nitrided Density (% Si_3N_4 Theo.)	76 (1.2)†	83	100	100
Hardness (GPa)	8.9 (0.5)	8.3	--	18.5
Toughness (MPa $m^{1/2}$)	2.3 (0.3)	2.3	2.72#	4.0 (0.2)
Strength (MPa)	531 (64)	302	523*	945 (60)

†Number in parentheses represents ± one standard deviation.

#Obtained from extrapolating the toughness data where α/β compositions ranged from 85/15 to 0/100.

*Strength for an α/β ratio of 60/40 which was the lowest β fraction strength tested.

Figure 1. Fracture strength of SiH_4-originating RBSN (76% dense) as a function of the severity of the strength-controlling defect.

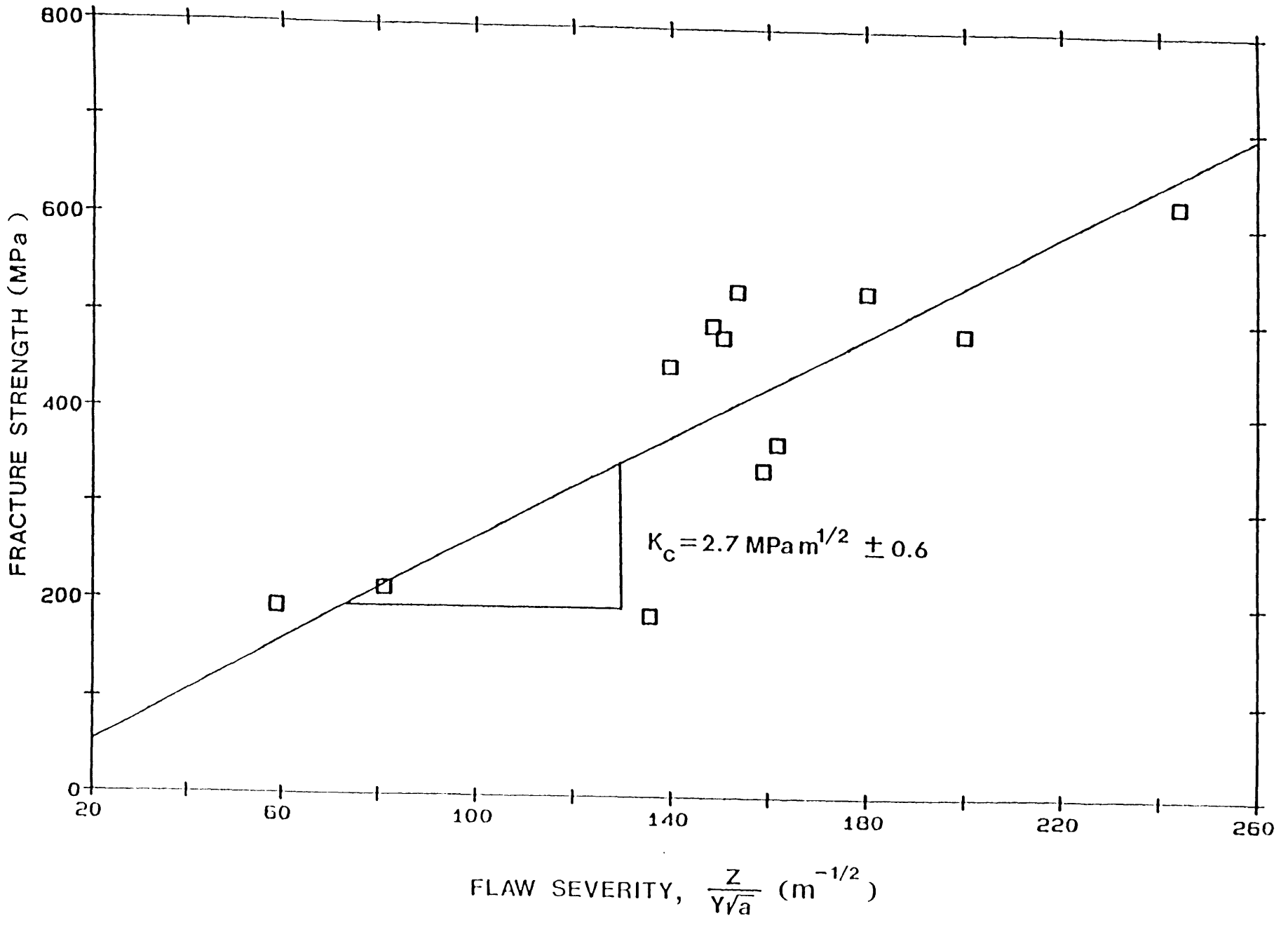

To be published in the Proceedings of the 12th Annual Conference on Composites and Advanced Ceramics, Engineering Ceramics Division Meeting, American Ceramic Society, Cocoa Beach, Florida, January 1988 P88-03

PROPERTIES OF REACTION BONDED SILICON NITRIDE MADE FROM HIGH PURITY SILICON POWDER

J. S. Haggerty and A. Lightfoot
Massachusetts Institute of Technology
Cambridge, MA

J. E. Ritter, S. V. Nair and P. Gennari
University of Massachusetts
Amherst, MA

ABSTRACT

Unique processing permits fabrication of RBSN samples containing exceptionally small defects. These samples nitride to completion in less than 1 h at 1400°C and exhibit average room temperature strengths of 531 MPa for 76% dense RBSN as well as excellent toughness and hardness characteristics. Room temperature strengths of as-processed samples are related to flaw size and shape by a fracture mechanics model. To determine oxidation resistance, samples were heat-treated in air for 1 and 50 h at 1000 and 1400°C and their weight gain and room-temperature strengths were measured. These weight-gain and strength results for RBSN are compared to those of HPSN.

INTRODUCTION

Nitriding extremely fine (about 0.3 μm diameter) silicon powder synthesized from laser heated SiH_4 results in an RBSN of high purity and fine microstructure.[1-3] The objective of the present research was to show that this high quality microstructure results in superior mechanical properties and oxidation resistance.

EXPERIMENTAL PROCEDURE

The detailed techniques used to produce the RBSN samples are described elsewhere.[1-3] Briefly, the SiH_4-originating Si powder is dispersed in methanol solution and disc shaped specimens are formed by colloidal pressing. The samples are cold isostatically pressed and then nitrided at 1420°C for 1 h. The tensile surface of the sample (12.7 mm diameter by 1 mm thick) is diamond polished to a 1 μm finish. Hardness and fracture toughness was measured with a Vickers indenter.[4] Fracture strength was determined by a ball-on-ring test.[5] In addition, samples were oxidized in air at 1000 and 1400°C for 1 and 50 h. After oxidation, strength and weight gain were measured.

RESULTS AND DISCUSSION

The samples have a porosity of 23.5% and X-ray analysis showed 90% α-Si_3N_4 and balance β-Si_3N_4. Nitride crystal sizes are 0.028 μm for α and 0.033 μm for β. The nitride phase is a continuous network with solid phase dimensions 0.2 to 0.7 μm. Hg porosimetry pore neck diameters are between 0.010 to 0.060 μm. Micrographs reveal occasional 5-15 μm isolated pores.

Table 1 summarizes the mechanical testing results for the SiH_4-originating RBSN. These results are based on an average from 8 samples. RBSN (NC350) and HPSN (NC132) are included in the table for comparison. Note that the properties of NC132 are those measured by the current authors. It is evident from these results that the mechanical properties of the SiH_4-originating RBSN are equal to or exceed those of NC350. Most dramatic is the fact that the average strength of the SiH_4-originating RBSN is over 75% greater. It is important to note that these high strengths for SiH_4-originating RBSN correspond to an average semi-circular flaw size of about 10 μm,[7] which is consistent with the observed, isolated pores of 5-15 μm diameter that exist in the structure. Although the properties of NC132 are not directly comparable since NC132 contains β-Si_3N_4 as the major phase, the strength of NC132 relative to its toughness is less than that of the SiH_4-originating RBSN.

To further substantiate the fracture toughness value for the SiH_4-originating RBSN, the fracture strength (σ_f) of samples with and without

optimum processing was correlated with the size and shape of the strength-controlling flaw by:[7]

$$\sigma_f = \frac{Z}{Y} \frac{K_C}{\sqrt{\pi a}} \qquad (1)$$

where Y is a geometric constant (1.07 for the bending fixture used in this study), Z is a constant related to the ellipticity of the flaw, and a is the depth of the flaw. Figure 1 summarizes the strength results. A regression line through the data gives a toughness value of 2.7 ($\pm$ 0.6) MPa $m^{1/2}$ which is in good agreement with that determined from the Vickers indentation technique.

The weight gain results of the oxidation experiments are given in Fig. 2 along with the results reported by others for RBSN[8] and HPSN.[9] The SiH_4-originating RBSN exhibits approximately two orders of magnitude lower weight gain than results for two more dense RBSN materials[8] and up to an order of magnitude better behavior than HPSN.[9] Although the results have not been analyzed mechanistically, it would appear that the same superior microstructural features that give high strengths in the SiH_4-originating RBSN also give it improved oxidation resistance relative to the more dense RBSN.[8] Average oxidation rates of the SiH_4-originating RBSN decrease with exposure time at both 1000 and 1400°C, indicating the formation of protective barriers to internal oxidation. The barriers form rapidly when large diameter channels into the interior of the samples are eliminated through careful processing with highly perfect powders.

The strength results of the oxidation experiments are given in Fig. 3 for both RBSN and HPSN. Short-term oxidation at 1000°C increases the strength of as-machined HPSN samples due to the formation of a glassy phase on the surface that tends to smooth out the pre-existing machining flaws.[10] More extensive, long-term oxidation at 1400°C causes surface pits to form, resulting in a sharp strength decrease.[10] On the other hand, oxidation of the SiH_4-originating RBSN at either 1000 or 1400°C causes no significant strength changes within experimental scatter. These results are consistent with the superior oxidation resistance of this material. These results also indicate that the glassy phase that forms during the initial stages of oxidation has little effect on the severity of the strength-controlling pores in RBSN. This is quite contrary to the smoothing out of the machining flaws on HPSN.

ACKNOWLEDGMENTS

This research was supported by two industrial consortia. One includes ABEX, Aisin Seiki Co., Alcoa, NGK Spark Plug Co., Nippon Steel, Sumitomo Electric Industries Ltd., The Japan Steel Works, Ltd., and Toa Nenryo Kogyo K.K. The second includes Caterpillar Tractor, Cummins Engine Co., Deer, Inc., General Motors, TRW Valve Division, and Rhone Poulenc. The authors are also grateful to Charles Lewinsohn for making samples with unusual care.

REFERENCES

1. J.S. Haggerty, G. Garvey, J-M. Lihrman, and J.E. Ritter, "Processing and Properties of Reaction Bonded Silicon Nitride Made from Laser Synthesized Silicon Powders," pp. 51-62 in Defect Properties and Processing of High Technology Nonmetallic Materials, MRS Proceedings, Vol. 60, Pittsburgh (1986).

2. J.S. Haggerty, J.H. Flint, G. Garvey, J-M Lihrman and J.E. Ritter, "High Strength, Oxidation Resistant Reaction Bonded Silicon Nitride from Laser-Synthesized Silicon Powder," pp. 147-54 in Proc. 2nd Int. Sym. Ceramic Materials and Components for Engines, eds. W. Bunk and H. Hausner, Gerlag Deutsche Keramische Gesellsehaft, Lubeck-Travemunde, W. Germany (1987).

3. J.S. Haggerty, G.J. Garvey, J.H. Flint, B.W. Sheldon, M. Aoki, M. Okuyama, J.E. Ritter, and S.V. Nair, "Processing and Properties of Reaction Bonded Silicon Nitride and Silicon Carbide Made From Laser Synthesized Powders," to be published in Proc. of Basic. Sci. Div., Am. Ceram. Soc., Orlando, Fla. (1987).

4. G.R. Anstis, P. Chantikul, B.R. Lawn, and D.B. Marshall, "A Critical Evaluation of Indentation Techniques for Measuring Fracture Toughness: I Direct Crack Measurements," J. Am. Ceram. Soc., 64, (9) 533-38 (1981).

5. D.K. Shetty, A.R. Rosenfield, P. McGuire, G.K. Bansal, and W.H. Duckworth, "Biaxial Flexure Tests for Ceramics," Am. Ceram. Soc. Bull., 59 (12), 1193-97 (1980).

6. S.C. Danforth and M.H. Richman, "Strength and Fracture Toughness of Reaction-Bonded Si_3N_4," Am. Ceram. Soc. Bull., 62, (4), 501-504 (1983).

7. G.K. Bansal, "Effect of Flaw Shape on Strength of Ceramics," J. Am. Ceram. Soc., 59 (1-2), 87-88 (1979).

8. F. Porz and F. Thummler, "Oxidation Mechanism of Porous Silicon Nitride," J. Mat. Sci., 19, 1203-95 (1984).

9. D. Cubicciotti and K.H. Lau, "Kinetics of Oxidation of Hot-Pressed Silicon Nitride Containing Magnesia," J. Am. Ceram. Soc., 61 (11-12), 512-17 (1978).

10. K. Jakus, J.E. Ritter, and W.P. Rogers, Strength of Hot-Pressed Silicon Nitride After High-Temperature Exposure," J. Am. Ceram. Soc., 67 (7), 471-75 (1984).

Table 1. Summary of Mechanical Properties

Property	Material		
	SiH_4-originating RBSN	NC350 (Ref. 6)	HPSN NC132
Phase Composition (α/β)	90/10	90/10	20/80
Nitrided Density (% Si_3N_4 Theo.)	76	83	100
Hardness (GPa)	8.9 (0.5)[+]	8.3	18.5
Toughness (MPa $m^{1/2}$)	2.3 (0.3)	2.3	4.0 (0.2)
Strength (MPa)	531 (64)	302	945 (60)

[+]Number in parentheses represents $\pm$ one standard deviation.

Figures

Figure 1. Fracture strength of SiH_4-originating RBSN (76% dense) as a function of the severity of the strength-controlling defect.

Figure 2. Weight gain after high temperature exposures in air. (Refs. 8 and 9)

Figure 3. Relative strength change after high temperature exposures in air.

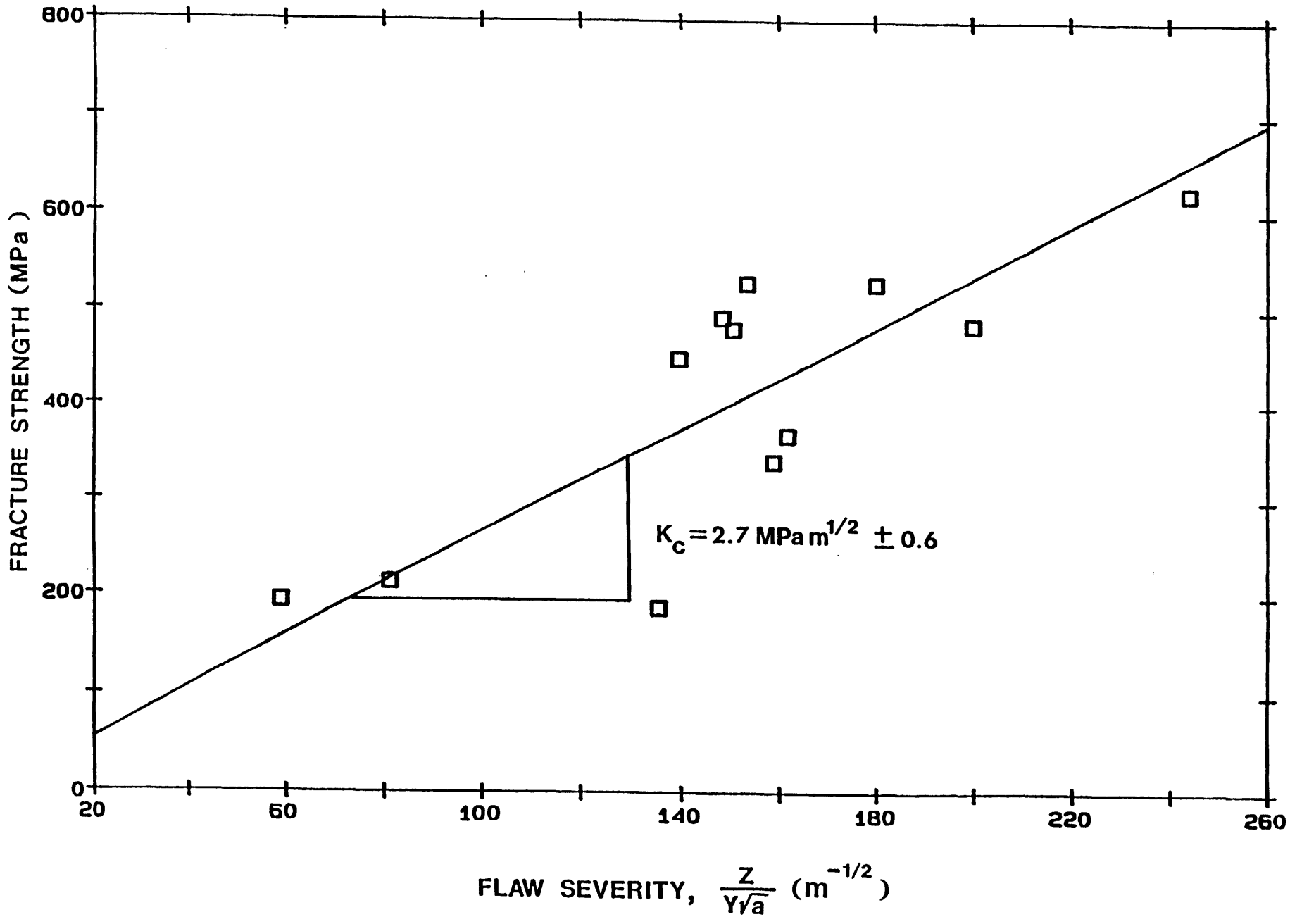
800
600
400
200
0
20
60
100
140
180
220
260
FRACTURE STRENGTH (MPa)
FLAW SEVERITY, $\frac{Z}{Y\sqrt{a}}$ ($m^{-1/2}$)
$K_c = 2.7$ MPa $m^{1/2}$ $\pm$ 0.6

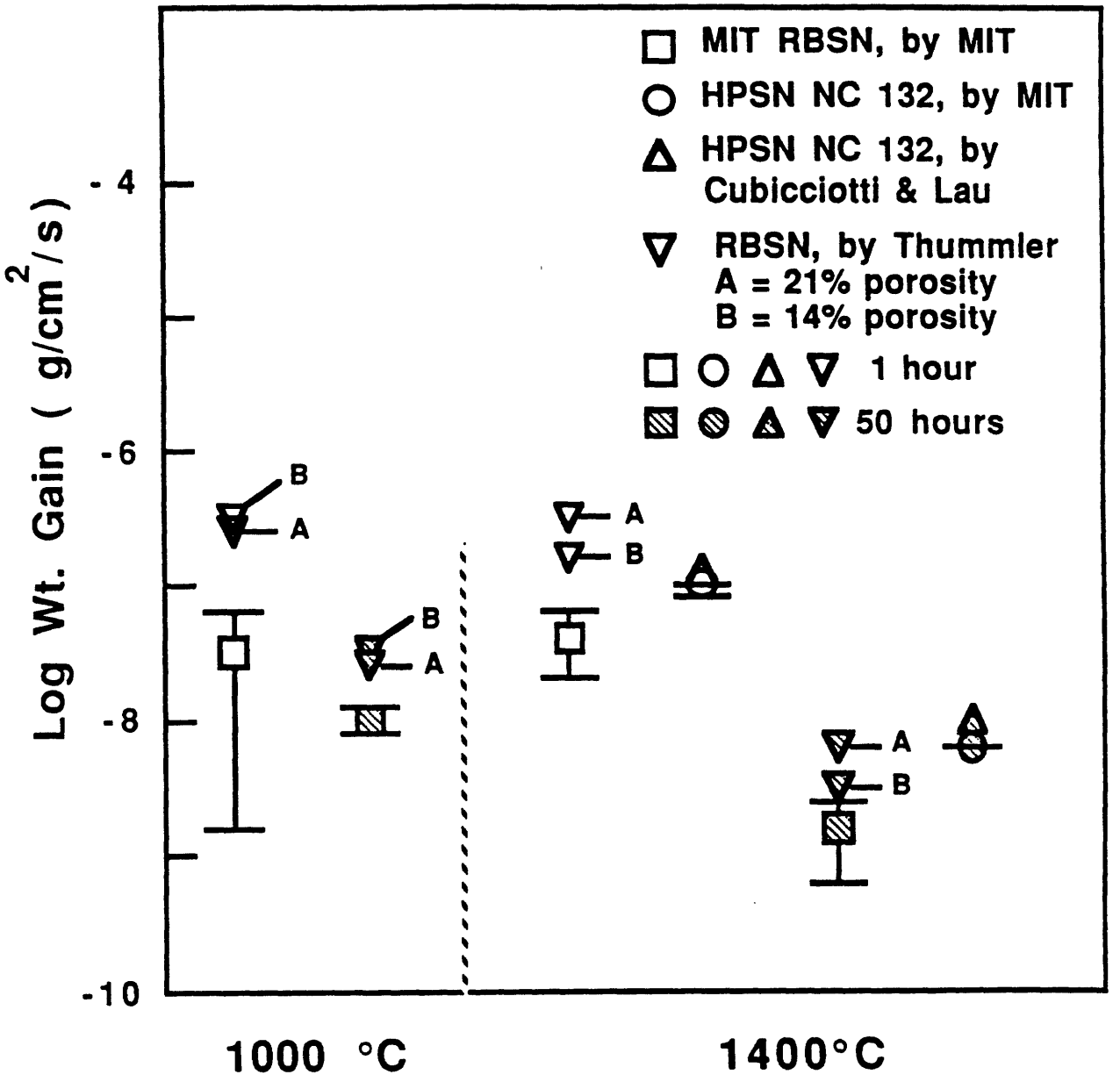

Oxidation of Silicon Nitride

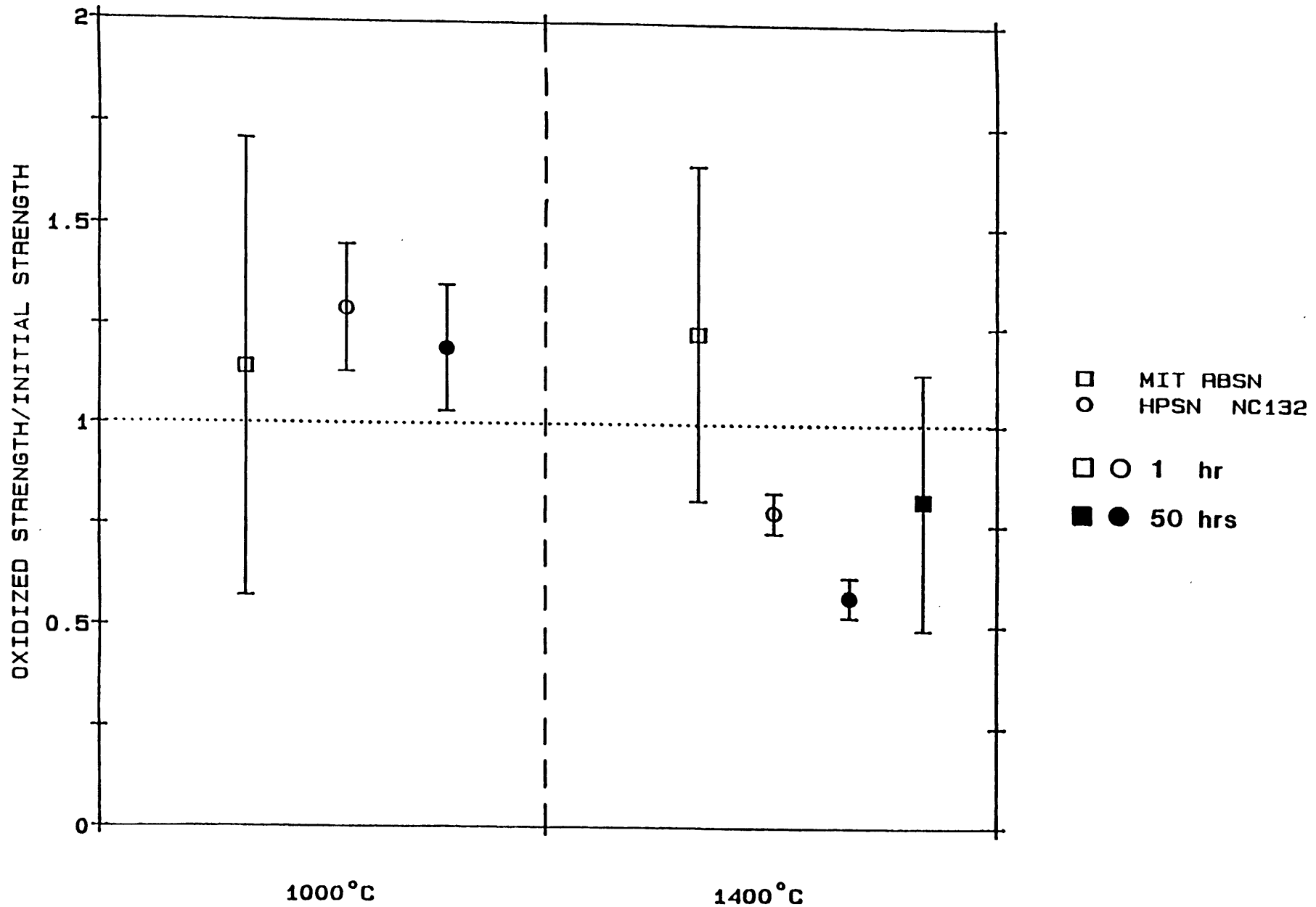
OXIDIZED STRENGTH/INITIAL STRENGTH
2
1.5
1
0.5
0
1000°C
1400°C
MIT RBSN
HPSN NC132
1 hr
50 hrs

Reprinted from the Journal of the American Ceramic Society, Vol. 68, No. 2, February 1985
Copyright 1985 by The American Ceramic Society
J. Am. Ceram. Soc., 68 [2] 81–85 (1985)

Surface Tensions of Alumina-Containing Liquids

J. M. LIHRMANN* and J. S. HAGGERTY*

Massachusetts Institute of Technology, Cambridge, Massachusetts 02139

The surface tensions of CO_2-laser-melted alumina-containing liquids have been measured by a static, pendant-drop technique in air, helium, and a 90% helium-10% hydrogen mixture. The influences of up to 10 wt% Cr_2O_3, MgO, and TiO_2 have been studied. Surface tension data are also reported throughout the whole concentration range between liquid alumina and zirconia in air. A new analytical technique based on comparing calculated and observed melt contours is reported. Using this technique, more precise surface tension to density ratios can be determined from low length to diameter ratio pendant drops than by previously reported procedures.

I. Introduction and Background

EXCEPT for those dealing with salts and glasses, relatively little data[1–5] exist for the physical and chemical properties of liquid ceramics. This paper reports static surface tensions of alumina-containing melts measured by the pendant-drop technique. The systems Al_2O_3-Cr_2O_3, Al_2O_3-MgO, Al_2O_3-TiO_2, and Al_2O_3-ZrO_2 were selected because they represent commercially important and technically interesting alumina-based ceramics.

Broken and distorted bonds between atoms at the liquid-vapor interface cause an excess energy defined as the surface energy. For incompressible liquids, the surface energy is equal to the surface tension because surface stresses are relieved by viscous flow. The surface tension causes a pressure difference, ΔP, across a curved interface,[6–7] defined by

$$\Delta P = \gamma(1/R_1(z) + 1/R_2(z)) \tag{1}$$

where γ is the surface energy or tension of the liquid-vapor interface and R_1 and R_2 are the principal radii of curvature of the interface at an altitude z. The internal pressure within a fluid body having a density ρ varies with altitude as ρgz; the changing pressure causes the local shape to vary accordingly.

The drop shape is used to define the surface tension in the pendant-drop technique. Figure 1 shows the pendant-drop geometry and Eq. (2) defines the analytical relationship between the liquid properties and pendant-drop shape

$$2\gamma/b - \gamma(1/R_1(z) + 1/R_2(z)) = \rho gz \tag{2}$$

where b is the drop radius at $z = 0$. Pendant-drop shapes can be analyzed using the differential form of Eq. (2)

$$\left(\frac{\rho gb^2}{\gamma}\right)\left(\frac{z}{b}\right) = 2 - b\left[\frac{d^2z/dr^2}{(1 + (dz/dr)^2)^{3/2}} + \frac{dz/dr}{r(1 + (dz/dr)^2)^{1/2}}\right] \tag{3}$$

This second-order, nonintegratable differential equation contains two parameters, b and

$$\beta \equiv -\rho gb^2/\gamma \tag{4}$$

whose values define the size and the shape of the pendant drop represented by Eq. (3). β is also used to characterize sessile drops; but it is positive for this case.

Historically, Bashforth and Adams[8] were the first to obtain numerical solutions of Eq. (3). They tabulated a large number of r/b and z/b solutions that are accurate to five significant figures for values of β ranging from -0.1 to 100. However, their tables, and similar ones,[9,10] have not been used extensively because they require an accurate experimental determination of b.

This last point encouraged others[11–13] to develop an analytical procedure that avoids an actual determination of b. In these, size is gauged by the equatorial radius, r_e, and shape, S, by the ratio of the drop radii at two different horizontal planes, $r_s/r_e \equiv S$; conventionally, r_s is measured at an altitude $2r_e$ from the bottom of the drop (Fig. 1). These solutions for the pendant-drop shape rearrange Eq. (4) as

$$\frac{\gamma}{\rho g} = -\frac{b^2}{\beta} = -\frac{1}{\beta}\frac{r_e^2}{(r_e/b)^2} = \frac{4r_e^2}{H} \tag{5}$$

to define a new term $H = -4\beta(r_e/b)^2$. Values of H have been calculated[11–13] and tabulated as a function of S. By this procedure, γ/ρ is determined simply by measuring r_e and r_s and deriving the corresponding H value from published tables.

Although this procedure is potentially more accurate since it eliminates the necessity of measuring b, the γ/ρ values are still subject to considerable error since the calculation depends on the precise determination of r_s measured at an altitude $2r_e$. Stauffer[14]

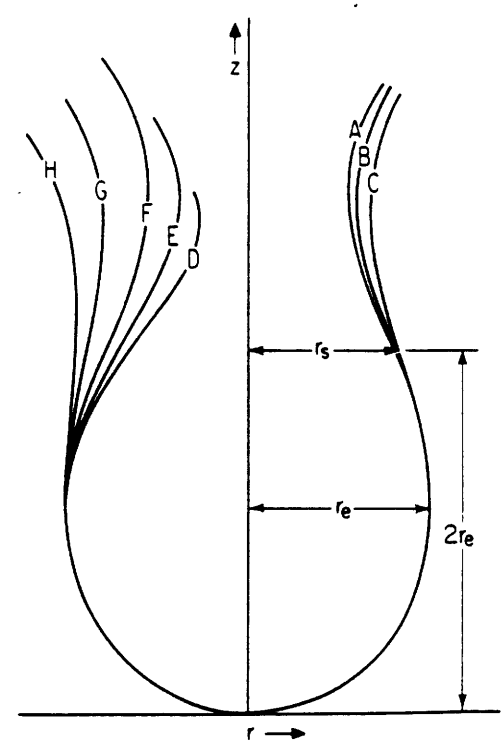

Fig. 1. Pendant-drop shapes computed for a constant r_e value are shown. Curves D through H, in that order, correspond to β values (Eq. (3)) of -0.25, -0.31, -0.37, -0.475, and -0.55. Curves A, B, and C, although defined by very close values of $S = r_s/r_e$, are almost indistinguishable at $z = 2r_e$; however, they correspond to γ/ρ values as different as 21.4, 20.1, and 18.7 $\mu J \cdot cm/g$, respectively.

Presented at the 85th Annual Meeting and Exposition, The American Ceramic Society, Chicago, IL, April 26, 1983 (Basic Science Division, Paper No. 109-B-83). Received April 16, 1984; revised copy received October 1, 1984; approved October 10, 1984.

Supported by ONR and ARO under Contract No. N0014-82-K0350 and the French Government by a salary grant.

*Member, the American Ceramic Society.

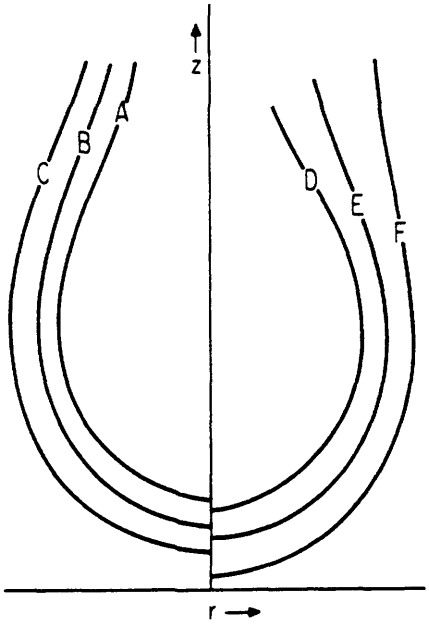

Fig. 2. Nonlinear aspects of Eq. (3) are illustrated. Parallel curves like *A*, *B*, and *C* correspond to very different γ/ρ values (μJ·cm/g) of 19.04, 25.37, and 35.25, respectively, whereas nonparallel contours *D*, *E*, and *F* define similar values of γ/ρ, i.e., 24.95, 25.37, and 25.82.

analyzed the errors expected using this analytical procedure. Assuming a 1% measurement error, he showed that the uncertainty of γ/ρ is 20% for $S = 0.4$, while it decreases to 2.6% for $S = 0.85$. The extreme sensitivity of the technique to measurement errors is evident from the small differences in the positions of curves *A*, *B*, and *C* in Fig. 1 at an altitude $z = 2r_e$. Also, it should be noted that *H* values tabulated by different authors[11,12] differ by several percent.

The use of higher length to diameter ratios improves the precision because the pendant-drop contours separate from one another as shown in Fig. 1. The accuracy also improves because the actual pendant-drop shape is less subject to distortions caused by noncircular cross sections of the solid rods, nonplanar solid-liquid interfaces and non-freely-hinging solid-liquid interfaces. Many authors[12-15] recommend using pendant-drop lengths that exceed 3.0 to $4.0r_e$.

We found this procedure gave unacceptable accuracy with the oxide melts investigated because pendant-drop lengths in excess of 2.2 to $2.6r_e$ could not be achieved with the γ/ρ values characteristic of this work. Rayleigh instability caused the pendant drops to form necks that collapsed when drop length to r_s ratios exceeded a critical value ($\approx$2.5), apparently related to the zone-height instabilities[16] found for floating-zone crystal growth between unequal rod diameters. Longer drop lengths require lower γ/ρ values. Also, we were not able to reliably measure r_s and r_e values with 1.0% precision because of the combined effects of an absence of a sharp image boundary caused by optical flare and uncertain boundary positions caused by vibrations that were characteristic of these high-temperature melts.

II. Analytical Procedure

Because established procedures did not permit γ/ρ's to be determined with adequate precision for the low length to diameter ratios characteristic of these oxide pendant drops, we considered other means of analyzing the shapes of the liquids. We found that it was possible to distinguish between observed melt shapes and melt shapes computed from Eq. (3) with small incremental changes in assumed γ/ρ values. When the comparisons were made over the entire pendant-drop contours, measurement errors appeared acceptable even with the low length to diameter ratios.

Table I. Impurities in Constituent Powders Detected by Semiquantitative Plasma Emission Technique

Elemental contaminant (ppm by wt)	Constituent powder					
	Al_2O_3	Cr_2O_3	MgO	TiO_2	Y_2O_3	ZrO_2
Al	Maj	200	50	300	200	200
Ba	ND	20	ND	ND	ND	30
Ca	50	80	300	70	50	300
Cr	10	Maj	30	ND	10	ND
Fe	50	100	200	100	50	80
Mg	ND	10	Maj	300	30	100
Ni	ND	ND	10	ND	50	ND
Si	100	100	200	400	100	200
Ti	ND	ND	ND	Maj	ND	ND
Y	ND	ND	ND	ND	Maj	ND
Zr	ND	ND	ND	ND	ND	Maj
Hf	ND	ND	ND	ND	ND	12 000

NOTE: ND = not detected.

The procedures used to calculate the pendant-drop shapes followed those given in Refs. 17 to 19. The entire contour is defined by the assumed r_e and β values; β is defined by r_e/b. For an assumed r_e value, a family of contours was generated as a function of *b*. Typical contours, *A* to *H*, are shown in Fig. 1 for a particular value of r_e. Iteration over a range of r_e values provided a complete set of curves, each of which correspond to a specific b^2/β; Eq. (4) is used to calculate γ/ρ for the best fitting curve. For this study, 300 theoretical contours were computed for 15 values of r_e ranging from 2.17 to 4.07 mm and 20 values of β ranging from -0.25 to -0.55. The average incremental γ/ρ between curves was approximately 1%.

It is important that the observed and calculated contours be the same over their entire lengths. Figure 1 illustrates the expected shapes for constant r_e values with different γ/ρ values. Curves *A* to *C* of Fig. 2 illustrate the error in γ/ρ resulting from selecting a contour that parallels the observed pendant-drop shape. Curves *D* to *F* of Fig. 2 illustrate that the pendant-drop shapes are in fact quite a strong function of r_e for similar γ/ρ values. With a little practice, it is possible to distinguish between matching and incorrect contours.

III. Experimental Procedure

Experimentally, melts were created on the bottom ends of polycrystalline feed rods in a controlled-atmosphere chamber. The incandescent melts were projected with a single lense (20× magnification) onto a surface where they were compared with calculated contours.

Heating was accomplished with four 10.6-μm wavelength beams of light that orthogonally impinged onto the melts in a radial direction. The light source was a 1350-W CO_2 laser custom designed to emit two beams. Each of the emitted beams was divided into two beams with roof prisms. The beam dimensions on the melt surfaces were controlled by the relative positions of the focusing lenses and the melt. Typical spot diameters equaled the feed-rod diameters.

Laser heating is particularly applicable to high-temperature materials. The laser has no characteristic temperatures to set maximum temperature limits. Also, ambient atmospheres can be selected without serious restrictions.

Feed rods were isostatically pressed from powders batched to the desired overall compositions with mixtures of Al_2O_3,* Cr_2O_3,† MgO,‡ TiO_2,§ and ZrO_2¶ powders. The purities of these are sum-

*Lot No. 1115/17, Meller Co., Providence, RI.
†Batch No. S87633B, Johnson Mathey Chemicals Ltd., Royston, Hartfordshire, England.
‡Lot No. 703653, Fisher Scientific Co., Pittsburgh, PA.
§Lot No. 725845, Fisher Scientific Co.
¶Lot No. P 82, Zircar Products Inc., Florida, NY.

marized in Table I. Nominally 3-mm-diameter rods were sintered for 12 h at 1200°C, typically producing a 65% dense, 10-μm grain size rod. Further densification occurred over a distance of nominally one rod diameter when they were melted. No material was withdrawn from the melts onto the feed rods during the experiment, so the melt compositions were not changed from the batch compositions by segregation effects. With the exception of the high ZrO_2 compositions, vaporization losses were negligible and thus did not cause compositional changes.

The relative beam positions on the melts and beam powers were adjusted to make the solid-liquid interfaces as flat as possible. When properly adjusted, the altitude of the solid-liquid interface was uniform within ±0.05 mm. Shaft rotation flattened the interface further but could not be used effectively in surface tension measurements because vibrations made the drop shape uncertain and severely limited the maximum drop length that could be achieved before it fell from the feed rod.

Temperatures of the molten pendant drops were measured pyrometrically. Absolute temperature measurements are imprecise because the melts are transparent. However, they do provide a reasonable measure of temperature gradients within the pendant drops. Some superheating[22,23] occurred where the laser beams intersected the melts. By expanding the beam diameters to equal the feed diameters, the radiant flux onto the melt surfaces was made as uniform as possible. This adjustment combined with the action of a spherical radiation shield positioned to refocus reflected and emitted radiation on the center of the melts minimized the superheat[28] to ≈30°C. Free convection in the melt acted to reduce temperature gradients and ensure compositional uniformity. Direct observation by telescope and experience with floating zone crystal growth from similar melts indicated that the pendant drops were completely molten.

The chamber was operated open for an air atmosphere. For the other atmospheres, the chamber was evacuated to a pressure of 2.7 Pa and backfilled with the desired gases twice before conducting the experiments. All experiments were conducted at 98 kPa pressure with static gas conditions. The initial air atmosphere was 21°C and 70% humidity. The 90% He-10% H_2 gas** contained 6 ppm O_2 and 12 ppm $H_2O(g)$; equilibrium oxygen and water vapor pressure concentrations at 2000°C are 5.4×10^{-2} and 24.9 ppm, respectively. The He gas†† contained 1.5 ppm O_2 as measured by a ZrO_2 electrolyte.

The maximum length to diameter ratio that could be achieved was determined by progressively increasing melt volumes until the melts dropped. Measurements were made with nearly maximum volume drops. The final S values were ≈0.85. Generally, each reported data point represents an average of five measurements.

IV. Results

Conversion of γ/ρ measurements into γ values requires knowledge of the melt densities. For pure liquid alumina, reported densities[1,20,21,24,25,27] at the melting point range from 2.51 to 3.05 g/cm³. We adopted the more recent and accepted value[1,27] of 3.01 g/cm³. Except[5] for Cr_2O_3, the densities of the other liquid oxides have not been characterized experimentally. We estimated the densities using average values of the solid thermal expansion coefficients between room temperature and the melting points, and an assumed 20.4% volume expansion upon melting.[3] The liquid densities of the binary mixtures were approximated assuming a linear variation of the liquid density with the molar concentration of each species. The density values used to determine the surface tensions are shown in Fig. 3. They are also given in Table II together with the estimated temperatures of the corresponding melts.

The measured surface tension results for the systems Al_2O_3-Cr_2O_3, MgO, Al_2O_3-TiO_2, and Al_2O_3-ZrO_2 in each of the three atmospheres investigated are shown in Figs. 4 and 5. The γ axes were truncated to expand the scales. The Al_2O_3-ZrO_2 results were plotted separately from the others taken in an air atmosphere because the range of investigated compositions was wider.

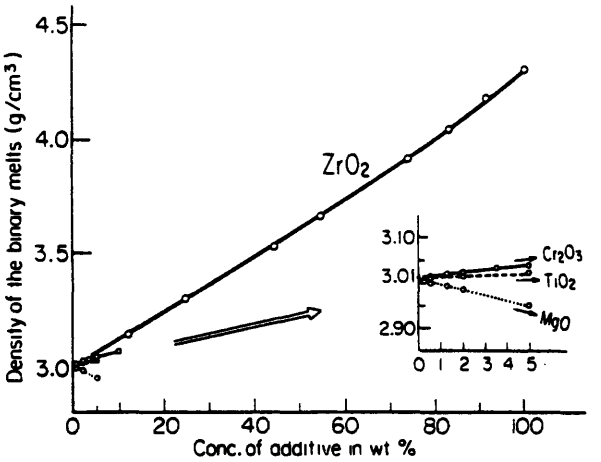

Fig. 3. Density of melts calculated with approximations detailed in Section II.

Table II. Composition, Liquid Density, and Liquid Temperature of Binary Mixtures

Composition of binary mixture (wt% additive)	Calculated liquid density (g/cm³)	Estimated melt temperature (°C)
	Al_2O_3-Cr_2O_3	
0.50	2.888	2075
1.25	2.893	2080
2.00	2.898	2082
3.50	2.908	2087
5.00	2.918	2090
10.00	2.953	2100
	Al_2O_3-TiO_2	
0.50	2.887	2075
2.00	2.894	2070
5.00	2.908	2050
	Al_2O_3-MgO	
0.25	2.880	2065
0.50	2.880	2050
1.25	2.865	2015
2.00	2.867	1965
5.00	2.843	2010
	Al_2O_3-ZrO_2	
11.84	3.027	2067
25.00	3.193	2010
44.62	3.455	1935
54.72	3.597	1990
73.82	3.883	2145
82.66	4.025	2305
91.58	4.167	2480
100.00	4.310	2740

V. Discussion

The results demonstrate the superior precision of this technique for analyzing pendant drops. The extremes between γ/ρ values for five independent measurements were typically 1% when determined by comparing contours. This reproducibility is comparable to the incremental differences between the calculated contours used to analyze the experimental contours. In contrast, γ/ρ values we determined using conventional methods of analyzing pendant drops from measured r_e and r_s values varied as much as ±10%. As can be seen from Table III, our precision is better than reported by others using a variety of surface tension measurement techniques.

The potential accuracy provided by this technique exceeds

**Lot No. AF-314475, Northeast Cryogenics, Waltham, MA.
††Grade 6 Helium, Lot No. N-347874, Airco Industrial Gases, Murray Hill, NJ.

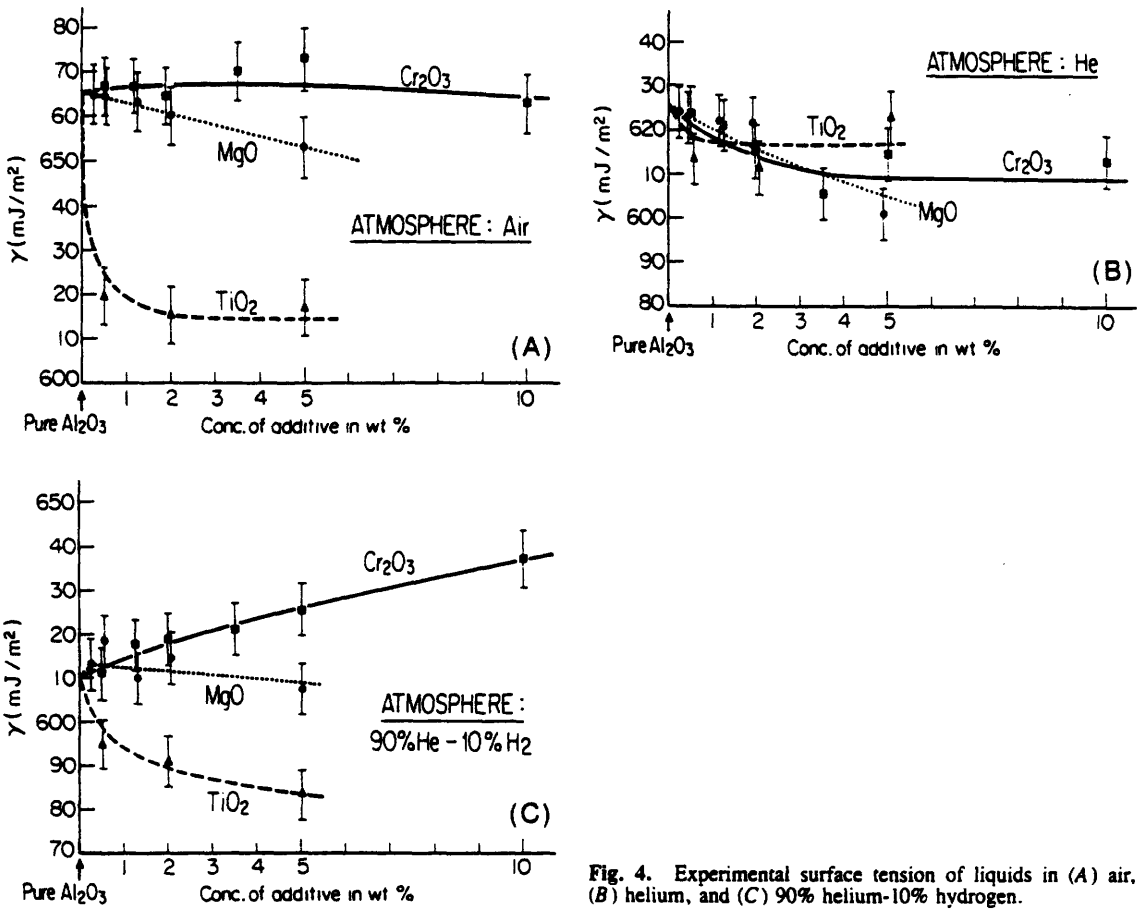

Fig. 4. Experimental surface tension of liquids in (*A*) air, (*B*) helium, and (*C*) 90% helium-10% hydrogen.

present knowledge of the melt densities. Because they have not generally been characterized experimentally, we calculated them using the stated assumptions. It is evident that the γ accuracy is limited by the ρ accuracy at this time. We would speculate that our absolute γ errors are in the range of 2 to 3% (13 to 20 mJ/m^2). The difference between our measured value for the surface tension of Al_2O_3 in He and that cited in Ref. 5 (570 mJ/m^2) exceeds the combined estimates of both errors. This difference may reflect systematic differences between the pendant-drop and bubble pressure measurement techniques.

In general, surface energies increased with increasing available oxygen. For pure Al_2O_3, γ was 665, 625, and 610 mJ/m^2 for air, He, and He-H_2 atmospheres, respectively.

The effect on surface energies of additions up to $\approx$10 wt% was generally either a small monotonic increase or decrease. TiO_2, the exception, caused a rapid decrease in γ for levels $\leq$0.5 wt% followed by essentially constant γ values for higher concentrations. Samples for each atmosphere and dopant group were characterized by electron microprobe; surface and bulk compositions exhibited no evidence of segregation.

The γ results have been treated with the Gibbs adsorption isotherm analysis to give the surface excesses of solute in the binary solutions, Γ_s (mol/cm^2); Γ_s is defined[29] by

$$d\gamma = -RT\Gamma_s d(\ln a_s) \tag{6}$$

where a_s is the activity of the solute. The Γ_s values shown in Table IV were calculated with the approximation that a_s is equal to the molar fraction of the solute. Γ_s values are positive and negative and they are at least 100 times smaller than values corresponding to a monolayer of pure solute (nominally 2×10^{-9} mol/cm^2), indicating that none of the solutes exhibits a strong surface activity in liquid alumina.

For an air atmosphere, additives generally caused the γ values to increase or decrease in the same direction that they cause the liquidus temperatures to change. For small concentrations, Cr_2O_3 is the only additive that raises the melting point and it is the only additive that raises the γ value. The minimum γ value for the system Al_2O_3-ZrO_2 corresponds to the eutectic composition, approximately 42 wt% ZrO_2. For ZrO_2 contents $\geq$70 wt%, γ decreases with increasing ZrO_2, violating this generality. This departure may result from a thermal reduction of the high ZrO_2 content melts as evidenced by the darkening of the quenched pendant drops, following the trend of reduced γ's with reduced oxygen partial pressures. Alternatively, the calculated liquid densities may not be valid over this extreme range.

The effects of specific additives on γ's in He and He-H_2 atmospheres are more complex; their magnitudes do not follow trends expected on the basis of available oxygen. No data was found for the effect of oxygen partial pressure on melting points, so this correlation could not be examined. It is apparent that γ's for these systems are sensitive to atmosphere and composition even though the causes are not understood.

VI. Summary and Conclusions

An improved technique for analyzing the surface energies of liquids in a pendant-drop configuration has been developed. The procedure, based on comparing observed and calculated contours, is particularly applicable to melts that cannot be extended to high length to diameter ratios and to high temperature melts for which precise dimensional characterization is difficult. The results demonstrated the technique with several alumina-containing melts. The precision of the γ/ρ measurements appears to be approximately 1%. The accuracy of the γ values is limited by the lack of measured ρ values.

Both composition and atmosphere have significant effects on γ values. In an air atmosphere, the effect of additives on γ's parallels their effect on melting points. In He and He-H_2 atmospheres the effects are more complex. None of the solutes exhibited a strong surface activity when analyzed in terms of Gibbs surface excesses.

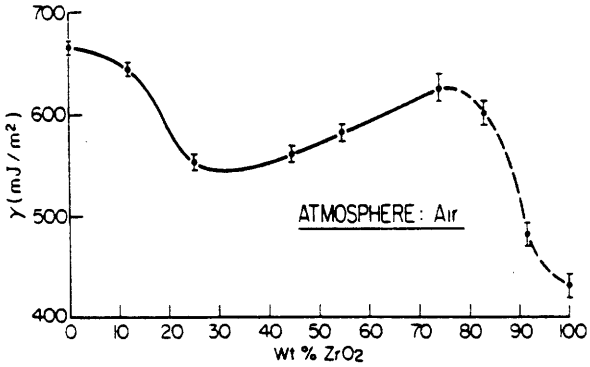

Fig. 5. Experimental surface tension of Al_2O_3-ZrO_2 liquids in air.

Acknowledgments: The specialized laser-heated crystal growth equipment was provided by NSF Contract No. 791687–DMR. Anne H. Foster, Boston, MA, and the Materials Processing Center, MIT. David Lum, Douglas Chin, and Paul McGrath assisted in sample preparation and computational work; Professor R. A. Brown provided important background information and insights. All contributions are gratefully acknowledged.

References

[1]E. T. Turkdogan, Physico-Chemical Properties of Molten Slags and Glasses. The Metals Society, London, August 1983.

[2]M. Humenik and W. D. Kingery, "Metal-Ceramic Interactions: Surface Tension and Wettability of Metal-Ceramic Systems," *J. Am. Ceram. Soc.*, **37** [1] 18–23 (1954).

[3]W. D. Kingery, "Surface Tension of Some Liquid Oxides and Their Temperature Coefficients," *J. Am. Ceram. Soc.*, **42** [1] 6–8 (1959).

[4](*a*)V. P. Elyutin, E. F. Grifts, and B. S. Mitin, "Wetting of Refractory Metals by Oxide Melts," *Izv. Akad. Nauk. SSSR, Neorg. Mater.*, **10**, 5 (1974); *Inorg. Mater. (Engl. Transl.)*, **10**, 723–25 (1974).

(*b*)V. P. Elyutin, E. F. Grifts, and B. S. Mitin, "Wetting of Refractory Metals by Al_2O_3-MgO Melts," ibid., **10**, 1796–97 (1974).

[5]Yu. S. Anisimov, E. F. Grifts, and B. S. Mitin, "Surface Tension and Density of Melts of the Systems Al_2O_3-SiO_2 and Al_2O_3-Cr_2O_3," *Izv. Akad. Nauk. SSSR, Neorg. Mater.*, **13**, 1444–46 (1977); *Inorg. Mater. (Engl. Transl.)*, **13**, 1168–70 (1977).

[6]T. Young, "An Essay on the Cohesion of Fluids," *Proc. R. Soc. London*, **1**, 171 (1804); *Philos. Trans. R. Soc. London*, 61 (1805).

[7]P. S. Laplace, Mecanique Celeste, Suppl., Livre X. Paris, 1805.

[8]F. Bashforth and J. C. Adams, An Attempt to Test the Theories of Capillary Action by Comparing the Theoretical and Measured Forms of Drops of Fluids. Cambridge University Press, London, 1883.

[9]S. Sugden, "The Determination of Surface Tension from the Rise in Capillary Tube," *J. Chem. Soc.*, 1483 (1921).

[10]N. K. Adam, The Physics and Chemistry of Surfaces, 3rd ed.; p. 365. Oxford University Press, 1941.

[11]J. M. Andreas, E. A. Hauser, and W. B. Tucker, "Boundary Tension by Pendant Drops," *J. Phys. Chem.*, **42**, 1001 (1938).

[12]S. Fordham, "On the Calculation of Surface Tension from Measurements of Pendant Drops," *Proc. R. Soc. London, Ser. A*, **A194**, 1 (1948).

[13]A. W. Adamson, Physical Chemistry of Surfaces, 2nd ed.; p. 14. Wiley, New York, 1967.

[14]C. E. Stauffer, "The Measurement of Surface Tension by the Pendant Drop Technique," *J. Phys. Chem.*, **69**, 1933 (1965).

[15]C. Huh and R. L. Reed, "A Method for Estimating Interfacial Tensions and Contact Angles from Sessile and Pendant Drop Shapes," *J. Colloid Interface Sci.*, **91** [2] 472 (1983).

[16]J. S. Haggerty and W. P. Menashi, Production of Oxide Fibers by a Floating Zone Fiber Drawing Technique, NASA CR-72811, ADL 71997, 1971.

[17]J. F. Padday, "The Measurement of Surface Tension"; pp. 110–12 in Surface and Colloid Science, Vol. 1. Edited by E. Matijevic. Wiley Interscience, New York, 1969.

[18]J. F. Padday, "The Profile of Axially Symmetric Menisci," *Philos. Trans. R. Soc. London, Ser. A*, **A269**, 265 (1971).

[19]J. F. Padday and A. Pitt, "Axisymmetric Meniscus Profiles," *J. Colloid Interface Sci.*, **38** [2] 1972.

[20]A. D. Kirshenbaum and J. A. Cahill, "The Density of Liquid Aluminum Oxide," *J. Inorg. Nucl. Chem.*, **14** [3–4] 283–87 (1960).

[21]B. S. Mitin and Yu. A. Nagibin, "Density of Molten Aluminum Oxide," *Russ. J. Phys. Chem. (Engl. Transl.)*, **44** [5] 741–42 (1970).

[22]N. Bloembergen, "Fundamental of Laser-Solid Interactions"; pp. 1–8 in Laser-Solid Interactions and Laser Processing. Materials Research Society, 1978.

[23]M. Lax, "Temperature Rise Induced by a Laser Beam," *J. Appl. Phys.*, **48**, 3919 (1977); *Appl. Phys. Lett.*, **33**, 786 (1978).

Table III. Cited Surface Tension Values for Liquid Alumina

Surface tension (mJ/m^2)	Atmosphere	Method used	Ref.
665 ± 15	Air	Pendant drop (ρ = 3.01)	Present work
625 ± 14	He		
610 ± 13	He + 10% H_2		
700		Theoretical value based on electrostatic forces between ions in coordinated or nearly ordered melt	26
577 ± 80	Vacuum	Drop weight (ρ = 2.5)	24
586 ± 81	Vacuum	Drop weight (ρ = 3.2)	
690 ± 48	He	Pendant drop (ρ = 2.97)	3
551	Not specified	Sessile drop, from contact angle value	25
574 ± 68	Vacuum	Pendant drop (ρ = 3.01)	27
570	He	Maximum bubble pressure (ρ = 3.03)	5

Table IV. Gibbs Surface Excesses of Solute in Binary Mixtures

Atmosphere	Surface excess (10^{-11} mol/cm²)	Coefficient of correlation ($-1 \leq R \leq 1$)
	Al_2O_3-TiO_2	
Air	0.69	0.6617
He	−1.91	−0.7128
He + 10% H_2	2.36	0.9638
	Al_2O_3-Cr_2O_3	
Air	−0.08	−0.0469
He	1.77	0.6920
He + 10% H_2	−3.96	−0.9338
	Al_2O_3-MgO	
Air	7.88	0.9170
He	2.98	0.7183
He + 10% H_2	0.94	0.5124

[24](*a*) H. von Wartenberg, E. Wehner, and E. Saran, "die Oberflächenspannung von geschmolzener Al_2O_3 und La_2O_3," *Nachr. Ges. Wiss. Gottingen, Math.-Phys. Kl., Fachgruppe* 2, 65–71 (1936–37).

(*b*)H. von Wartenberg, E. Wehner, and E. Saran, "Die Dichte geschmolzener Tonerde," ibid., 73–75 (1936–37).

[25]R. W. Bartlett and J. K. Hall, "Wetting of Several Solids by Al_2O_3 and BeO Liquids," *Am. Ceram. Soc. Bull.*, **44** [5] 444–48 (1965).

[26]O. K. Sokolov, "On the Surface Tension of Molten Salts and Oxides," *Izv. Akad. Nauk. SSSR, Metall. Gorn. Delo*, **4**, 59–64 (1963); *Russ. Metall. Min. (Engl. Transl.)*, **4**, 37–44 (1963).

[27]J. J. Rasmussen and R. P. Nelson, "Surface Tension and Density of Molten Al_2O_3," *J. Am. Ceram. Soc.*, **54** [8] 398–401 (1971).

[28]E. M. Levin, C. R. Robbins, and H. F. McMurdie, Phase Diagrams for Ceramists. Edited by M. K. Reser. The American Ceramic Society, Inc., Columbus, OH. Figs. 260, 309, and 316 (1964 Suppl.) and Fig. 4378 (1969 Suppl.).

[29]W. J. Moore, Physical Chemistry, 2nd ed.; p. 508. Prentice-Hall Chemical Series, Englewood Cliffs, NJ, 1960.

VII. Appendix 1: Listing of Publications and Theses Resulting from Research Sponsored by this Program

I. PUBLICATIONS

- **PAPERS IN REFEREED JOURNALS**

1. Mizuta, S., W.R. Cannon, A. Bleier, and J.S. Haggerty, *Wetting and Dispersion of Silicon Powder Without Deflocculants,* AM. CER. SOC. BULL. 61 [8], 872-875 (1982). [J82-05]

2. Sawhill, H.T. and J.S. Haggerty, *Crystallization of Ultrafine Amorphous Si_3N_4 During Sintering,* J. AM. CER. SOC. 65 [8], C131-132 (1982). [J82-06]

3. Danforth, S.C. and J.S. Haggerty, *Mechanical Properties of Sintered and Nitrided Laser-Synthesized Silicon Powder,* J. AM. CER. SOC. 66 [4], C58-59 (1983). [J83-02]

4. Suyama, Y., J.S. Haggerty and H.K. Bowen, *Synthesis of Ultra-fine SiC Powders by Laser Driven Gas Phase Reactions,* J. THE CHEMICAL SOCIETY OF JAPAN, CHEM. AND INDUSTRIAL CHEM., No. 10, 1539 (1984). [J84-03]

5. Lihrmann, J-M. and J.S. Haggerty, *Surface Tensions of Alumina-Containing Liquids,* J. AM. CER. SOC. 68 [2], 81-85 (1985). [J85-01]

6. Suyama, Y., R.A. Marra, J.S. Haggerty, and H.K. Bowen, *Synthesis of Ultrafine SiC Powders by Laser Driven Gas Phase Reactions,* AM. CER. SOC. BULL. 64 [10], 1356-59 (1985). [J85-02]

7. Flint, J.H., R.A. Marra, and J.S. Haggerty, *Powder Temperature, Size, and Number Density in Laser-Driven Reactions,* AEROSOL SCI. AND TECH. 5, 249-260 (1986). [J86-03]

8. Marra, R.A., J.H. Flint, and J.S. Haggerty, *Homogeneous Nucleation and Growth of Silicon Powder from Laser Heated SiH_4,* submitted for publication to the J. AM. CER. SOC. [J87-01]

9. Marra, R.A., and J.S. Haggerty, *Crystal Structure of Silicon Powders Produced from Laser-Heated Silane,* J. AM. CER. SOC. 70 [1], C15-17 (1987). [J87-02]

10. Sawano, K., J.S. Haggerty and H.K. Bowen, *Formation of SiC Powder from Laser Heated Vapor Phase Reactions,* Yogyo-Kyokai-Shi (J. CERAMIC SOC. OF JAPAN) 95 [1], 64-69 (1987). [J87-10]

11. Castro, D., T.A. Ring, and J.S. Haggerty, *Drying of Silicon Powder Compacts,* accepted for publication in J. AM. CER. SOC. [J87-13]

12. Okuyama, M., G. Garvey, T.A. Ring and J.S. Haggerty, *Dispersion of SiC Powders in Non-aqueous Solvents,* submitted for publication to J. AM. CER. SOC. [J87-15]

13. Flint J.H. and J.S. Haggerty, *Processing and Properties of Reaction Bonded Silicon Nitride and Silicon Carbide Made From Laser Synthesized Powders,* submitted for publication to J. AM. CER. SOC. [J88-01]

14. Flint, J.H. and J.S. Haggerty, *A Model for the Growth of Silicon Particles from Laser Heated Gases*, submitted for publication to AEROSOL SCI. AND TECH. [J88-02]

15. Ritter, J.E., S.V. Nair, P. Gennari, W.A. Dunlay, J.S. Haggerty and G.J. Garvey, *High Strength Reaction Bonded Silicon Nitride*, accepted for publication in J. AM. CER. SOC. [J88-03]

- **PROCEEDINGS OF CONFERENCES**

1. Marra, R.A. and J.S. Haggerty, *Synthesis and Characteristics of Ceramic Powders made from Laser-Heated Gases,* CERAMIC ENG. AND SCIENCE PROCEEDINGS, Vol. 3, [1-2], 3-19 (1982). [P82-01]

2. Haggerty, J.S., *Growth of Precisely Controlled Powders from Laser Heated Gases,* ULTRASTRUCTURE PROCESSING OF CERAMICS, GLASSES, AND COMPOSITES, 353-66, Eds. L. L. Hench and D. R. Ulrich, J. Wiley & Sons, 1983. [P83-02]

3. Haggerty, J.S., *Synthesis of Powders and Thin Films by Laser Induced Gas Phase Reactions,* EMERGENT PROCESS METHODS FOR HIGH-TECHNOLOGY CERAMICS, Mat. Sci. Res., Vol. 17, 137-54, Plenum Press, 1984. [P84-01]

4. Flint, J.H. and J.S. Haggerty, *Ceramic Powders from Laser Driven Reactions,* APPLICATIONS OF LASERS TO INDUSTRIAL CHEM., SPIE, Vol. 458, 1984. [P84-02]

5. Haggerty, J.S., *Synthesis of Ceramic Powders and Surface Films from Laser Heated Gases,* INNOVATIONS IN MAT. PROCESSING, Vol. 30, Sagamore Army Mat. Res. Conference Processings, Eds. V. Weiss and G. Bruggeman, p. 355-79, 1985. [P85-01]

6. Haggerty, J.S. and J.H. Flint, *Ceramic Powders from Laser Heated Reactant Gases,* ADVANCES IN CERAMICS, S. Somiya (ed.), Tokyo, Terra Scientific Publishing Company, 1986. [P85-03]

7. Haggerty, J.S., G. Garvey, J-M. Lihrmann and J.E. Ritter, *Processing and Properties of Reaction Bonded Silicon Nitride made from Laser Synthesized Silicon Powders* in DEFECT PROPERTIES AND PROCESSING OF HIGH-TECHNOLOGY MAT., Y. Chen, W.D. Kingery and R.J. Stokes (eds.), Proceedings of the Mat. Res. Society, 1986. [P85-05]

8. Haggerty, J.S., J. Flint, G. Garvey, J-M. Lihrmann and J.E. Ritter, *High Strength, Oxidation Resistant Reaction Bonded Silicon Nitride from Laser-Synthesized Silicon Powder,* in CERAMIC MAT. AND COMPONENTS FOR ENGINES, W. Bunk, H. Hauser (eds.), Verlag Deutsche Keramische Gesellschaft, pp. 147-54, Apr 1986. [P86-01]

9. Lihrmann, J-M., M. Luce, O. Croix, M. Cauchetier and J.S. Haggerty, *Potentiel des Ceramiques Thermo-Mechaniques Elaborees a Partir de Poudres Laser,* to be published in PRESENT AND FUTURE OF CERAMICS IN THE MECHANICAL INDUSTRIES, June 1987. [P87-02]

10. Flint, J.H. and J.S. Haggerty, *Laser Synthesized Ceramic Powders: Synthesis, Characteristics, Fabrication, and Part Properties*, to be published in the Proceedings of the 172nd Meeting of the Electrochemical Society, Session IV, High Temperature Synthesis, Honolulu, Hawaii, October 1987. [P87-05]

11. Flint, J.H. and J.S. Haggerty, *Models for Synthesis of Ceramic Powders by Vapor Phase Reactions*, to be published in the Proceedings of the First International Conference on Ceramic Powder Processing Science, American Ceramic Society, Orlando, Florida, November 1987. [P87-08]

12. Haggerty, J.S., G.J. Garvey, J.H. Flint, B.W. Sheldon, M. Aoki, M. Okuyama, J.E. Ritter and S.V. Nair, *Processing and Properties of Reaction Bonded Silicon Nitride and Sintered Silicon Carbode Made From Laser Synthesized Powders*, to be published in the Proceedings of the First International Conference on Ceramic Powder Processing Science, American Ceramic Society, Orlando, Florida, November 1987. [P87-09]

13. Haggerty, J.S., A. Lightfoot, J.E. Ritter, S.V. Nair and P. Gennari, *Properties of Reaction Bonded Silicon Nitride made from High Purity Silicon Powder*, to be published in the Proceedings of the 12th Annual Conference on Composites and Advanced Ceramics, American Ceramic Society, Cocoa Beach, Florida, January 1988. [P88-03]

- **BOOK CHAPTERS**

1. Haggerty, J.S., *Synthesis of Ceramic Powders and Thin Films from Laser Heated Gases*, Chapter in DESIGN OF NEW MATERIALS, A. Clearfield, and D.L. Cocke (eds.), Plenum Pub. Co., New York, NY, 1987. [M87-01]

II. THESES

• S.B. Theses

1. Lum, David, *The Effects of Machining Induced Defects on the Mechanical Strength of High Purity RBSN*, June 1986 (Mechanical Eng., MIT).

• S.M. Theses

1. Batakis, Anthony, *A Study of the Biaxial Strength Testing of Brittle Material*, May, 1980, (University of Massachusetts).

2. Sawhill, Howard T., *Crystallization of Ultra-fine Amorphous SiN During Sintering*, Sept 1981 (Materials Science and Engineering, MIT).

3. Flint, John H., *Powder Temperatures in Laser Driven Reactions*, Feb 1982 (Materials Science and Engineering, MIT).

4. Dunlay, William A., *Mechanical Properties of Laser Synthesized Reaction Bonded Silicon Nitride*, Sept 1987, (University of Massachusetts).

- **Doctoral Theses**

1. Marra, Robert A., *Homogeneous Nucleation and Growth of Silicon Powder from Laser Heated Gas Phase Reactions*, Feb 1983 (Materials Science and Engineering, MIT).

2. Akmandor, Ibrahim Sinan, *Theoretical and Computational Model of Reacting Silane Gas Flows: Laser Driven Pyrolysis of Subsonic and Supersonic Jets*, June 1985, (Aeronautics and Astronautics, MIT).

3. Sawano, Kiyoshi, *Formation of Silicon Carbide Powder from Laser Induced Vapor Phase Reactions*, June 1985 (Materials Science and Engineering, MIT).

4. Sheldon, Brian, *The Determination and Analysis of Rate Controlling Mechanisms that Affect the Nitriding of Silicon Powder Compacts*, expected Jan 1988 (Materials Science and Engineering, MIT).